DISSERTATION

ANALYSIS OF IMPACT OF NON-UNIFORMITIES ON THIN-FILM SOLAR CELLS AND MODULES WITH 2-D SIMULATIONS

Submitted by

Galymzhan T. Koishiyev

Department of Physics

In partial fulfillment of the requirements

For the Degree of Doctor of Philosophy

Colorado State University

Fort Collins, Colorado

Spring 2010

COLORADO STATE UNIVERSITY

March 22, 2010

WE HEREBY RECOMMEND THAT THE DISSERTATION PREPARED UNDER OUR SUPERVISION BY GALYMZHAN T. KOISHIYEV ENTITLED ANALYSIS OF IMPACT OF NON-UNIFORMITIES ON THIN-FILM SOLAR CELLS AND MODULES WITH 2-D SIMULATIONS BE ACCEPTED AS FULFILLING IN PART REQUIREMENTS FOR THE DEGREE OF DOCTOR OF PHILOSOPHY.

Committee on Graduate work

_____
John L. Harton

_____
Kevin L. Lear

_____
Robert G. Leisure

_____
Advisor: James R. Sites

_____
Department Head: Dieter H. Hochheimer

ABSTRACT OF DISSERTATION

ANALYSIS OF IMPACT OF NON-UNIFORMITIES ON THIN-FILM SOLAR CELLS AND MODULES WITH 2-D SIMULATIONS

Clean and environmentally friendly photovoltaic (PV) technologies are now generally recognized as an alternative solution to many global-scale problems such as energy demand, pollution, and environment safety. The cost ($/kWh) is the primary challenge for all PV technologies. In that respect, thin-film polycrystalline PV technology (CdTe, Cu(In,Ga)Se_2, etc), due to its fast production line, large area panels and low material usage, is one of the most promising low-cost technologies.

Due to their granular structure, thin-film solar cells are inherently non-uniform. Also, inevitable fluctuations during the multistep deposition process of large area thin-film solar panels and specific manufacturing procedures such as scribing result in non-uniformities. Furthermore, non-uniformities can occur, become more severe, or increase in size during the solar-panel's life cycle due to various environmental conditions (i.e. temperature variation, shading, hail impact, etc). Non-uniformities generally reduce the overall efficiency of solar cells and modules, and their effects therefore need to be well understood.

This thesis focuses on the analysis of the effect of non-uniformities on small size solar cells and modules with the help of numerical simulations. Even though the 2-D

model developed here can analyze the effect of non-uniformities of any nature, only two specific types of microscopic non-uniformities were addressed here: shunts and weak-diodes. One type of macroscopic non-uniformity, partial shading, was also addressed.

The circuit model developed here is a network of diodes, current-sources, and transparent-conductive-oxide (TCO) resistors. An analytic relation between the TCO-resistor, which is the primary model parameter, and TCO sheet resistance ρ_S, which is the corresponding physical parameter, was derived. Based on the model several useful general results regarding a uniform cell were deduced. In particular, a global parameter δ, which determines the performance of a uniform solar cell depending on sheet resistance ρ_S, cell length L, and other basic parameters, was found. The expression for the lumped series resistance in terms of physical parameters was also derived. Primary power loss mechanisms in the uniform case and their dependence on ρ_S, L, and light generated current J_L were determined.

Similarly, power losses in a small-area solar cell with either a shunt or a weak-microdiode were identified and their dependence on ρ_S, J_L, and location of the non-uniformity with respect to the current collecting contact was studied. The impact of multiple identical non-uniformities (shunts or weak-diodes) on the performance of a module was analyzed and estimates of efficiency loss were presented. It was found that the efficiency of the module strongly depends not only on the severity and fractional area of non-uniformities but also on their distribution pattern. A numerical parameter characterizing distribution pattern of non-uniformities was introduced. The most and least favorable distribution patterns of shunts and weak-diodes over the module area were determined.

Experimentally, non-uniformities may be detected with the help of spatially resolved measurements such as electroluminescence (EL). The 2-D circuit model was also used to develop the general framework to extract useful information from experimental EL data. In particular, a protocol that can help distinguish a shunt from a weak-diode and estimate the severity of the non-uniformity based on the EL data was developed. Parts of these simulation results were verified with experimental EL data obtained by other authors.

The thesis also discusses the effect of partial shading (a macroscopic non-uniformity) on the operation and safety of thin-film solar panels. A detailed analysis of the current-voltage characteristics of partially shaded module was performed. Conditions that result in a shaded cell experiencing high reverse voltage were shown. A mathematical formalism was developed to distinguish two extremes: when reverse-bias shunting or breakdown dominates. It was shown that in the shunt-dominated case in extreme situations the voltage across the shaded cell can be quite large (~ 20V). High voltage across the shaded cell results in both high power dissipation and elevated temperature. Depending on the light generated current, the temperature above ambient of the shaded cell can be as high as ~100-300ºC, implying potential safety issues. The analysis covered all basic rectangular shade configurations.

Galymzhan T. Koishiyev
Physics Department
Colorado State University
Fort Collins, CO, 80523
Spring 2010

Acknowledgments

I owe my deepest gratitude to my advisor Jim Sites. He has made his support available in a number of ways. His encouragement and guidance from the initial to the final level enabled me to develop the skills, acquire the knowledge and do the research I needed to write this dissertation and achieve my goal. Jim would always be there to help me out in times of frustration and discouragement. There is a saying: “I’ve learned that people will forget what you said, people will forget what you did, but people will never forget how you made them feel”. I will never forget how welcome and comfortable Jim made me feel over these years.

I am indebted to my many colleagues: Ana Kanevce, Alan Davies, Jun Pan, Tim Nagle, Ray Hsiao, Katherine Zaunbrecher, John Raguse, and Russell Geisthardt. I would like to thank all of them for their support.

This dissertation would not have been possible without the moral support from my family: my mom and dad, Kuralay, Dinara, Abu-Raikhan and all my relatives back home. I am grateful to my family for cheering me up and believing in me. I would also like to show my gratitude to all my friends I met here in Colorado for all the good time we spent together.

Lastly, I offer my regards and blessings to all of those who supported me in any respect during the completion of my Ph.D. degree.

Contents

List of figures

Ch. 1

Ch. 2

Ch. 3

Ch. 4

Ch. 5

Ch. 6

List of tables

Ch. 1

Ch. 2

Ch. 3

Chapter 1
Introduction

1.1. The big picture

The industrial revolution that spread over the world by the end of nineteenth century marked a new era in the history of humankind. During that period the world made a transition from manual labor and draft-animal–based economy towards machine-based manufacturing. Since the revolution, consumption of fossil fuels to drive the economy has been growing exponentially, causing three primary global problems: depletion of fossil fuels, pollution, and climate change.

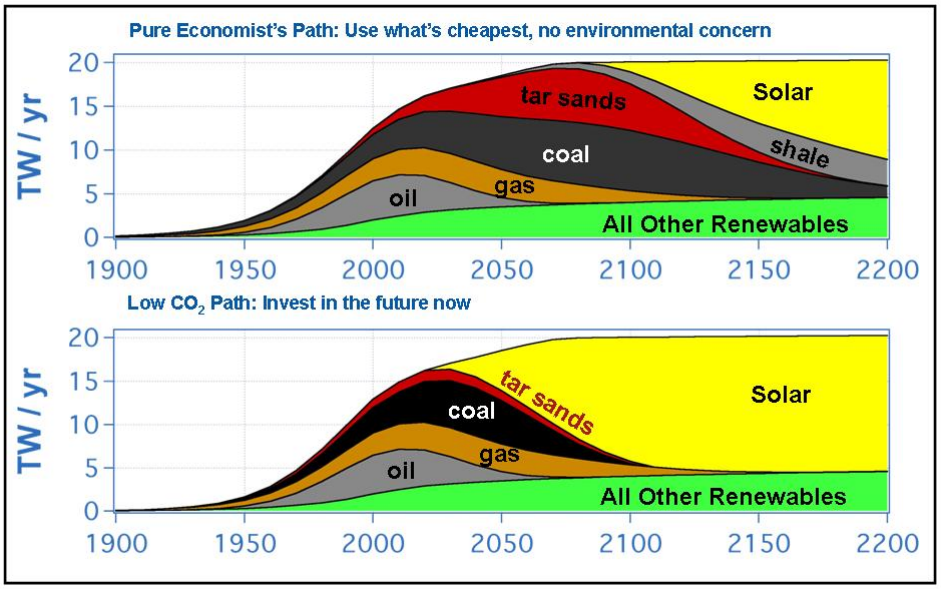

Fig.1.1. World power consumption. (From AVS Short Course - 2009, NREL[1])

In 2008 total worldwide power consumption was 15 TW and 80-90% of that came from burning fossil fuels. **Figure 1.1** shows world power consumption in the past, its current status and two future forecasts based on different approaches: 1. “use what’s cheapest, no environmental concern”, 2. “save the planet, invest in the future now”. In both future forecasts the world is forced to make another worldwide revolutionary technological transition due to depletion of resources. However, besides the inevitable depletion of accessible fossil fuels, there is a global concern that makes the second approach more appealing – the problem of increasing pollution. There is yet another worldwide problem caused by burning fossil fuels – global warming and climate change (still debatable). Due to technological lifestyles, neglectful attitudes towards the nature and a constantly increasing population, we as a species have become a force of nature that is capable of altering environment on a global scale. The issue of global warming and its impact is addressed in depth elsewhere.

Thus, there are more than enough reasons to shift from burning fossil fuels to using clean, safe and environmentally friendly technologies to produce electricity from renewable energy sources such as solar, wind, tidal waves, etc. Photovoltaic (PV) technologies, which convert solar energy directly into electricity, are very likely to play an ever increasing role in electricity production worldwide. There are several primary competing PV technologies such as crystalline and multi-crystalline (c-Si, c-GaAs), thin-

film polycrystalline (a-Si, CdTe, $Cu(In,Ga)Se_2$ (CIGS), etc), organic and multijunction concentrators.

Thin-film (TF) polycrystalline PV is a promising technology that has its advantages: low-cost, fast production line, large area panels. However, TF polycrystalline solar cells are inherently non-uniform due to their granular structure. Various non-uniformities, which occur during manufacturing process, generally reduce the overall performance of TF solar panels and their lifetime. Some of these non-uniformities can be experimentally detected with the help of different spatially resolved imaging techniques such as Light Beam Induced Current (LBIC), Electroluminescence (EL), etc.

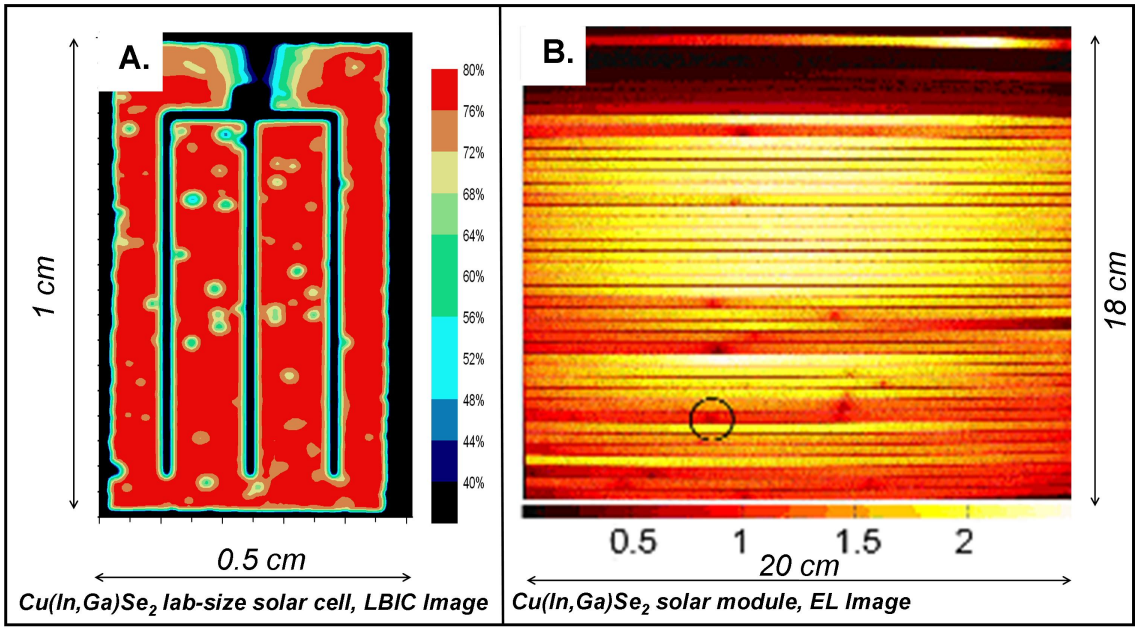

Fig.1.2. Experimental visualization of non-uniformities in A.) CIGS solar cell (measured by author) and B.) CIGS module[2].

Figure 1.2 shows an LBIC image of a lab-sized CIGS TF solar cell measured by the author and an EL image of a CIGS TF solar module from Ref. [2]. Both images reveal that there are non-uniformities of different severities.

The primary focus of the current work is to analyze and evaluate the impact of specific non-uniformities on thin-film solar cells and modules with the help of 2-D numerical simulations, show how such simulations can be coupled with experiments (EL) and provide useful information and recommendations for manufacturers.

Figure 1.3 shows primary layers of a solar cell: back-contact metal (BC), p-type layer, n-type layer, transparent-conductive-oxide (TCO), and front-contact (FC).

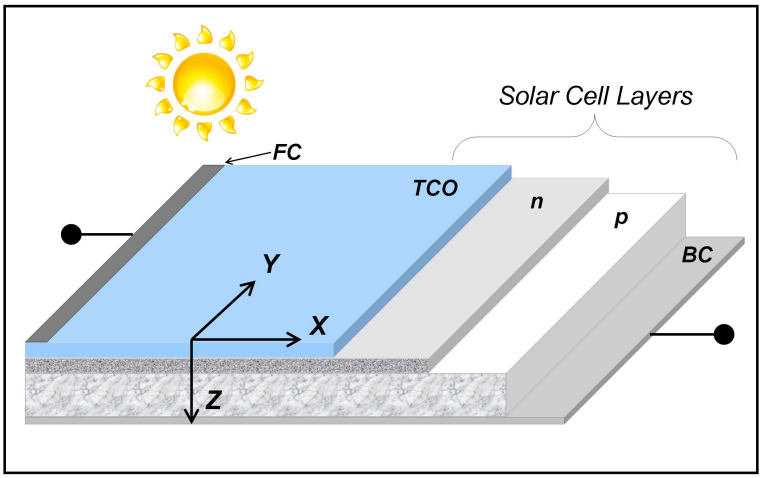

Fig.1.3. Basic solar cell layers.

Usually, simulations in the *Z*-direction that involve the definition of properties of each layer and interfaces between them are referred to as 1-D simulations. However, in the present work such simulations are referred to as *normal 1-D* simulations, because there can also be *planar 1-D* simulations in the *X*-direction that do not deal with layers. There are several normal 1-D simulation software packages (AMPS, SCAPS, etc.) specifically adapted to model properties of solar cell layers and interfaces, though the solar cell physics associated with these properties is beyond the scope of the present work. All of these programs are based on solving coupled differential equations (Poisson's equation and continuity equations for holes and electrons). The primary final product of a normal

1-D simulation is the current-voltage (*J-V*) curve (or numerical table). If some of the properties in *Z* direction are different from the rest of the overall cell area it causes a 2-D spatial non-uniformity. Analysis of the impact of such non-uniformities is beyond the scope of normal 1-D simulations.

A *J-V* curve obtained from either normal 1-D simulation, experiments on a small size solar cell, or analytic approximations serves as raw data for a planar 2-D simulation in *X* and *Y*-directions (or simply 2-D simulation). Such 2-D simulations account for voltage drop in the TCO layer of the solar cell and have the capability to analyze the effect of 2-D spatial non-uniformities. A detailed 2-D simulation framework used in the current work is discussed in the following chapter. Planar 1-D model also accounts for voltage drop in the TCO layer but is only used here to analyze uniform cells.

Since the *J-V* curve of a solar cell is in the center of the present work it is necessary to introduce its basic features and terminology.

1.2. Current-voltage curve and terminology

In the first approximation a solar cell can be modeled by a simple circuit diagram shown in **figure 1.4**.

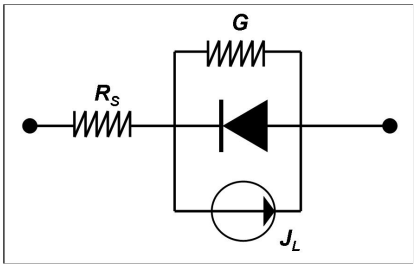

Fig.1.4. Equivalent circuit of a solar cell.

The basic circuit diagram shown in **figure 1.4** has four elements: p-n junction diode, light generated current source J_L, conductance G, and series resistance R_S. Based on this circuit model one can deduce the analytic expression for the current-voltage dependence[3]:

$$J = J_0 \exp\left[\frac{q}{AkT}(V - R_S J)\right] + G(V - R_S J) - J_L \qquad (1.1)$$

Equation (1.1) can be used to show graphically the current-voltage dependence both in the dark ($J_L = 0$) and in the light ($J_L \neq 0$).

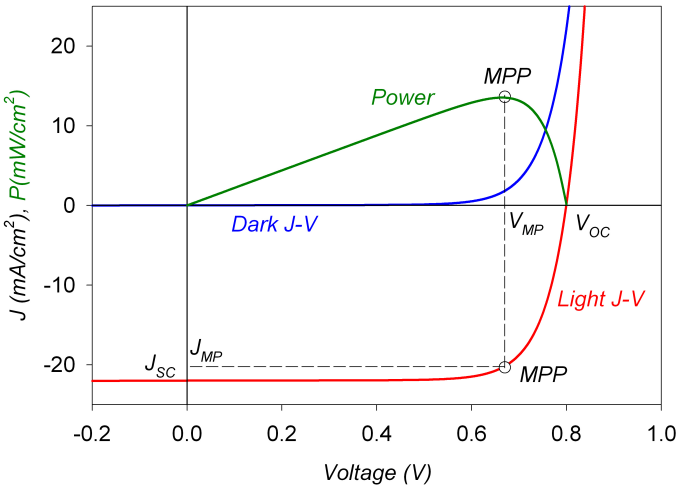

Fig.1.5. Dark and light *J-V* curves, power curve, and basic solar cell parameters.

Figure 1.5 shows *J-V* curves of a solar cell in the dark (blue solid line) and in the light (red solid line). The voltage at which the current of the light *J-V* curve is zero is called open-circuit voltage (V_{OC}) and the current at which the voltage is zero is called short-circuit current (J_{SC}). The green solid line is the generated power density graph $P(V) = J \cdot V$. The voltage at which the power has a maximum is called maximum power voltage V_{MP} and corresponding current is called maximum power current J_{MP}. The point (V_{MP},J_{MP}) on

the light *J-V* curve is called maximum power point, or MPP. Two primary parameters of a solar cell are efficiency (η) and fill-factor (*FF*). Fill factor is defined as the ratio of areas of two rectangles:

$$FF(\%) = \frac{V_{MP} \cdot J_{MP}}{V_{OC} \cdot J_{SC}} \times 100\%. \tag{1.2}$$

Efficiency η is defined as follows:

$$\eta(\%) = \frac{V_{MP} J_{MP}}{P_{in}} \times 100\% = \frac{FF \cdot V_{OC} \cdot J_{SC}}{P_{in}} \times 100\%, \tag{1.3}$$

where P_{in} is the standard normally-incident solar power density, 100 mW/cm^2. **Table 1.1** shows basic solar cell parameters of the light *J-V* curve shown in **figure 1.5.**

Table 1.1.
Basic solar cell parameters.

	η	*FF*	V_{OC}	J_{SC}	V_{MP}	J_{MP}	*G*	R_S	*A*
Units	(%)	(%)	(V)	(mA/cm^2)	(V)	(mA/cm^2)	(mS/cm^2)	(Ω·cm^2)	-
	13.5	76.9	0.8	22.0	0.67	20.3	0	0	2

In the example given above both parasitic resistances are zeros. However, this is usually not true. **Figure 1.6** shows the effect of parasitic resistances on the light *J-V* curve. The red solid line is the light *J-V* curve shown for reference with R_S = 0 Ω·cm^2 and G = 0 mS/cm^2. Dark and purple solid lines are light *J-V* curves with one of the parasitic resistances non-zero. In both cases efficiency is reduced by ~15% due to these resistances. Open circles are maximum power points.

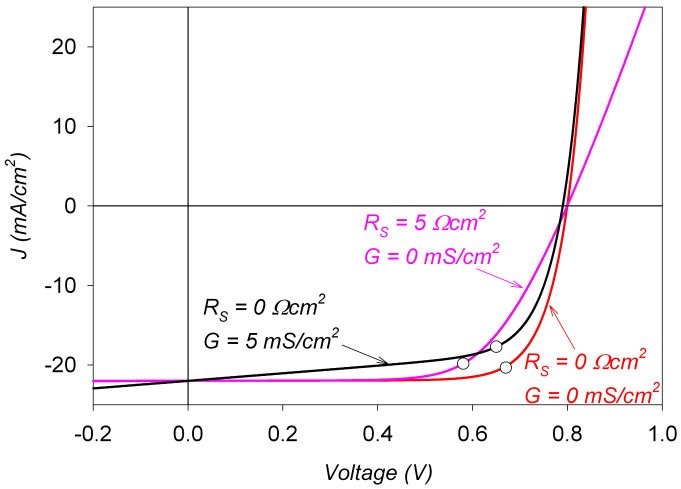

Fig.1.6. Effect of parasitic resistances on light *J*-*V* curve.

Parasitic resistances and diode quality factor *A* can be calculated from the light *J*-*V* curve with the help of equation (1.1) and simple mathematical manipulations. An example of such a comprehensive analysis is given in Ref. [3].

Thus, the general problem and the approach are outlined. Basic concepts and terminology given in this chapter are enough to understand the main body of the thesis.

Chapter 2
The 2-D model

A full treatment of the voltage drop across a transparent-conductive-oxide (TCO) contact layer is necessary both for calculating accurate *J-V* curves and as the first step in the study of spatial non-uniformities with numerical simulations. This chapter gives a detailed description of the 2-D circuit model, which in the chapters to follow is used to analyze the effect of non-uniformities. Also in the current chapter some useful general results are obtained from the analysis of the model in the uniform case. However, in the uniform case analysis only the primary *X* direction of the 2-D circuit model is considered, this is basically planar 1-D model.

2.1. The general simulation setup

2.1.1. The module baseline

The general design and geometry of most thin-film modules is essentially the same. A typical thin-film module consists of a number of elongated cells connected in series and separated from each other by scribe lines.

As a baseline, a CdTe thin-film module, which assumes a typical rectangular geometry and a distributed TCO sheet resistance ρ_S (Ω/sqr*)* is used. **Figure 2.1** shows the general simulation schematic.

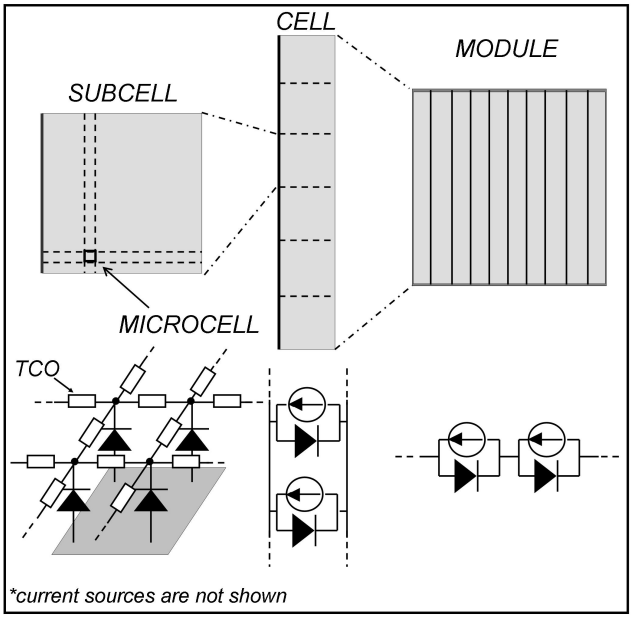

Fig.2.1. The general simulation schematic.

A complete simulation based on the **figure 2.1** implies three steps: subcell, cell and module with corresponding circuit diagrams. A subcell is a network of microcell-diodes, current sources, and TCO resistors. A more detailed description of the subcell is given in the following section. The *microcell* and *subcell* terminology has been adopted by photovoltaic groups at *Colorado State University* and colleagues at the *University of Ljubljana, Slovenia*. The baseline adopted here for a thin-film module has 40 cells, each 1-by-40 cm in size; each cell is modeled by 40 subcells (1 by 1 cm); each subcell is modeled by 21 by 21 microcells (0.05 by 0.05 cm). Current-voltage (*J*-*V*) curves of subcells are used to calculate the cell's *J*-*V* curve, and the *J*-*V* curves of cells are used to

simulate the *J-V* curve of the module. Clearly the dimensions and numbers of units can be changed to match specific situations.

2.1.2. The subcell baseline

Figure 2.2 shows a cross-sectional perspective view of a subcell, where the continuous TCO sheet resistance ρ_S (Ω/sqr) and the bulk semiconductor resistivity ρ (Ω·cm) are physical parameters, whereas the discrete TCO resistances R (Ω) and the discrete semiconductor resistances r (Ω) are corresponding model parameters. For simplicity, the photogenerated current sources for the n-p junction diodes are not shown.

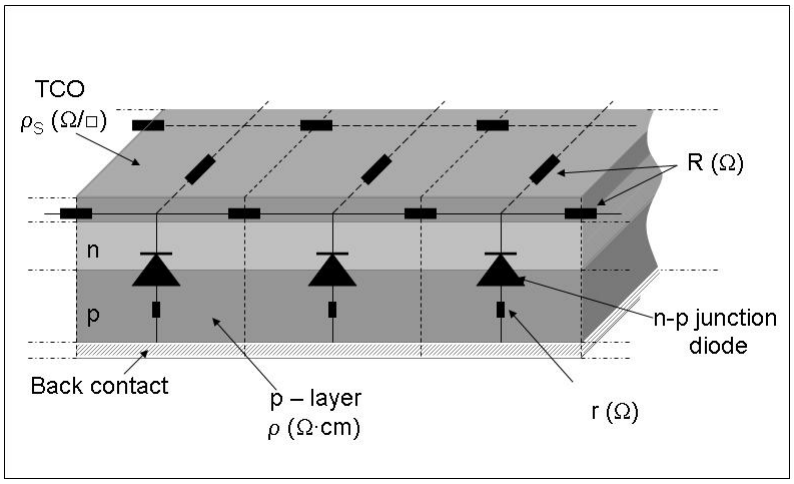

Fig.2.2. Cross-sectional perspective view of a subcell.

Figure 2.3 illustrates the schematic picture of the subcell. The illustrated subcell has dimensions of L (length) and W (width). For simulation purposes, the subcell is divided into N by M microcells with square bases. A uniform voltage is assumed across each microcell, but the voltage across different microcells will in general vary.

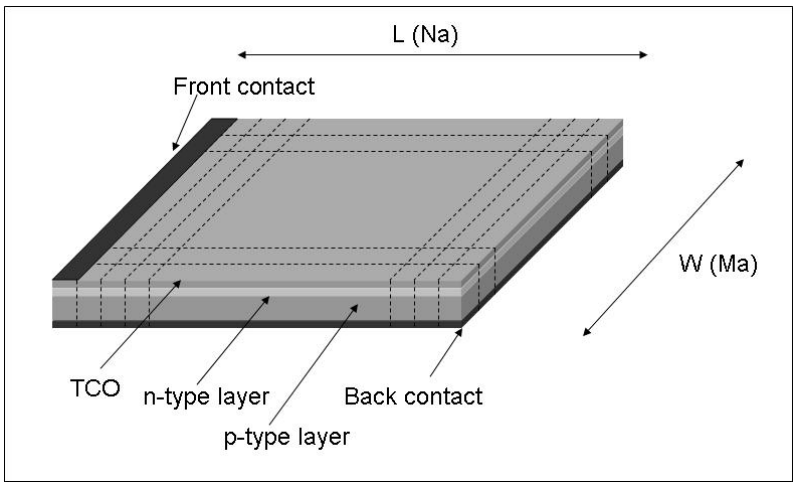

Fig.2.3. Schematic picture of a subcell.

The total current is collected by the front and back contacts shown. Within the model, the front contact represents a strip of negligible thickness and infinite conductivity. The back contact is also assumed to have zero resistance.

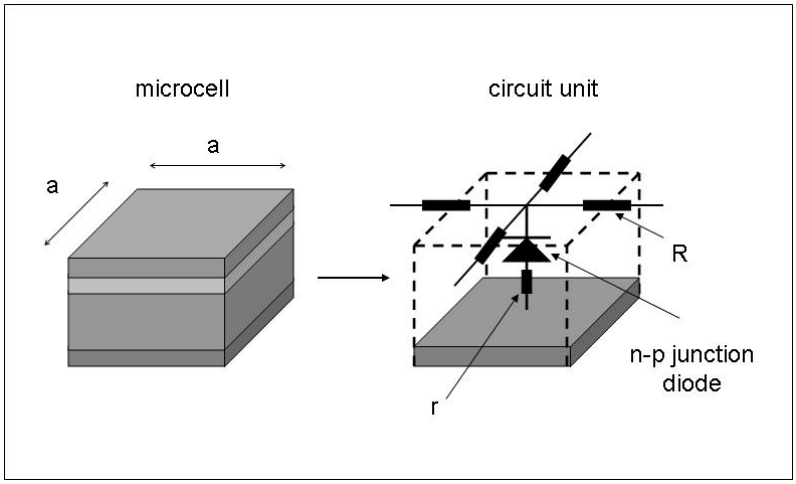

Fig.2.4. Schematic picture of a circuit unit.

Each microcell, which represents a discrete circuit unit, is modeled by four shared resistors *R*, bulk semiconductor resistance *r* and a diode, as in **figure 2.4**. The current source that accounts for light generated current is again not explicitly shown. Any

deviation of a microcell parameter in the circuit unit from that of the rest of the solar cell would indicate a spatial non-uniformity.

Simulations are performed in PSpice software[4]. Depending on the approach chosen, one can use either a diode and a current source or a numerical table of current vs. voltage values. Such a *J-V* table, referred to as a GTABLE in the PSpice software, is a numerical representation of a current-voltage curve and can include many modifications to the ideal diode and current source. Nevertheless, for simplicity diodes and current sources are used to visualize a microcell. **Figure 2.4** shows that one micro-diode accounts for an area $a \times a$, and therefore, $L = Na$ and $W = Ma$.

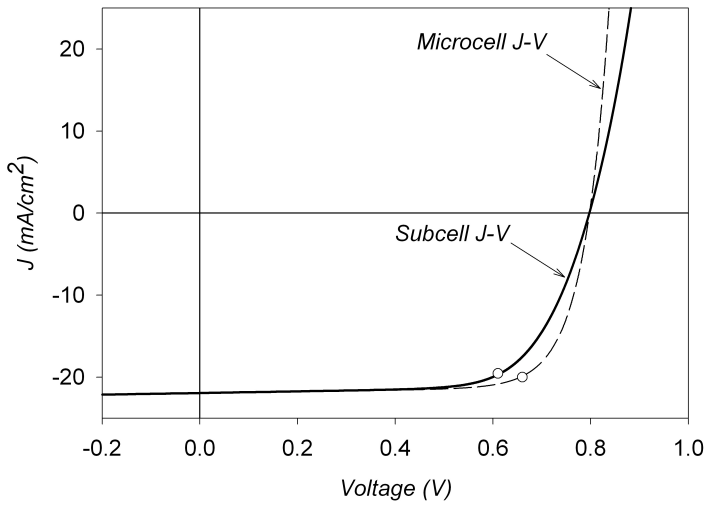

Fig.2.5. Baseline *J-V*s.

Baseline *J-V* curve of the microcell (dashed line) and the subcell (solid line) are illustrated in **figure 2.5**. The difference is due to the sheet resistance of the transparent top contact. Open circles in **figure 2.5** are maximum power points. Due to the distributed sheet resistance the *FF* of the subcell is less than that of the microcell, while V_{OC} and J_{SC} are unchanged. Basic solar cell parameters of the microcell and subcell are presented

below in **table 2.1.** In the uniform case, the subcell *J-V* is the same as cell and module *J-V*s.

Table 2.1. Basic solar cell parameters.

	η	FF	V_{OC}	J_{SC}	V_{MP}	J_{MP}	G	A	J_0
Units	(%)	(%)	(V)	(mA/cm^2)	(V)	(mA/cm^2)	(mS/cm^2)	-	(mA/cm^2)
Microcell	13.1	74.8	0.8	22.0	0.66	19.9	1	2	3.8E-6
Subcell	12.0	68.6	0.8	22.0	0.61	19.5	1	2	3.8E-6

2.2. TCO sheet resistance

For simulation purposes it is important to relate the sheet resistance ρ_S of the TCO layer to the discrete resistances *R* of the 2-D circuit model. The strategy to find such a relation is to calculate power losses due to lateral currents in the TCO layer for both continuous and discreet distributions of sheet resistance.

The bulk resistivity of a uniformly doped p-type semiconductor absorber, measured in (Ω·cm), is given by:

$$\rho = \left(q\mu_h p\right)^{-1}, \tag{2.1}$$

where *q* is the elementary charge, μ_h is the hole mobility and *p* is the hole density. Lateral resistance of the n-type TCO, however, is generally characterized by the sheet resistance ρ_S measured in Ω/sqr:

$$\rho_S = \left(tq\mu_e n\right)^{-1}, \tag{2.2}$$

where *t* is the thickness of the layer, μ_e is the electron mobility and *n* is the electron density.

Figure 2.6 shows a schematic picture of lateral currents in the TCO layer of a subcell. The thickness of the TCO layer is equal to *t*.

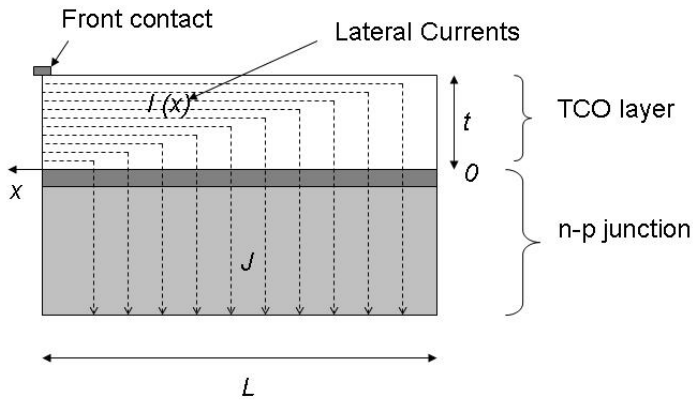

Fig.2.6. Schematic picture of lateral currents in TCO layer.

The *X*-axis shown in **figure 2.6** is defined such that the front contact is located at $x = 0$. To a good approximation the lateral current *I(x)* decreases linearly with *x* and is given by[5]:

$$I(x) = JW(x - L), \tag{2.3}$$

where *J* is the longitudinal current density. The resistance element *dR* is given by:

$$dR = \rho \frac{dx}{tW} = \left(\frac{\rho}{t}\right)\frac{dx}{W} = \rho_S \frac{dx}{W}. \tag{2.4}$$

Thus, the power loss per unit area *P* is:

$$P = \frac{1}{LW}\int_{x=0}^{x=L} I(x)^2 dR = \frac{1}{3}\left(\rho_S L^2\right)J^2. \tag{2.5}$$

Figure 2.7.a shows the circuit diagram of a single row of microcells (planar 1-D model). The voltage across each diode will vary, because of the non-zero voltage drop across the resistors, and therefore the currents through different diodes will be different.

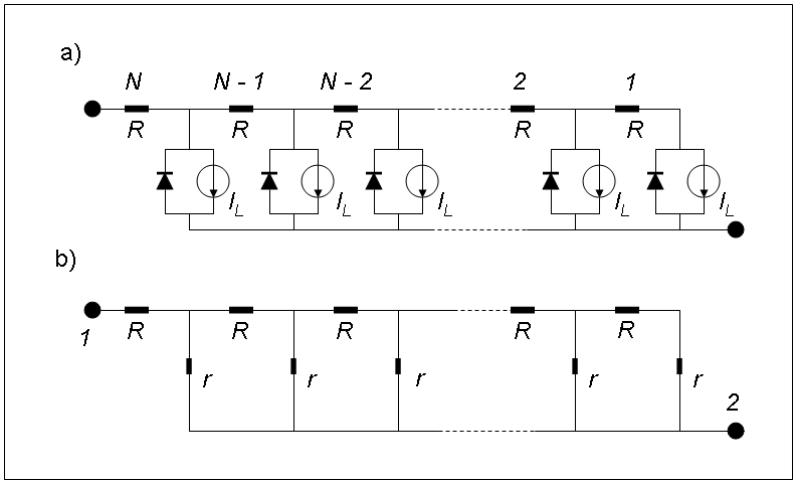

Fig.2.7. Circuit diagram of a single row (a) with diodes and current sources shown (b) with semiconductor resistors *r* emphasized.

However, to a good approximation for the purposes of power loss calculations, the current that flows through *n*-th resistor is equal to *nI*. Therefore, the power dissipated on *n*-th resistor is equal to $R(nI)^2$.

Thus, taking into account that there are *M* rows in the 2-D network, the dissipated power per unit area is given by:

$$P = \frac{M}{LW}\left(RI^2 \sum_{n=1}^{N} j^2 \right) = \frac{M}{LW} RI^2 \, \frac{N(N+1)(2N+1)}{6}. \qquad (2.6)$$

Setting the right-hand-sides of equations (2.5) and (2.6) equal to each other and taking into account that $I = Ja^2$, it follows that:

$$\rho_S = \frac{(N+1)(2N+1)}{2N^2} R. \qquad (2.7)$$

Here, in the limit of large N equation (2.6) reduces to:

$$P \cong \frac{1}{3}\left(RL^2\right)J^2, \tag{2.8}$$

which is independent of W, and equation (2.7) reduces to: ρ_S (Ω/sqr) ≅ R (Ω). For practical simulation purposes, N should be 20 or more.

2.3. Lumped series resistance approximation

The J-V behavior of a good-quality lab-scale thin-film solar cell can be described reasonably accurately by a general single exponential diode equation[3]:

$$J = J_0 \exp\left[\frac{q}{AkT}\left(V - R_S J\right)\right] + GV - J_L, \tag{2.9}$$

where J_0 is the reverse saturation current, q is the electron charge, A is the diode quality factor, T is the temperature, G is the shunt conductance, J_L is the light generated current, and R_S is the lumped series resistance. Equation (2.9) assumes a non-distributed TCO resistance in the solar cell, or, in other words, a circuit model where the TCO resistance is a single element. For a module-geometry cell, the lumped series resistance approximation is not very reliable and J-V curves can deviate significantly from equation (2.9). However, for small values of $\rho_S L^2$, equation (2.9) will closely follow the J-V curve obtained from the model with distributed TCO resistance. It is therefore important to find a relation between R_S and the material resistances and to define when $\rho_S L^2$ is sufficiently small that equation (2.9) is applicable.

The internal semiconductor absorber resistance r of a microcell in the 2-D model is inversely proportional to its physical base area a^2:

$$r = \frac{\rho b}{a^2}, \tag{2.10}$$

where b is the thickness of the bulk region of the absorber layer and ρ is the resistivity of the absorber layer.

Figure 2.7-b shows a single row of microcells (planar 1-D model) with the focus on TCO resistors R and semiconductor resistors r. Again, for visual clarity the diodes and current sources are not shown. The resistance R_{12} between points 1 and 2 is given by:

$$R_{12} = R \cdot g(\kappa, N), \tag{2.11}$$

where $\kappa = r/R$ and $g(\kappa,N)$ is a dimensionless factor given by the following recurrence relation:

$$\begin{aligned} g(\kappa, N) &= 1 + \left[\kappa^{-1} + g(\kappa, N-1)^{-1}\right]^{-1} \\ g(\kappa,1) &= 1 + \kappa. \end{aligned} \tag{2.12}$$

The full 2-D network has M rows and the series resistance R_S ($\Omega \cdot cm^2$) of the solar cell is therefore given by:

$$R_S\left(\Omega \cdot cm^2\right) = A\frac{R_{12}}{M} = AR\frac{g(\kappa, N)}{M}, \tag{2.13}$$

where A is the total area of the cell.

It is a straightforward exercise to find $g(\kappa,N)$ for the first few values of N, but for large N it is not tractable to give a general analytic expression. However, for fixed values

of L and W, in the limit of small a, which is equivalent to the limit of large r and large values of M and N, the $g(\kappa,N)/M$ -factor is approximately:

$$\frac{g(\kappa,N)}{M} \cong \frac{1}{M}\left(\frac{\kappa}{N}+\frac{N}{2}\right). \tag{2.14}$$

Using equations (2.10), (2.14) and the fact that $L = Na$, $W = Ma$, $A = NMa^2$, ρ_S (Ω/sqr) $\cong R$ (Ω) equation (2.13) can be reduced to:

$$R_S \cong \rho b + \frac{\rho_S L^2}{2}, \tag{2.15}$$

where the first and second terms are the contributions to the series resistance from the absorber and TCO layers respectively. One can estimate the first term in equation (2.15) with typical parameter values for a thin-film solar cell absorber layer: b = 2.5 μm, μ_h = 25 cm^2/Vs, $p = 10^{14} - 10^{16}$ cm^{-3} yield ρb = 0.003 to 0.3 $\Omega\cdot$cm^2. Thus, unless L is very small, the first term is much less than the second one, and therefore the series resistance is given by:

$$R_S \cong \frac{\rho_S L^2}{2}. \tag{2.16}$$

As an example, planar 1-D simulation of a uniform CIGS thin-film solar cell is performed in PSpice with the help of GTABLEs. The J-V curve for an individual GTABLE is obtained from normal 1-D simulation in AFORS HET[6]. The solar-cell parameters used in the normal 1-D AFORS-HET simulation of CIGS are taken from Ref. [7].

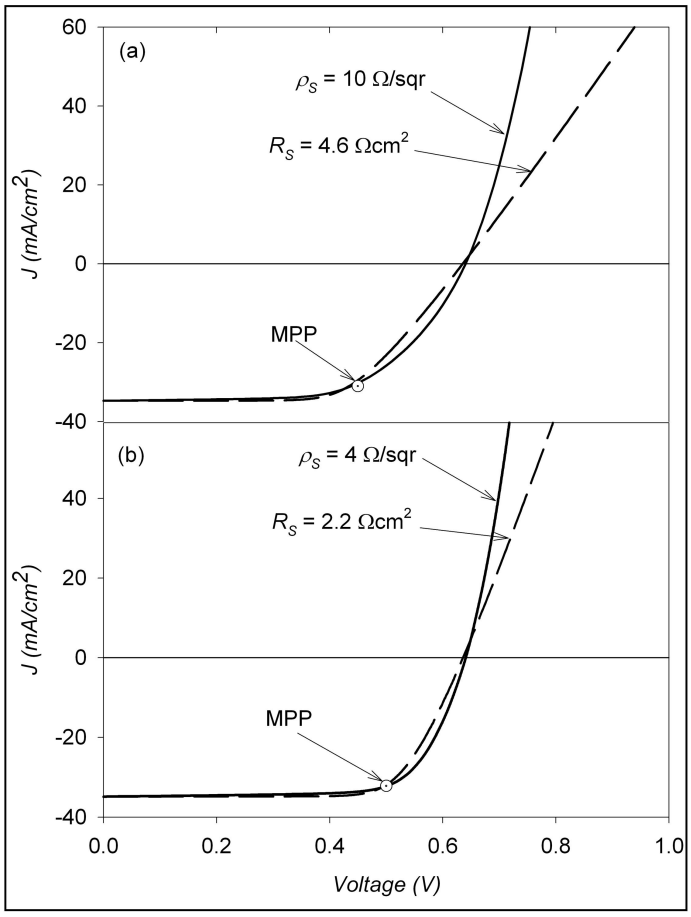

Fig.2.8. Comparison between distributed TCO planar 1-D and lumped R_S models for (a) large and (b) small ρ_S.

The solid curves in **figure 2.8-a** and **-b** represent *J-V* curves of the CIGS solar cell obtained from planar 1-D simulations for two different values of TCO sheet resistance ρ_S = 4 Ω/sqr and 10 Ω/sqr, with L = 1 cm. The basic solar-cell parameters of these *J-V* curves are given in **Table 2.2.**

Table 2.2.
Basic solar cell parameters.

ρ_S(Ω/sqr)	V_{OC} (V)	J_{SC} (mA/cm^2)	FF (%)	η (%)
4	0.64	34.9	72.3	16.2
10	0.64	34.8	61.2	13.6

The dashed lines in **figures 2.8-a** and **-b** are graphic representations of equation (2.9), which implies lumped series resistance R_S. This series resistance was chosen such that both solid and dashed *J-V* curves in each case have the same *FF*, or equivalently, the same maximum power point, which also implies that η is the same since V_{OC} and J_{SC} values match.

The values of R_S used were 4.6 and 2.2 Ω·cm^2 for ρ_S = 10 and 4 Ω/sqr respectively, which are close to those predicted by eq. (2.16): 5 Ω·cm^2 and 2 Ω·cm^2. For a non-zero value of the TCO sheet resistance, it is not possible to overlay the solid line with any dashed approximation. For decreasing ρ_S, the agreement of the two lines in the power quadrant becomes reasonably good, but less so in the first quadrant.

2.4. Dimensionless reduced-TCO sheet resistance

The TCO sheet resistance ρ_S primarily affects the *FF* and leaves V_{OC} and J_{SC} unchanged. The cell length *L* also strongly affects the fill factor, and hence the power loss, but the value of *W* has no effect upon the *J-V* curve for a uniform solar cell. The fractional power loss from the TCO layer also depends on the amount of lateral current J_{SC} and varies with V_{OC}. An empirical observation showed that the dimensionless

quantity $\delta = \rho_S L^2 J_{SC}/V_{OC}$ in fact determines the reduction in fill factor due to the sheet resistance to a reasonable approximation.

Figure 2.9 shows the calculated dependence of the ratio FF/FF_0 on δ, where FF_0 is the fill-factor of a microcell, or alternatively in the $\rho_S = 0$ limit.

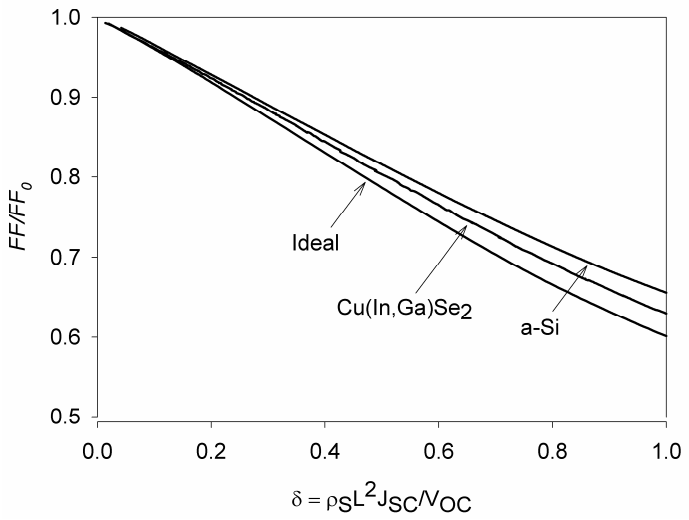

Fig.2.9. FF/FF_0 dependence on δ.

Figure 2.9 illustrates plots of FF/FF_0 for three different cells – two-junction a-Si, CIGS and ideal (high-efficiency). The basic solar cell parameters of these three cells are given in **Table 2.3.**

Table 2.3.
Basic solar cell parameters

Cell	V_{OC} *(V)*	J_{SC} *(mA/cm²)*	*FF (%)*	η *(%)*
a-Si	1.64	6.1	72.1	7.1
CIGS	0.64	34.6	79.5	18.8
Ideal	0.80	35.0	86.1	24.1

The fact that the three curves in **figure 2.9** generated for cells with significantly different parameters have the same shape, and are very similar numerically, suggests that to a good approximation the variable δ is in fact a global variable. Thus, it can be used to

describe the *FF* variation for non-gridded large cells or modules. **Figure 2.9** also implies that with higher quality cells, there will be a slightly greater effect of δ on the *FF*. Generally, the ratio FF/FF_0 for actual large-area cells and modules ranges from about 0.7 to 0.9, i.e. δ is between 0.2 and *0.5*. Within that range all three curves in the **figure 2.9** are close to each other and show near-linear behavior with a slope close to 0.38.

Thus, the chapter gives a detailed description of the three-step simulation framework. Several useful analytic and empirical results were obtained directly from the analysis of the uniform case. In particular, based on power dissipation in the TCO layer due to lateral currents, an analytic relation between model TCO resistors, discritization level N, and physical TCO sheet resistance ρ_S, was derived. A derivation of the expression for the lumped series resistance R_S of the uniform cell was also given. The lumped series resistance approximation was compared with the distributed TCO resistance approach (planar 1-D model) for small and large values of ρ_S. As is expected current voltage curves match well only for small values of ρ_S. A global parameter δ, which determines the *FF* of the cell, was introduced.

Chapter 3
Impact of shunts and weak-diodes on lab-scale solar cells

This chapter discusses the effect of shunts and weak-microdiodes on small size solar cells (subcells). In particular, power losses in a non-uniform subcell are identified and compared with those of the uniform with the help of pie charts. Variation of these power losses with sheet resistance ρ_S and light generated j_L current is studied. Power losses are studied both as a function of position in the subcell and in integral form. Also variation of the impact with location of the non-uniformity in the subcell is analyzed. Analytic methods were used where possible.

3.1. Origin of shunts and weak-diodes

3.1.1. Origins of shunts

Minimization of loss mechanisms remains a primary goal of research and development in many laboratories. One such loss mechanism, which under certain conditions can be a critical one, is the loss due to localized shunts. **Figure 3.1** illustrates a cross-section of a typical CdTe solar cell (not to scale) that has a filament-type shunt

along grain boundaries that connects the back contact metal directly to the TCO bypassing the p-n junction.

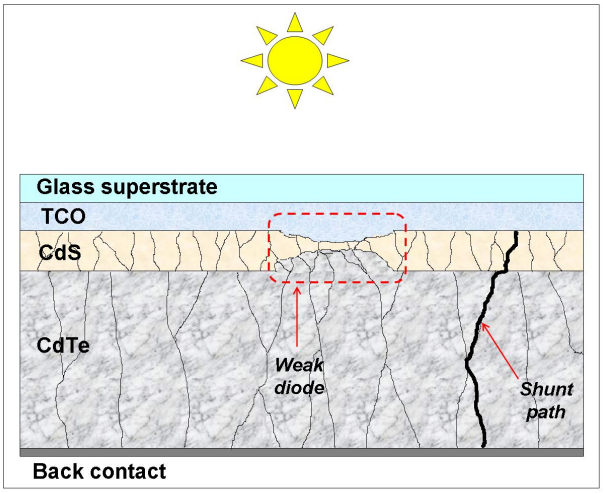

Fig.3.1. Schematic illustrating a shunt path and a weak diode in the CdS/CdTe structure.

Various imperfections in scribing techniques can result in localized shunt paths. In many cases, the shunts are not random but occur preferentially at cell cusps and grain-boundary corners along cell edges due to physical chipping from the scribing procedure[8]. Imperfection in the scribing procedure, however, is not the only cause of shunt paths in thin-film modules. Generally during deposition, thin-film growth produces a granular structure with the main grain axis perpendicular to the film plane. Penetration of the junction depletion layer throughout a module by such grain boundaries can also lead to shunting conductance[9]. Still, another mechanism that can cause localized shunt is a flaw during the deposition process of the layers, when the window layer is not properly deposited and is locally too thin or is not continuous. One of the primary goals of the current chapter is to understand the impact of localized-shunts on subcell performance. Another type of non-uniformity addressed in the current chapter is a weak-diode.

3.1.2. Origins of weak-diodes

The production of large area thin-film solar modules may lead to fluctuations of cell parameters such as defect density, band gap, doping density and layer thicknesses. Such fluctuations become increasingly important as devices get thinner, and they can have a significant negative effect on device performance when thickness fluctuations become comparable with the grain size. A thin window layer can result in insufficient coverage and formation of junctions between transparent-conducting-oxide (TCO) and absorber layers, which in turn can result in local reductions of voltage. Such local areas are commonly referred to as weak-diodes. The key physical parameter is the voltage of the weak-diode. **Figure 3.1** illustrates a cross-section of a typical CdTe solar cell (not to scale) that has a region with thin CdS layer, which results in a weak diode.

3.2. Effect of shunts on lab-scale solar cells

3.2.1. The setup

To analyze the effect of localized shunts on lab-scale (~ 1 cm^2) solar cells (subcell) the model of 12% efficiency CdTe solar cell, which was introduced in Chapter 2, was used. **Figure 3.2** shows the circuit diagram of the subcell with a central filament-type shunt in it. The shunt is modeled by a resistor (colored in red) across one of the microdiodes. For visual simplicity current sources are not shown in **figure 3.2**.

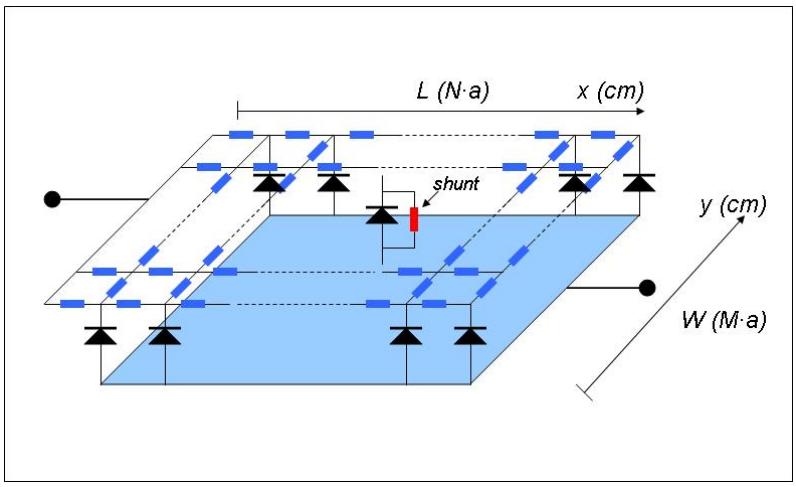

Fig.3.2. Circuit diagram of the subcell with a central shunt

There may also be a distributed shunt of the subcell among all microcells. Again for visual simplicity resistors accounting for the distributed shunt are not shown in **figure 3.2**.

3.2.2. Examples of shunted subcells and characteristic parameters of shunted subcell *J-V* curves

Figure 3.3 shows examples of *J-V* curves of shunted subcells with a filament-type shunt located in the center of the subcell. A filament-type shunt is modeled by a single shunt resistor over one of the microdiodes as shown in **figure 3.2**. A non-filament-type-shunt over a larger physical area can be modeled by several shunt resistors across many neighboring microdiodes. In the discussion to follow a filament-type shunt is assumed. For ease of discussion the severity of the shunt is characterized by the efficiency of the shunted subcell, though the actual parameter that is being changed in the circuit is the conductance of the shunt.

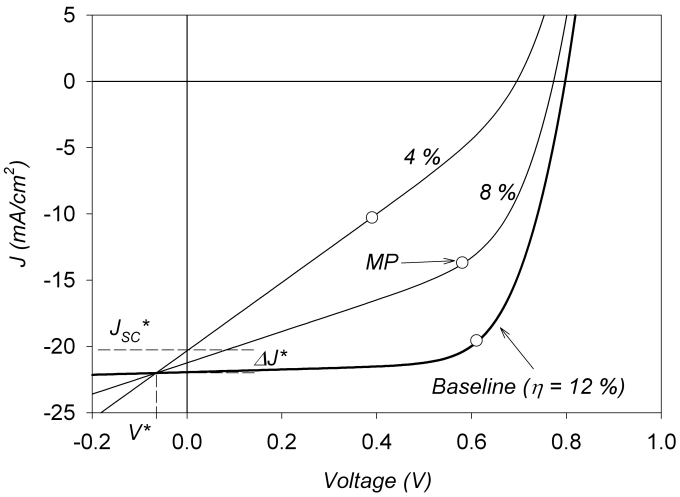

Fig.3.3. Examples of subcell *J-V* curves with a central shunt.

Figure 3.3 shows *J-V* curves of CdTe subcells with different efficiencies – 4, 8 and 12%, with latter being the baseline. To generate these curves, the conductance of the shunt located across the central microdiode was varied, for instance to get η = 8%, a shunt conductance of 11.8 mS is required. Open circles show maximum power points (MPP).

Figure 3.3 also shows characteristic parameters of shunted *J-V* curves, V^*, J_{SC}^* and ΔJ^*. An approximate analytic interpretation of these characteristic parameters can be obtained from the simple analysis of the single diode equation that includes parasitic resistances[3]:

$$J = J_0 e^{\beta(V - R_S J)} + G(V - R_S J) - J_L, \tag{3.1}$$

where J_0 is the saturation current, R_S is the series resistance, $G = 1/R_{SH}$ is the conductance and R_{SH} is the shunt resistance, J_L is the light generated current, and $\beta = q/AkT$.

Parameter J_{SC}* is basically the short-circuit current of the shunted subcell. With V = 0 in equation (3.1):

$$J_{SC}* = J_0 e^{-\beta R_S J_{SC}*} - G R_S J_{SC}* - J_L . \tag{3.2}$$

Neglecting the first term in (3.2) and rearranging the other terms:

$$J_{SC}* \cong -\frac{J_L}{1+GR_S}. \tag{3.3}$$

Equation (3.3) can also give a rough estimate of the conductance G from the experimental or simulated J-V curve.

Next, from equation (3.3):

$$\Delta J* = J_L - \left| J_{SC}* \right| = J_L \frac{GR_S}{1+GR_S}. \tag{3.4}$$

Since parameters V*, J_{SC}* and ΔJ* characterize behavior of the shunted J-V curve in its linear regime, equation (3.1) can be simplified in this range to:

$$J \cong G\left(V - R_S J\right) - J_L . \tag{3.5}$$

Rearranging the terms in (3.4) we get:

$$J \cong \frac{G}{\left(1+R_S G\right)} V - \frac{J_L}{\left(1+R_S G\right)}. \tag{3.6}$$

Setting J = - J_L and simplifying:

$$V^* = -J_L R_S . \tag{3.7}$$

Thus, equations (3.3), (3.4), (3.6) and (3.7) give approximate analytic interpretations of characteristic parameters V^*, J_{SC}^* and ΔJ^*. The derivations given above imply two primary approximations: 1. the exponential part of the *J-V* curve is neglected, that is a linear regime is in place; 2. the non-distributed series resistance model implied by diode equation is applied (3.1).

3.2.3 Shunt location analysis

In examples of shunted subcells given in the section above the shunt resistor is located in the center of the subcell. A shunt, however, can be located anywhere in the subcell with different probabilities depending on its physical origin and/or the mechanism that caused the shunt during the production process. From the symmetry of the problem, it follows that only variations along *X*-axis matter; variation in the *Y* direction simply implies redefinition of the subcell and shifting its borders along the cell. In that respect the front contact gridline serves as a reference line. **Figure 3.4** illustrates *J-V* curves of subcells with shunts at different locations – next to the gridline (1), in the center (2) and opposite the gridline (3). The black solid line is the baseline *J-V* curve of the uniform subcell for reference. **Table 3.1** shows basic solar cell parameters of these four subcells.

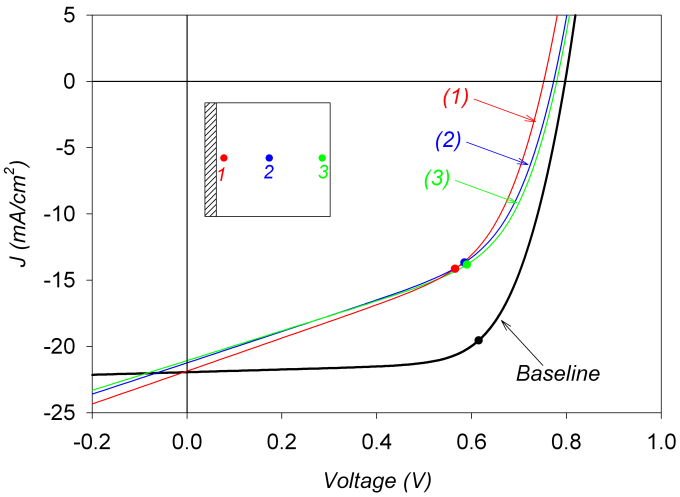

Fig.3.4. Subcell *J-V* curves with shunts at different locations.

Table 3.1.
Basic solar cell parameters

	V_{OC} (V)	J_{SC} (mA/cm^2)	FF (%)	η (%)
Baseline	0.80	22.0	68.7	12.0
(1) Close to the gridline	0.75	21.9	48.6	8.0
(2) In the center	0.77	21.2	48.7	8.0
(3) Opposite the gridline	0.78	21.1	49.7	8.2

Both **table 3.1** and **figure 3.4** imply that the location of the shunt makes only a minor difference. There is a small advantage when the shunt is located opposite the gridline. A subcell with the shunt away from the gridline has higher efficiency than the subcell with a shunt in the center for three reasons in order of importance:

(i) The power dissipation in the shunt resistor is higher towards the gridline because the lateral current is higher towards the gridline.

(ii) Essentially for the same reason, there is more power dissipation in the TCO layer near the gridline due to the lateral currents that were diverted from their original path towards the shunt.

(iii) Finally, simply from geometrical considerations, a center has more capability of degrading the performance of more neighboring microdiodes than when it is at the edge.

The same arguments explain why a subcell with the shunt in the center has better performance than a subcell with the shunt next to the gridline. However, there is an additional effect: when the shunt is located next to the gridline it tends to draw current not only from neighboring areas through TCO but also from the gridline that is highly conductive and the advantage of TCO screening vanishes. The TCO screening effect will be considered in more detail in the sections to follow.

3.2.4. Microcell voltage and current density profiles

Even in the uniform cell, due to the voltage drop in the distributed TCO sheet resistance, microdiodes in the subcell operate at different voltages. When the subcell is biased at its maximum power voltage (subcell V_{MP}) microdiodes in that subcell are biased at a range of different voltages close to maximum power voltage of the microcell (microcell V_{MP}). Thus, microcells in a subcell will generate different amounts of power. Therefore, it is worthwhile to look at the variation of microcell operating parameters with position along the *X*-axis. Obviously, in the uniform case there will be no variation in *Y* direction.

In this aspect the operating voltage of the microdiode is the primary parameter. The profile of microdiode operating voltages can be obtained numerically with PSpice.

However, an approximate analytic result would be helpful to understand the general behavior and its mathematical interpretation.

Since for uniform analysis there is no variation in *Y*-axis we can consider a single row of microdiodes (planar 1-D model). **Figure 3.5** illustrates a circuit diagram of one such row of microdiodes.

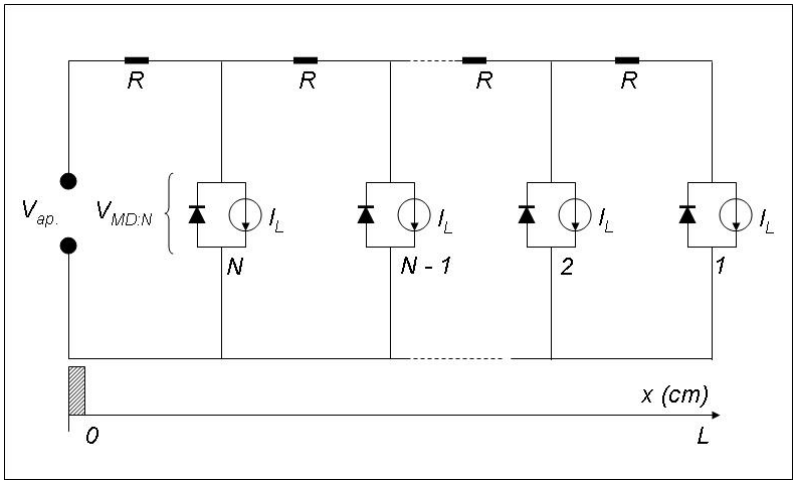

Fig.3.5. Schematic of the single row of microcells.

From **figure 3.5** it follows that the voltage across the *N-th* microdiode $V_{MD:N}$ is given by:

$$V_{MD:N} = V_{ap.} + R\left\{ NI_L - \sum_{j=1}^{N} I_{MD:j} \right\}. \tag{3.8}$$

In equation (3.8) $V_{ap.}$ is the voltage applied to the subcell, *R* is the resistor that represents TCO sheet resistance, *N* is the total number of microcells in one row, I_L is the light generated current of each microcell, and $I_{MD:j}$ is the forward current of the *j-th* microdiode given by:

$$I_{MD:j} = I_0 e^{\beta V_{MD:j}} \tag{3.9}$$

, where I_0 is the microdiode saturation current and $\beta = q/AkT$, and $j = 1...N$. The saturation current I_0 can be expressed in terms of the open-circuit voltage V_{OC} as follows:

$$I_0 = I_L e^{-\beta V_{OC}} . \tag{3.10}$$

Substituting (3.8) and (3.9) into (3.10) and rearranging the terms we get:

$$V_{MD:N} = V_{ap.} + RI_L \left\{ N - \sum_{j=1}^{N} e^{\beta\left(V_{MD:j} - V_{OC}\right)} \right\}. \tag{3.11}$$

In the same way from **figure 3.5** it follows that:

$$V_{MD:N-1} = V_{MD:N} + RI_L \left\{ (N-1) - \sum_{j=1}^{N-1} e^{\beta\left(V_{MD:j} - V_{OC}\right)} \right\}. \tag{3.12}$$

Recurrent relations (3.11) and (3.12) can be solved numerically to give the profile of microdiode voltages across the subcell from the gridline to the edge. Exponential terms in both (3.11) and (3.12) do not allow an exact analytic solution. However, at the maximum power voltage of the subcell $V_{ap.} = V_{MP\text{-}Subcell}$, which in fact is the voltage of the most interest, one can obtain a first-order analytic approximation. If $Vap. = V_{MP\text{-}Subcell}$ then $V_{MD:j} \approx V_{MP\text{-}Microcell}$ for all values of j. Since $V_{OC} > V_{MP\text{-}Microcell}$ exponential terms in (3.11) and (3.12) can be neglected. Thus, for (3.11) and (3.12) we get:

$$V_{MD:N} \cong V_{ap.} + RI_L N, \tag{3.13}$$

$$V_{MD:N-1} \cong V_{MD:N} + RI_L (N-1). \tag{3.14}$$

Substituting the microdiode voltages from (3.13) and (3.14) into (3.11) and (3.12), one can get second order approximation. In principle, repeating that iterative process an approximation of any order can be obtained. However, the main purpose for deriving equations (3.13) and (3.14) is to illustrate the semi-quantitative behavior of the microdiode voltage profile across the subcell from the gridline to the edge at the maximum power voltage of the subcell. Using the numerical values given in **table 3.1**, numerical parameters of the subcell mentioned in the baseline section and equations (3.13) and (3.14) one can plot the first order analytic approximation of the microdiode voltage profile across the subcell.

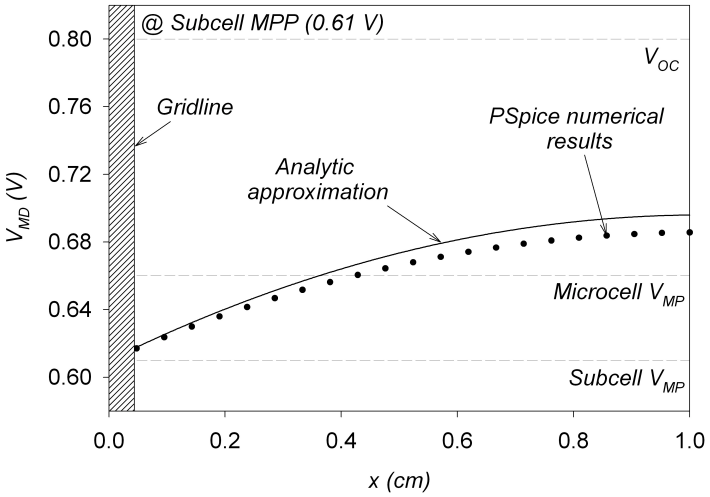

Fig.3.6. Microdiode voltage profile in the uniform subcell (at V_{MP}).

The dots in **figure 3.6** illustrate microdiode voltage profile obtained from PSpice numerical simulation, the solid line shows the first order analytic approximation, and for

reference purposes the dashed straight lines represent characteristic voltage levels: V_{OC}, microcell V_{MP} and subcell V_{MP}. It is worthwhile to note that the analytic approximation presented above is valid for a limited range of voltages applied to the subcell, those when the exponential terms can be neglected. Fortunately, that is the case for the subcell maximum power voltage. In principle, one can get the same voltage profile by solving following differential equations with appropriate boundary conditions[10,11]:

$$\frac{dJ}{dx} = -j_0\left(\exp\left(\frac{qV}{AkT}\right)-1\right)+ j_L, \tag{3.15}$$

$$J = -\frac{1}{\rho_S}\frac{dV}{dx}, \tag{3.16}$$

where J is the current in the resistive electrode. However, that set of differential equations has no general analytic solution, and can only be solved analytically for a limited range of parameters. Thus, the numerical approach is preferred in general.

Figure 3.7 illustrates a 3-D profile of microdiode operating voltages in the subcell with a shunt in the center, when the subcell is biased at the shunted-subcell-V_{MP}. Because of the shunt, there is a variation in microdiode operating voltage not only in X-direction but also in Y-direction. Hence, there is no credible planar 1-D approach applicable to problems with spatial non-uniformities, and only 2-D numerical simulations can reveal the useful information.

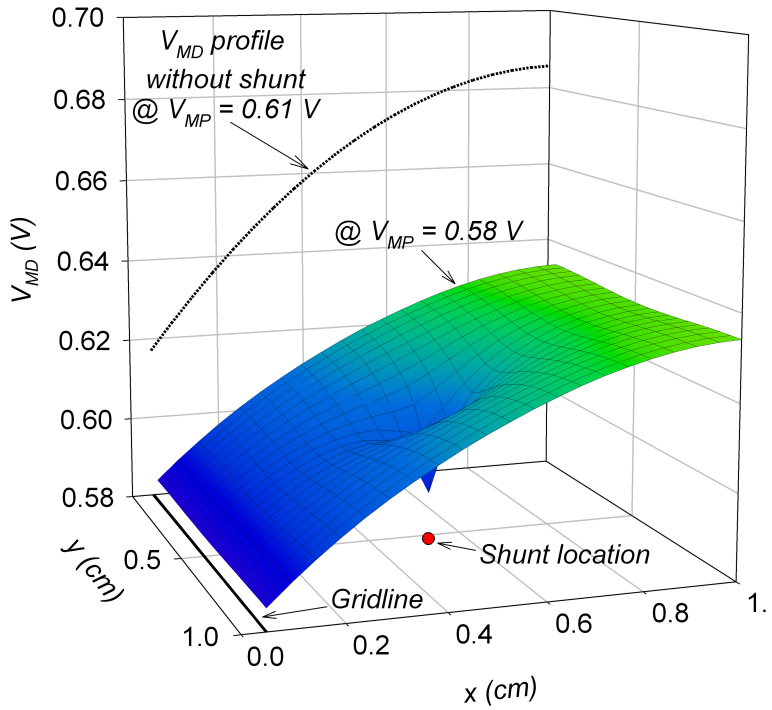

Fig.3.7. 3-D profiles of microdiode operating voltages in the subcell with a central shunt.

For reference, **figure 3.7** also shows a solid line that represents profile of microdiode operating voltages of the uniform subcell at the uniform-subcell values of V_{MP}. **Figure 3.7** shows that not only the voltage near the shunt is reduced but also that the entire subcell has a lower voltage. The latter is primarily due to the fact that the shunted subcell is biased at shunted-subcell-V_{MP} (0.58 V) which is lower than the uniform-subcell-V_{MP} (0.61 V).

Figure 3.8 shows the analogous graph, obtained from numerical analysis with PSpice, as in **figure 3.6**, but in this case for current density. For reference purposes dashed lines represent characteristic current density levels: subcell J_{SC}, microcell J_{MP}, and subcell J_{MP}.

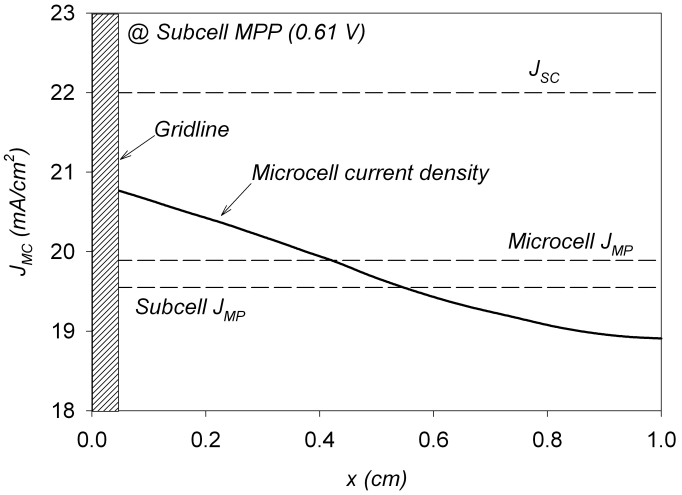

Fig.3.8. Microdiode current density profile in the uniform subcell (at V_{MP}).

One can also reproduce a 3-D analog of **figure 3.8** for the shunted subcell case, but that will be omitted here.

3.2.5. Microcell power density profiles

The variations in operating voltage and current density of the microdiodes can be combined to show the variation in generated power. That variation in the uniform subcell is illustrated in **figure 3.9**. The solid line in **figure 3.9**, obtained from numerical analysis with PSpice, represents the profile of the microcell power density. Dashed lines represent microcell and subcell maximum power density levels. The solid line shows that even though the subcell is biased at its subcell V_{MP}, microcells do not operate at their full capacity. Only microcells at $x \sim 0.4$ cm reach their maximum power, because as is seen in **figure 3.6** at $x \sim 0.4$ cm microdiodes operate at microcell V_{MP}. That difference will be

referred to as “power lost due to variation in microdiode operating voltage” (P_{MD}) and will be discussed in more detail in the following section.

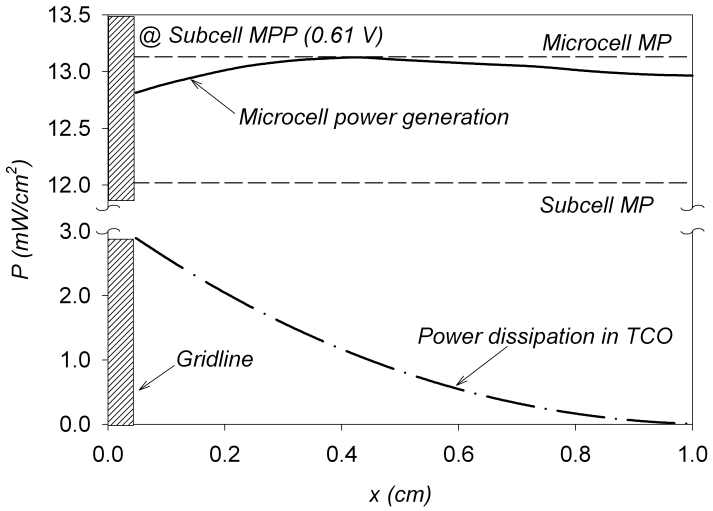

Fig.3.9. Power density profiles in the uniform subcell (at V_{MP}).

The dash-dot line in **figure 3.9** represents the power density dissipated in the TCO layer. **Figure 3.9** shows that even though the TCO sheet resistance is uniform over the subcell area, the power density dissipated in the TCO layer, P_{TCO}, decreases monotonically (as ~ x^2) from the gridline to the edge of the subcell. This is because the density of lateral currents that flow in TCO increases linearly from the edge to the gridline. Clearly P_{MD} and P_{TCO} are separate quantities and must be handled individually.

3.2.6. Integrated power losses in the subcell

Figure 3.10 illustrates 3-D surfaces representing the spatial dependence of power loss densities associated with dissipation in TCO, $P_{TCO}(x,y)$, and the variation in microdiode operating voltage, $P_{MD}(x,y)$, for two different situations: a.) Non-shunted

subcell at uniform-subcell-V_{MP} and b.) Shunted subcell at shunted-subcell-V_{MP}. For $P_{MD}(x,y)$ the reference level is the maximum power density of the microcell – 13.1 mW/cm^2 as in **figure 3.9**.

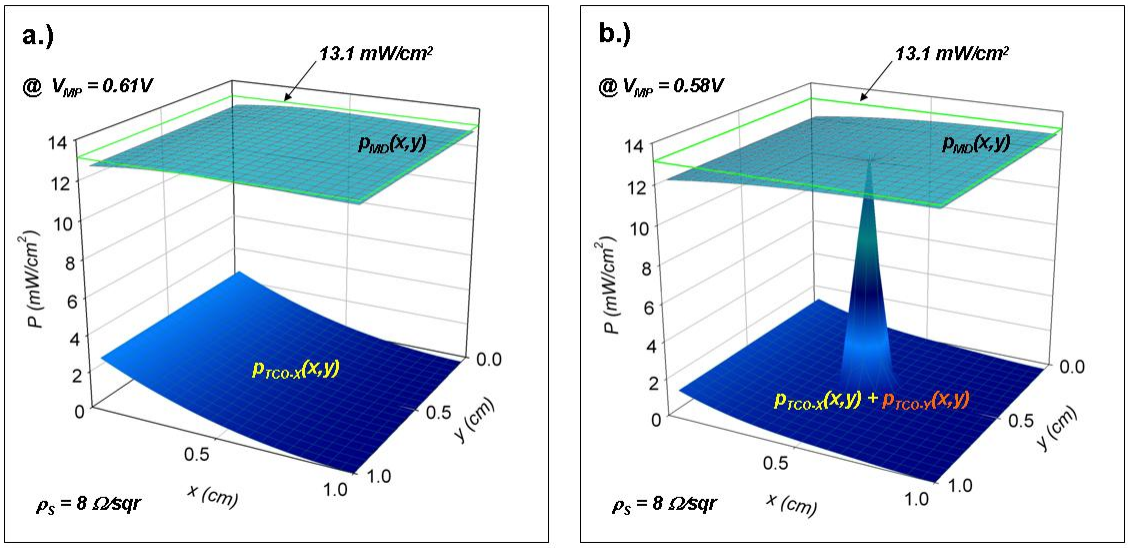

Fig.3.10. 3-D power loss profile P_{MD} and P_{TCO} for a) uniform and b) shunted cases.

X and *Y* subscripts in **figure 3.10** refer to the direction in which lateral currents flow and produce power dissipation in the TCO. In the uniform subcell case, there is no lateral current flow in *Y* direction in the TCO layer, and therefore **figure 3.10-a** shows only $P_{TCO\text{-}X}(x,y)$. When there is a shunt, some lateral current flows in the *Y* direction, thus, causing power dissipation loss $P_{TCO\text{-}Y}(x,y)$. Therefore, the 3-D surface with a spike in **figure 3.10-b** accounts for both $P_{TCO\text{-}X}(x,y)$ and $P_{TCO\text{-}Y}(x,y)$. The effect of current diversion towards the shunt is also known as current crowding effect. While **figure 3.10-a** shows all power losses in the subcell, **figure 3.10-b** must also include the power dissipation in the shunt. This term is shown in **figure 3.11**, and can be large compared with other power losses.

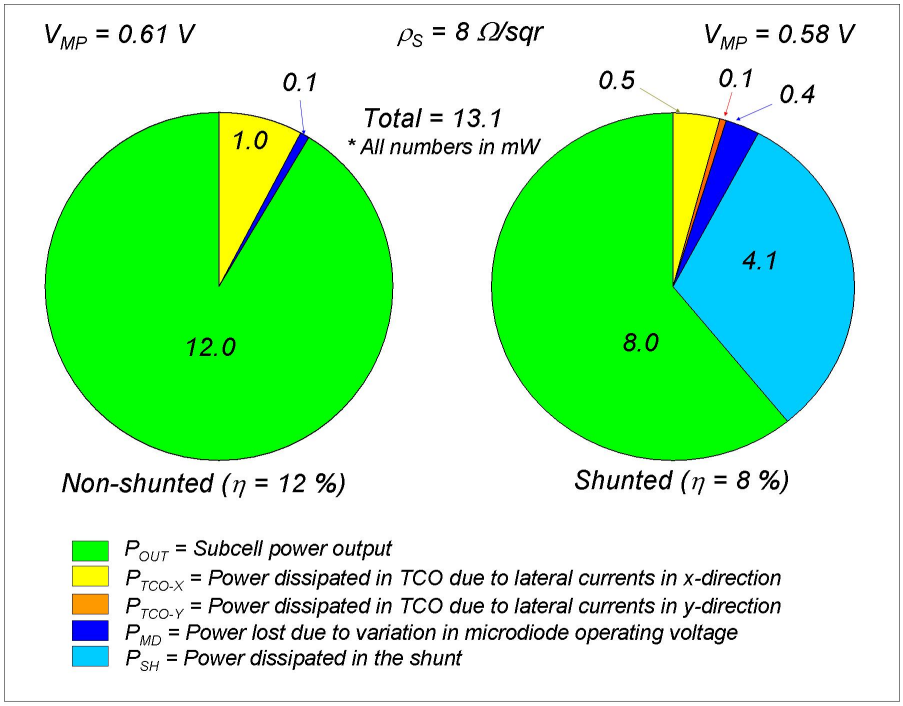

Fig.3.11. Integrated power losses in non-shunted and shunted subcells (ρ_S = 8 Ω/sqr).

Figure 3.11 shows pie charts of power losses integrated over the subcell surface area for two cases: the uniform subcell (η = 12%) and the shunted subcell (η = 8%) at their respective values of V_{MP}. The pieces in both pie charts add up to 13.1 mW, which is the maximum generated power of an ideal subcell with zero TCO sheet resistance. In the uniform subcell case, dissipation in the TCO layer P_{TCO} accounts for a substantial loss (~ 8%), while P_{MD} (~ 1%) is a relatively minor factor. In the shunted-subcell case power dissipation in the shunt P_{SH} accounts for most of the power loss (~ 30 %), while P_{TCO} (~ 5%) and P_{MD} (~ 3%) are secondary, though non-negligible, factors. Even though the amount of the power dissipated in the shunt is modest (4.1 mW), the power density can be very large depending on the physical area of the shunt. For instance, if the physical area of the shunt is about the area of the cone base in **figure 3.10-b** then the power

density is 0.52 W/cm^2; if it is on the order of a microcell area then the power density is 2.3 W/cm^2; if it is a grain-size shunt (1 μm^2) then the density can reach up to 0.5 MW/cm^2.

If the power density in the shunt is very high, as in the last example, the local temperature can be very high and the properties of the shunt may be significantly altered. Additionally, for the shunted-subcell case $P_{TCO\text{-}X}$ (~ 4%) is somewhat larger than $P_{TCO\text{-}Y}$ (~ 1%) which means that currents are being diverted towards the shunt from near-by regions only. Power dissipation in the TCO layer in the uniform-subcell case (1.0 mW) is larger than in the shunted-subcell (0.6 mW) because in the latter case a significant percentage of lateral currents does not flow through the whole original path in TCO causing power dissipation and is instead diverted towards the shunt. Comparison of P_{MD}-s for both cases is not straightforward because it involves consideration of both TCO sheet resistance ρ_S and shunt conductance G_{SH} at the same time, which is a non-trivial non-linear problem where the outcome may vary depending on the product of $\rho_S \cdot G_{SH}$.

3.2.7. TCO sheet resistance variation

Obviously, TCO sheet resistance ρ_S is one of the major factors, and it is worthwhile to see how variation in ρ_S affects the overall power loss picture. For that purpose, **figure 3.12** illustrates uniform-subcell *J-V* curves for two values of ρ_S, 8 and 16 Ω/sqr. The dashed line in **figure 3.12** is the microcell *J-V* curve, which is the same for both cases, and open circles are maximum power points. The higher TCO sheet resistance

results in a greater *FF* reduction which in turn results in an additional efficiency drop from 12% to 11%.

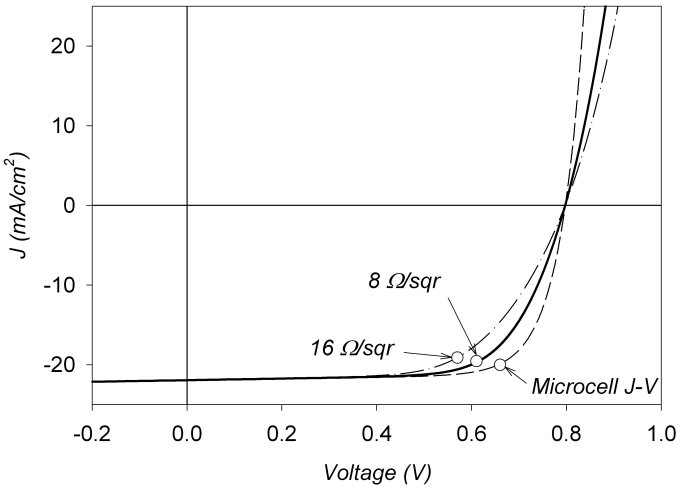

Fig.3.12. Uniform-subcell *J-V* curves for different values of ρ_S = 8 and 16 Ω/sqr.

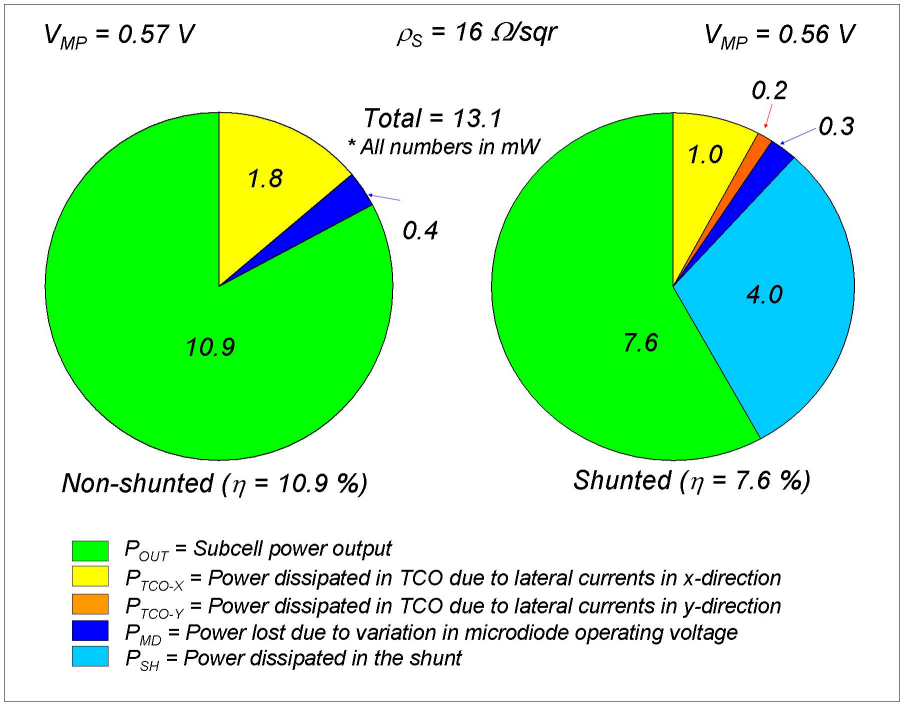

Fig.3.13. Integrated power losses in non-shunted and shunted subcells (ρ_S = 16 Ω/sqr).

Figure 3.13 is analogous to **figure 3.11** but for the larger value of sheet resistance. For both uniform and shunted subcells, P_{TCO} has essentially doubled, but P_{SH} is reduced due to the better TCO screening effect. For the uniform subcell case, P_{MD} has also increased, because higher ρ_S results in a larger spread in microdiode operating voltages. It is less affected, however, in the shunted-subcell case. Straightforward comparison of **figures 3.11** and **3.13** may be slightly misleading, since P_{TCO} does not increases quite linearly with ρ_S, as seen in **figure 3.14**. **Figure 3.14-a** shows the integrated power losses P_{TCO} and P_{MD} for uniform-subcell case as a function of TCO sheet resistance. **Figure 3.14-a** implies that for small values of ρ_S (< 10 Ω/sqr) P_{MD} is a relatively minor compared to P_{TCO}, while for larger values of ρ_S it begins to play a major factor. The sum of P_{TCO} + P_{MD} increases semi-linearly with ρ_S, which implies that the efficiency decreases semi-linearly with sheet resistance. **Figure 3.14-b** illustrates that the power dissipated in the shunt P_{SH} decreases semi-linearly with ρ_S which demonstrates TCO screening effect, though the rate of screening is relatively modest. **Figure 3.14-b** also shows that P_{MD} stays essentially constant with sheet resistance.

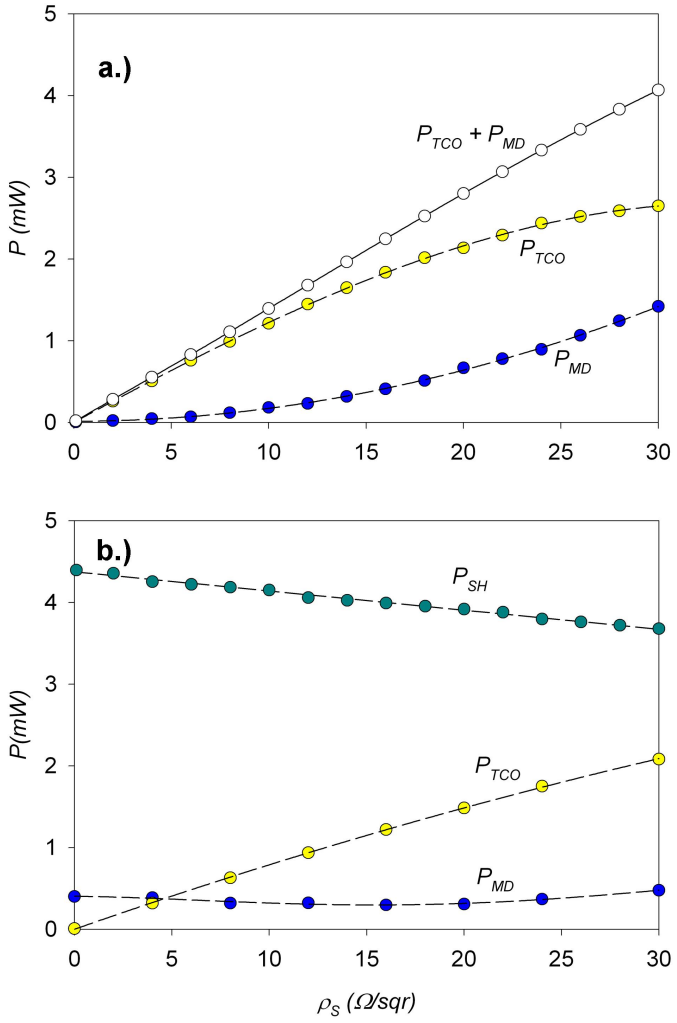

Fig.3.14. Integrated power losses as a function of ρ_S.

3.2.8. CdTe vs. CIGS

The amount of light generated current is another important parameter that significantly affects power losses. The effect of increased light generated current on power losses can be observed with the example of a low bandgap solar cell like CIGS.

Figure 3.15 shows comparison of baseline microcell (dashed) and uniform subcell (solid) *J-V* curves of CdTe and CIGS, assuming ρ_S = 8 Ω/sqr in both cases.

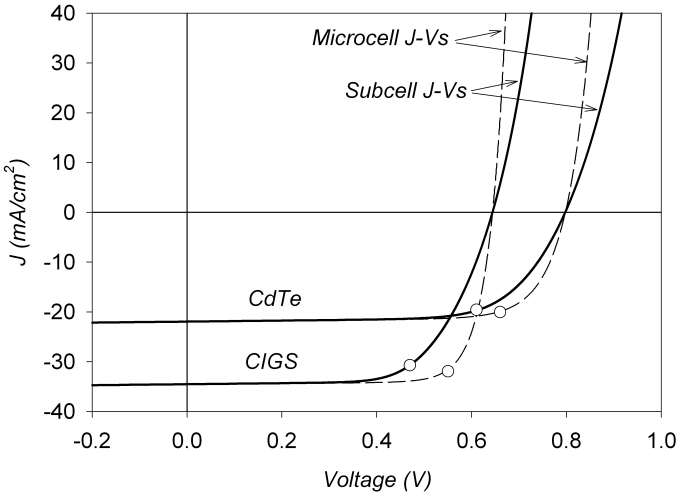

Fig.3.15. Comparison of CdTe and CIGS microcell and subcell *J-V*, ρ_S = 8 Ω/sqr in both cases.

Table 3.2 shows numerical values of both CdTe and CIGS microcells and subcells. Even though the V_{OC} of the CIGS is smaller, its J_{SC} is ~1.6 times larger, which is important for present analysis.

Table 3.2. Basic parameters of CdTe and CIGS microcells and subcells.

		η	*FF*	V_{OC}	J_{SC}	V_{MP}	J_{MP}	*G*
	units	(%)	(%)	(V)	(mA/cm^2)	V	(mA/cm^2)	(mS/cm^2)
CdTe	***Microcell***	13.1	74.8	0.80	22.0	0.66	19.9	1
	Subcell	12.0	68.6	0.80	22.0	0.61	19.5	1
CIGS	***Microcell***	17.4	78.1	0.64	34.6	0.55	31.9	1
	Subcell	14.4	64.9	0.64	34.5	0.47	30.7	1

Figure 3.16 shows pie-charts of integrated power losses in uniform CdTe and CIGS subcells. In both cases TCO sheet resistance was fixed at 8 Ω/sqr.

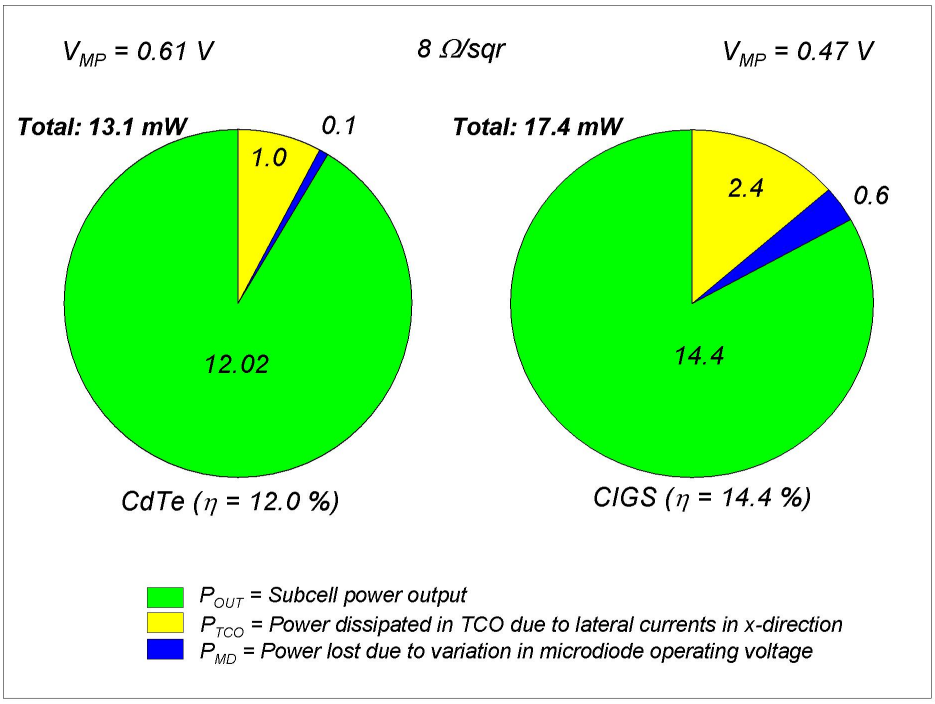

Fig.3.16. Integrated power losses in uniform CdTe and CIGS subcells.

The fact that P_{TCO} in CIGS (2.4 mW) is ~ 2.4 times larger than in CdTe (1 mW) is because $P_{TCO} \sim J_{MP}^2$ and $(J_{MP\text{-}CIGS}/J_{MP\text{-}CdTe})^2 = (30.7/19.5)^2 \sim 2.5$. However, there is no simple quantitative explanation as to why P_{MD} is ~ 6 times larger in CIGS. A qualitative explanation would be to say that since the P_{TCO} in CIGS is larger, the spread of microdiode operating voltages in CIGS is larger than in CdTe.

Figure 3.17 shows pie-charts of integrated power losses in equally shunted CIGS and CdTe subcells. It illustrates that overall CIGS (total loss – 21%) is more tolerant to the same shunt than CdTe (total loss – 39%).

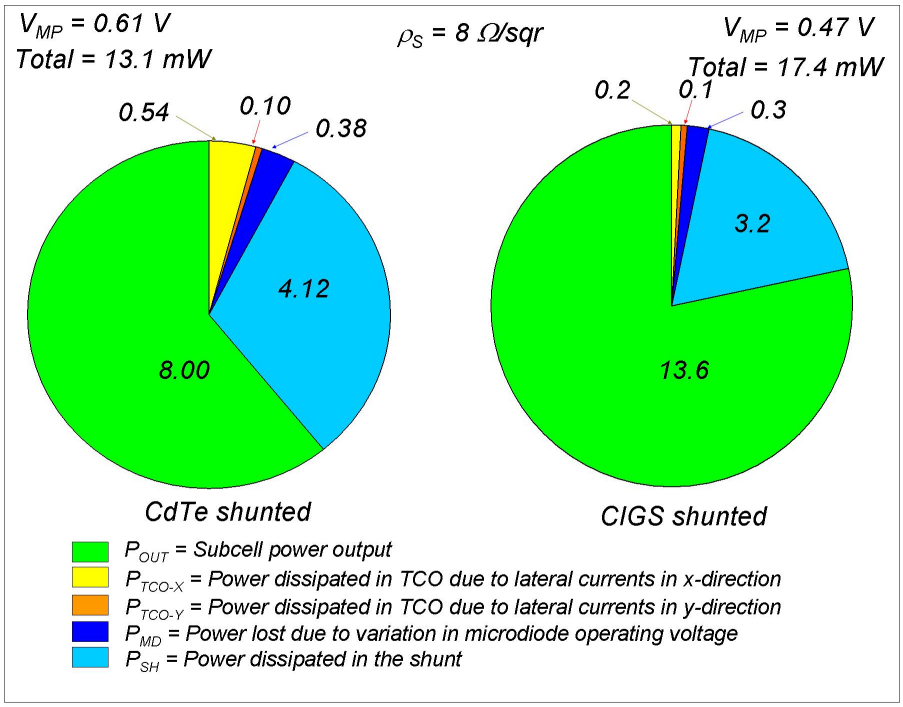

Fig.3.17. Integrated power losses in shunted CdTe and CIGS subcells.

This can partially be explained by the fact that the screening length in both cases is different. A simple approximate relation of the screening length of the dead shunt to basic solar cell parameters is given in Ref. [13]:

$$L_{SC} \propto \sqrt{\frac{V_{OC}}{J_L \rho_S}}. \tag{3.17}$$

Using values in **table 3.2** and equation (3.17) we get $L_{SC\text{-}CdTe}/L_{SC\text{-}CIGS} \sim 1.4$, which means that CIGS has a smaller screening length and therefore has better shunt-screening capability than CdTe. This also explains why $P_{SH\text{-}CdTe} > P_{SH\text{-}CIGS}$.

3.3 Effect of weak-diodes on lab-scale solar cells

3.3.1 Examples of subcell *J-V* curves with one weak microdiode in the center

Figure 3.18 illustrates the circuit diagram of the subcell with a weak microdiode in the center. As in the case of shunt in the **figure 3.2**, here again current sources are not shown for visual simplicity.

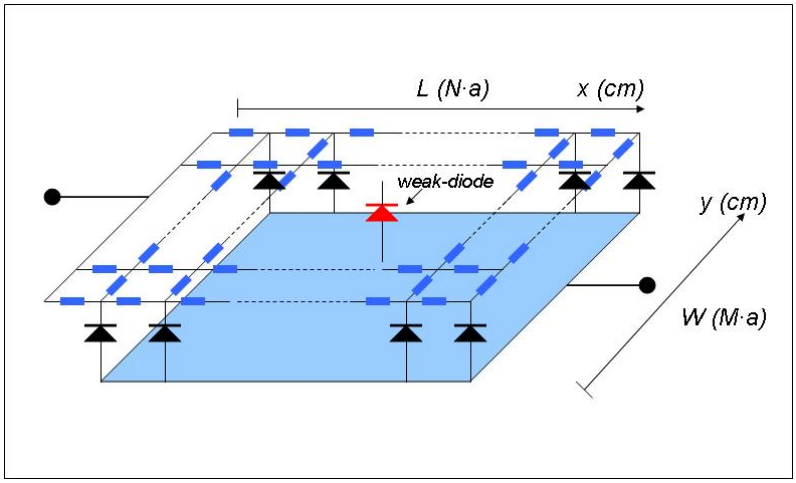

Fig.3.18. Circuit diagram of the subcell with a weak microdiode in the center.

The weak microdiode (colored in red) is modeled by a diode with the open circuit voltage lower than the rest good behaving microdiodes. **Figure 3.19** shows examples of subcell *J-V*s with weak microdiodes in the center that have different open-circuit voltages $V_{OC\text{-}W}$ = 0.2, 0.26 and 0.4 V, while the baseline microdiode has V_{OC} = 0.8 V. Open circles represent maximum power points.

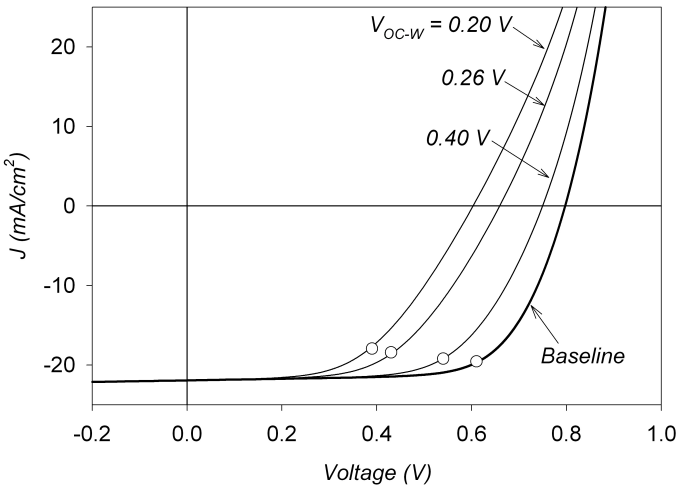

Fig.3.19. Examples of subcell *J-V*s with different weak microdiodes in the center.

As opposed to a subcell with a shunt, the short circuit current of a subcell with a weak microdiode stays essentially unchanged. **Table 3.3** shows basic solar cell parameters of subcell *J-V* curves shown in **figure 3.19.**

Table 3.3.
Basic solar cell parameters

	η	*FF*	V_{OC}	J_{SC}	V_{MP}	J_{MP}	*G*
V_{OC-W}	(%)	(%)	(V)	(mA/cm^2)	V	(mA/cm^2)	(mS/cm^2)
0.40 V	10.4	63.1	0.75	21.9	0.54	19.2	1
0.26 V	8.0	55.4	0.66	21.9	0.43	18.4	1
0.20 V	6.9	52.2	0.60	21.9	0.39	17.9	1

Table 3.3 shows that the lower voltage of the weak diode can cause significant change in the performance of the whole subcell. For comparison purposes the V_{OC-W} of one of the subcells is chosen to be 0.26 V so that the efficiency (8%) of that subcell is the same as the efficiency of the subcell with a shunt in the center that has G = 11.8 mS.

3.3.2 Weak diode location analysis

In the examples given above, the subcells have weak microdiodes in the center, but this may not be the case. In section 3.2.3 it was explained why variation in the location of the shunt along *Y*-axis of the subcell does not matter, and the same applies for weak diodes. Thus, only variation in *X*-axis will be considered, though the probability of a weak diode being at a specific spatial location may vary depending on the physical mechanism that causes local voltage reduction. **Figure 3.20** shows subcell *J*-*V* curves with weak microdiodes ($V_{OC\text{-}W}$ = 0.26 V) at different spatial locations – close to the gridline, in the center and opposite the gridline.

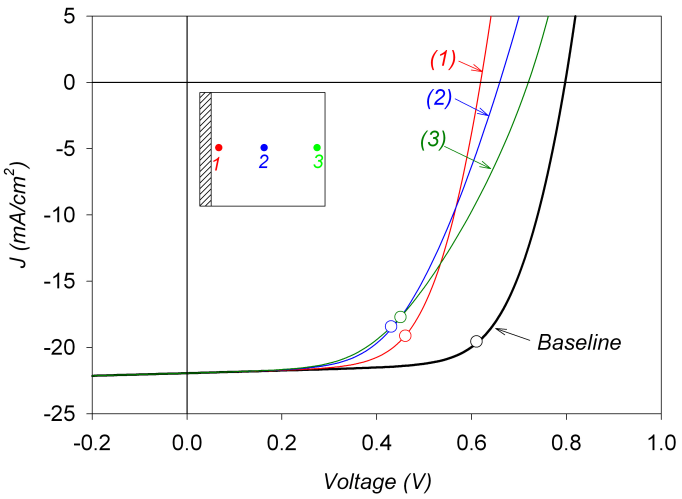

Fig.3.20 Subcell *J*-*V* curves with weak microdiodes ($V_{OC\text{-}W}$ = 0.26 V) at different spatial locations.

Table 3.4 shows basic solar cell parameters of four subcell *J*-*V* curves shown in **figure 3.20**. The location of the weak microdiode in the subcell has a significant impact on the current-voltage curve of the subcell, but less so on the maximum power.

Table 3.4.
Basic solar cell parameters

	V_{OC} (V)	J_{SC} (mA/cm^2)	FF (%)	η (%)
Baseline	0.80	22.0	68.7	12.0
(1) Close to the gridline	0.62	21.9	64.8	8.8
(2) In the center	0.66	21.9	55.4	8.0
(3) Opposite the gridline	0.72	21.9	50.5	8.0

The best case is when the weak microdiode located right next to the gridline.

3.3.3 Microdiode voltage profile and weak microdiode operation conditions

Similar to the presentation of shunt effects, **figure 3.21** profile a 3-D surface of microdiode operating voltages in a subcell with a weak microdiode ($V_{OC\text{-}W}$ = 0.26 V) in the center with the subcell biased at its weak-subcell V_{MP} = 0.43 V. The solid line in **figure 3.21** is shown for reference and is the profile of microdiode operating voltages of the uniform subcell which is biased at the uniform-subcell V_{MP} = 0.61 V.

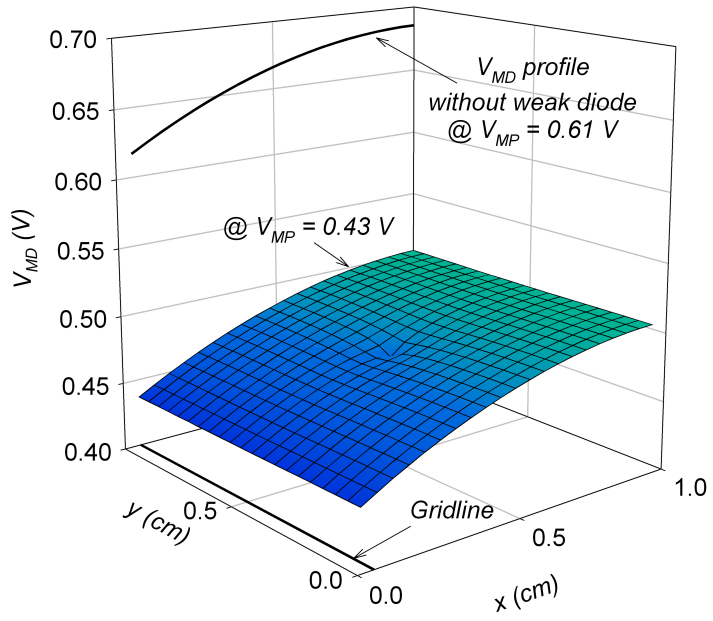

Fig.3.21 3-D profile of microdiode operating voltages in a subcell with a weak microdiode ($V_{OC\text{-}W}$ = 0.26 V) in the center.

Most of the difference between the reference line and the 3-D surface is because subcell operating voltage values (V_{MP}) are different. The small dip in the surface corresponds to the location of the weak microdiode in the subcell. The weak microdiode is biased at $V_{MD\text{-}W}$ = 0.47 V, while the $V_{OC\text{-}W}$ = 0.26 V, which means that the forward current of the weak microdiode at 0.47 V is very high.

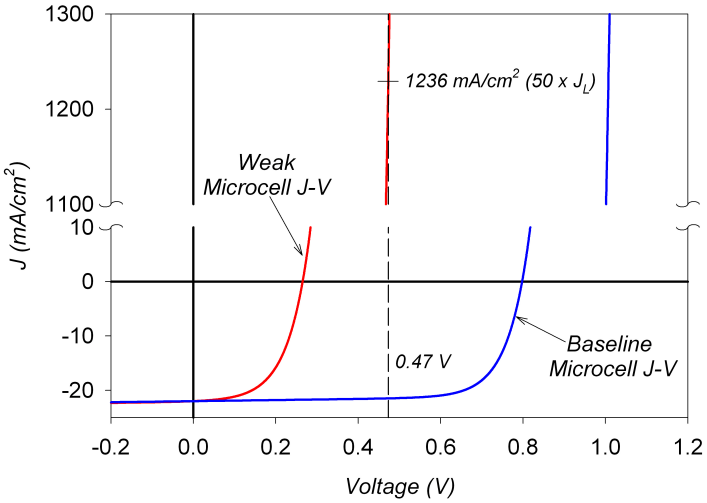

Fig.3.22 Weak ($V_{OC\text{-}W}$ = 0.26 V) and baseline microcell *J-V* curves.

Figure 3.22 illustrates weak ($V_{OC\text{-}W}$ = 0.26 V) and baseline microcell *J-V* curves on a large current density scale, the dashed line shows the operating voltage (0.47 V) of the weak microdiode in the subcell; at that voltage weak-microdiode has current density of above 1000 mA/cm^2 which is equivalent to 50×J_L. Thus, since this weak microdiode operates in the first power quadrant it functions not as a power generator but instead as a power consumer. A more detailed analysis of its power losses is considered in the next section.

3.3.4 Power losses in the subcell

Figure 3.23 shows 3-D power loss surfaces P_{MD} and P_{TCO} for a subcell with a weak microdiode ($V_{OC\text{-}W}$ = 0.26 V) in the center and when the subcell is biased at the weak-subcell V_{MP} = 0.43 V.

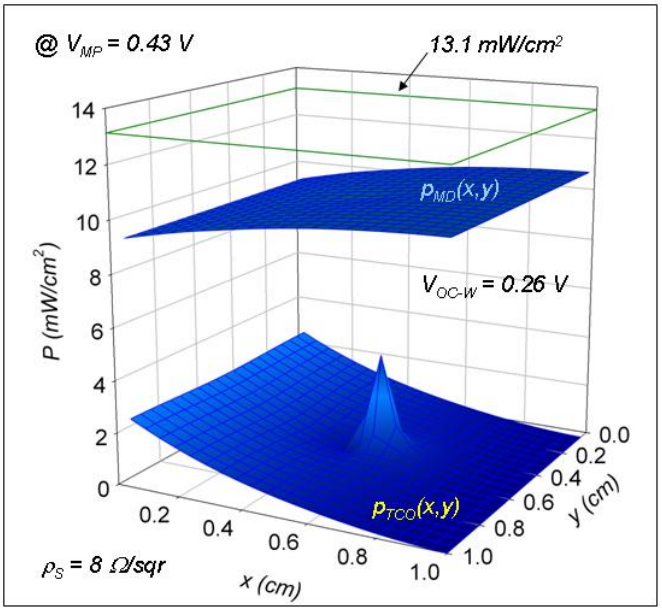

Fig.3.23. 3-D power loss surfaces P_{MD} and P_{TCO} for a subcell with a weak microdiode in the center.

For the upper surface P_{MD} the reference level is the maximum power density of the microcell 13.1 mW/cm^2. The spike in the lower surface P_{TCO} representing the power dissipation density in TCO is not as high as it was in the case of shunt in **figure 3.10-b**, even though both subcells have same efficiency (8%). The upper surface P_{MD} has dropped much lower than in the case of shunt. **Figure 3.23** shows a smooth P_{MD} surface, however, it does not reflect power lost in the weak diode itself. This loss, however, is included in **Figure 3.24.**

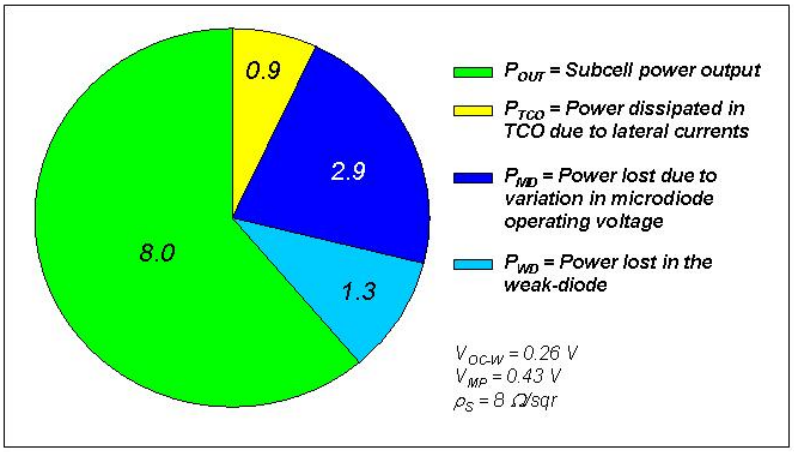

Fig.3.24. Integrated power losses in the subcell with the weak microdiode in the center.

Figure 3.24 shows a pie chart with integrated power losses for a subcell with the weak diode in its center. The power lost due to variation in microdiode operating voltages P_{MD} accounts for most of the power loss, while in the case of shunts it was a minor secondary loss mechanism. Power lost in the weak diode P_{WD} is very sensitive to the difference $\Delta V = V_{WD}$-$V_{OC\text{-}W}$, and has exponential dependence. Taking $R_S = 0$ from equation (3.1) for the weak microdiode:

$$j_{WD} = j_0 e^{\beta V_{WD}} + G V_{WD} - j_L. \tag{3.18}$$

For the high forward bias conditions the last two terms are negligible (G = 1mScm^{-2}) and thus the power lost in the weak microdiode is:

$$P_{WD} = j_{WD} \cdot V_{WD} = j_0 V_{WD} e^{\beta V_{WD}}. \tag{3.19}$$

From (3.18),

$$j_0 = j_L e^{-\beta V_{OC-W}}. \tag{3.20}$$

Substituting (3.20) into (3.19),

$$R_{WD} = j_L V_{WD} e^{\beta \Delta V}. \tag{3.21}$$

Thus, j_L = 22mA/cm^2, V_{WD} = 0.47 V and $V_{OC\text{-}W}$ = 0.26 V yield power density $P_{WD} \approx$ 600 mW/cm^2 and power ≈ 1.38 mW (since the area of a microdiode is $a^2 = 2.3 \cdot 10^{-3}$ cm^2), which is close to what is shown in **figure 3.24** (1.3 mW).

3.3.5. TCO sheet resistance variation

Figure 3.25 shows integrated power losses P_{MD}, P_{WD}, P_{TCO} and P_{TOTAL} in the subcell with a weak microdiode ($V_{OC\text{-}W}$ = 0.26 V) in its center as a function of subcell TCO sheet resistance. The subcell is biased at weak-subcell V_{MP}, which depends on specific value of ρ_S.

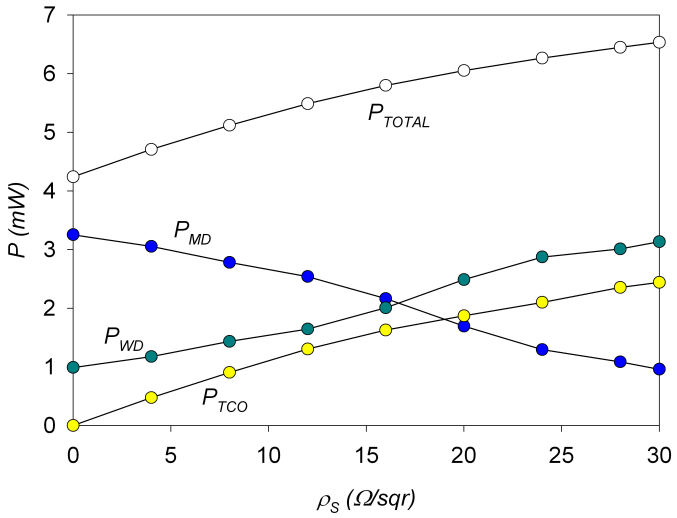

Fig.3.25 Integrated power losses as a function of ρ_S.

Figure 3.25 shows that all three contributors P_{MD}, P_{WD} and P_{TCO} are comparable for typical values of ρ_S (8-16 Ω/sqr).

Thus, a systematic study of the effect of a shunt and a weak-diode on a subcell is performed. It was shown that the 2-D circuit model of a subcell, presented in the previous chapter, is indeed capable of analyzing the impact of non-uniformities from different aspects. Most of the useful results extracted from simulations are summarized in the last chapter.

Chapter 4
Effect of multiple shunts and weak-diodes on thin-film modules

In the previous chapter 3 it was shown that a localized micro-shunt or weak micro-diode can have a severe destructive impact on a lab-scale solar cell (subcell). However, even a severe micro-shunt or micro-diode will have very little effect on the performance of the entire module. The primary goals of the present chapter are to understand the collective impact of multiple shunts or weak diodes on module performance, what the appropriate non-uniformity parameters are, and how these parameters correlate with each other in their effect on the module.

4.1. Non-uniformity distribution parameter

To evaluate the effect of multiple, but similar non-uniformities (i.e. shunts or weak diodes) on a module, it is useful to define a parameter that characterizes the distribution of several identical non-uniformities over the module area. The distribution pattern of identical non-uniformities over the module will be characterized here by the parameter P, which is defined as $P = a/b$, where "b" is the fraction of cells in a module

that have non-uniformity(s), and "*a*" is the fraction of identical subcells that have non-uniformity in each of the non-uniform cells.

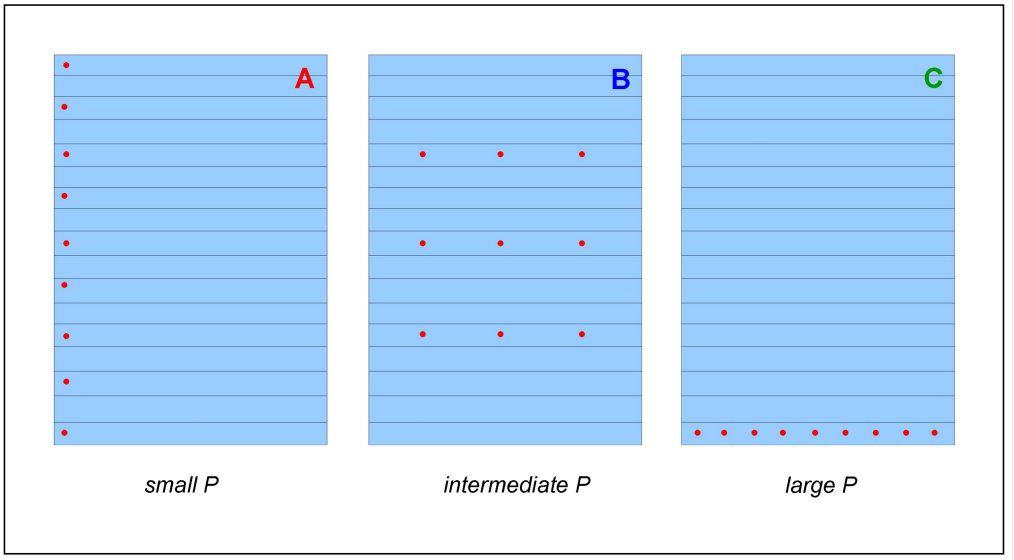

Fig.4.1. Illustration of distribution parameter *P*.

Figure 4.1 illustrates how non-uniformities are distributed depending on the value of *P*. Small values of *P* correspond to a pattern where many cells in the module have a small number of non-uniformities in each of them. Large values of *P* simulate a pattern where a small number of cells contain a large number of non-uniformities each. An intermediate value of *P* simulates a pattern when a moderate number of cells have moderate number of non-uniformities; that is non-uniformities are spread relatively evenly over the whole module area. This approach can be generalized so that the non-uniform cells need not be identical, and the results are qualitatively the same. There can be other definitions of a distribution parameter; however, the one introduced here seems to be the most practical, because it is easy to work with and can be related to real-life situations. For example,

1. situation *A* in **figure 4.1** exists physically if the edge of the entire module is not properly treated during the manufacturing process causing shunts or weak-diodes.
2. situation *B* can be reproduced when the layer deposition process has occasional imperfections.
3. situation *C* can be reproduced if the end of the module is not properly processed, or if scribing between two cells is misaligned.

4.2. Simulation setup

Figure 4.2 again shows the general simulation schematic of the circuit model used to analyze the impact of non-uniformities on modules. The setup is discussed in details in Chapter 2. Although the location of the non-uniformity in the subcell is not critical, for consistency purposes it is located at the central microcell.

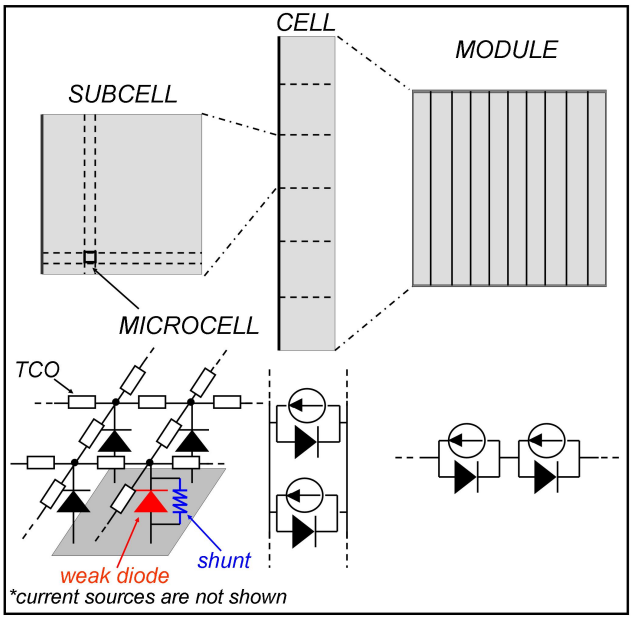

Fig.4.2. Circuit model setup.

A reliable parameterization of severity of non-uniformity and its fractional area is introduced in each of the following sections. Absolute module-efficiency loss $\Delta\eta$ (%) is used as the main output parameter for the analysis of both shunts and weak diodes in their impact on the module.

4.3. Effect of multiple shunts on thin-film modules

The number of shunts over the module area is parameterized by the relative shunted area A_S (%), and the severity of a shunt is parameterized by the efficiency η_S (%) of the shunted subcell. **Figure 4.3** shows subcell *J*-*V* curves based on typical CdTe parameters with different efficiencies η_S = 0.5, 1, 2, 4, 8 and 12%, where the 12% curve represents a subcell without a shunt. Unless otherwise stated, TCO sheet resistance is ρ_S = 8 Ω/sqr.

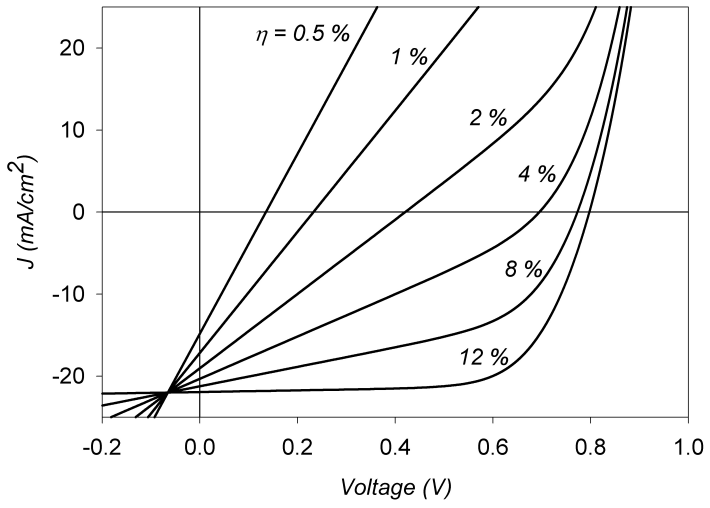

Fig.4.3. Subcell *J*-*V* curves for shunts of different magnitude.

Figure 4.4 shows dependence of absolute module-efficiency loss $\Delta\eta$ on the distribution pattern of identical shunts over the module.

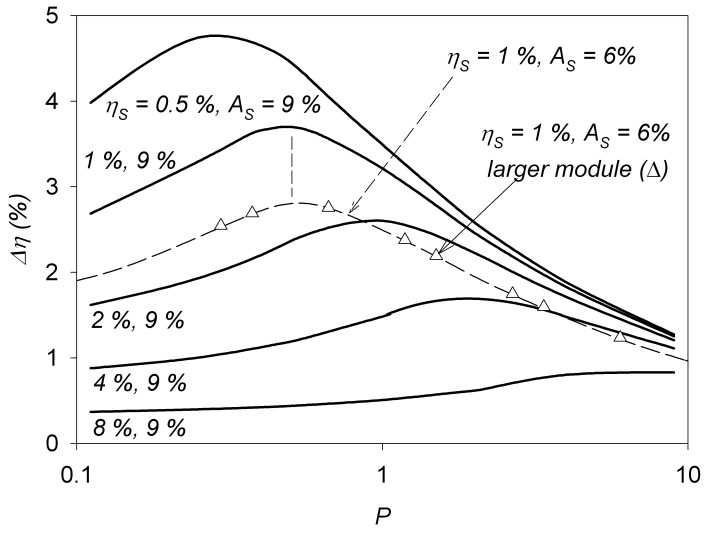

Fig.4.4. $\Delta\eta$ vs. shunt-distribution parameter P. Solid lines for A_S = 9%, dashed for A_S = 6%.

Figure 4.4 shows that the absolute module-efficiency loss $\Delta\eta$ varies significantly with distribution pattern of shunts over the module (P). Solid lines in the **figure 4.4** correspond to the module with A_S = 9% and different values of η_S (0.5, 1, 2, 4 and 8%). The dashed line corresponds to the same module with A_S = 6% and η_S = 1%, and triangle icons, which fall on that line, correspond to a larger module that has 120 cells, each 1 by 60 cm in size with the same shunt area fraction and severity. The coincidence of the curves for different size modules confirms that P is a reliable distribution parameter.

One common feature to all of the curves in **figure 4.4** is a maximum absolute-efficiency reduction at an intermediate value of P. Thus, the worst-case scenario occurs when shunted subcells are evenly distributed over the entire module. The fact that $\Delta\eta$ monotonically decreases as P gets larger suggests that the smallest efficiency decrease

occurs when all shunted subcells are clustered in a small number of cells. **Figure 4.4** also implies that with all other parameters the same, the maximum reduction shifts towards larger values of P when η_S is less severe. Also shown in the **figure 4.4**, when A_S is smaller, the maximum reduction is less, but it occurs at nearly the same value of P.

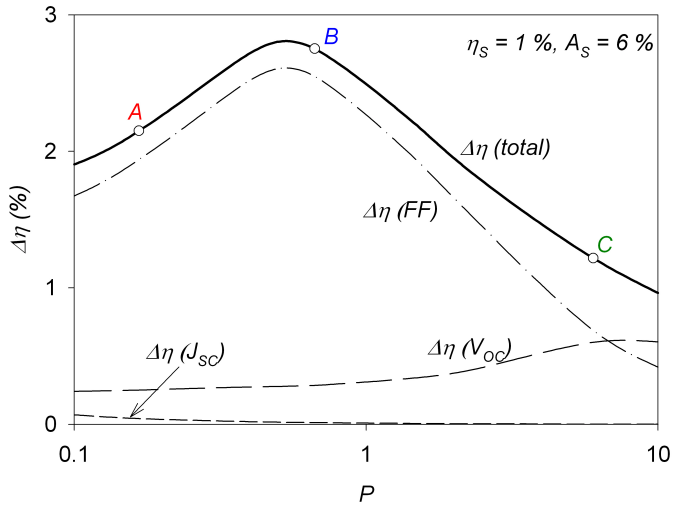

Fig.4.5. Contributions to $\Delta\eta$ caused by different J-V parameters.

Figure 4.5 illustrates the individual contributions of FF, V_{OC} and J_{SC} to the total module-efficiency loss $\Delta\eta$ *(total)*. The variables shown in the figure are defined as:

$$\Delta\eta(FF) = \eta_0 \frac{\Delta FF}{FF}, \quad \Delta\eta(V_{OC}) = \eta_0 \frac{\Delta V_{OC}}{V_{OC}}, \quad \Delta\eta(J_{SC}) = \eta_0 \frac{\Delta J_{SC}}{J_{SC}}. \tag{4.1}$$

Second and third order contributions are negligible and are not shown in the **figure 4.5**. **Figure 4.5** suggests that in the worst-case scenario, at intermediate values of P, $\Delta\eta$ is primarily due to the FF loss and to a smaller extent to the V_{OC} loss, while for the large values of P, the FF and V_{OC} losses are comparable. The J_{SC} loss has a nearly negligible impact in all cases. **Figure 4.6** illustrates module J-V curves corresponding to points A, B

and *C*, from **figure 4.5**. The black line in the **figure 4.6** is the baseline *J-V* with no shunts. Circles highlight the maximum power points. Curves *B, C* and *A* represent typical module *J-V* curves with the largest, smallest, and intermediate impact of shunt distribution respectively. **Figure 4.6** reaffirms that in the worst-case scenario (B), *FF* suffers the most, while in the best-case scenario (C), V_{OC} suffers the most, which is consistent with the **figure 4.5**.

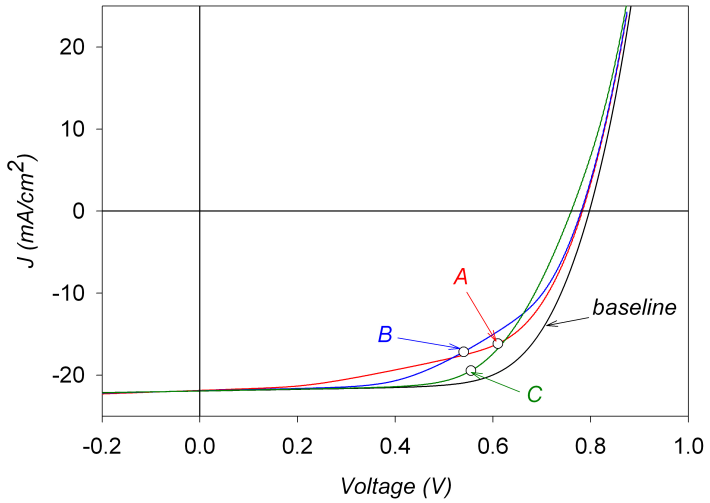

Fig.4.6. Module *J-V* curves with small, intermediate, and large values of *P*.

Figure 4.7 shows the absolute module-efficiency loss $\Delta\eta$ in the worst-case scenario (point B) as a function of relative shunted area A_S for different values of shunted subcell efficiency η_S. **Figure 4.7** suggests that even though $\Delta\eta$ depends on both η_S and A_S, it depends more strongly on η_S compared to A_S. **Figure 4.7** also shows that estimates of $\Delta\eta$ based on simple area-weighted efficiencies yield a significant error. For example, for A_S = 6% and η_S = 1%, the area-weighted efficiency loss is $\Delta\eta$ = 0.7% compared to the 2.8% impact of shunted subcells. Similarly, when η_S = 8%, the area-weighted efficiency loss would be 3 times less, 0.2% compared to 0.6%.

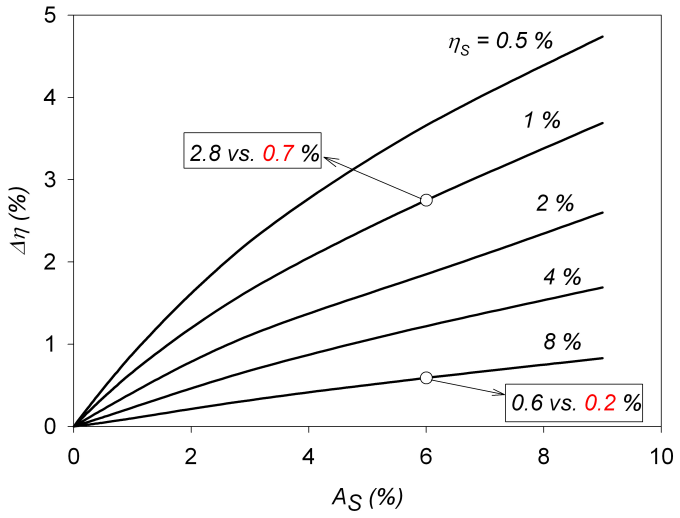

Fig.4.7. $\Delta\eta$ in the worst-case scenario (point B) vs. A_S for different η_S.

Figure 4.8 shows module-efficiency η_S in the worst-case scenario as a function of relative shunted area A_S with η_S = 1% for two different TCO sheet resistances: 8 and 16 Ω/sqr. The non-shunted module-efficiencies are η_0 = 12% and 11% respectively. Since the TCO sheet resistance tends to isolate the shunt from the rest of the area, a higher sheet resistance diminishes the impact of shunts on module-efficiency (smaller slope).

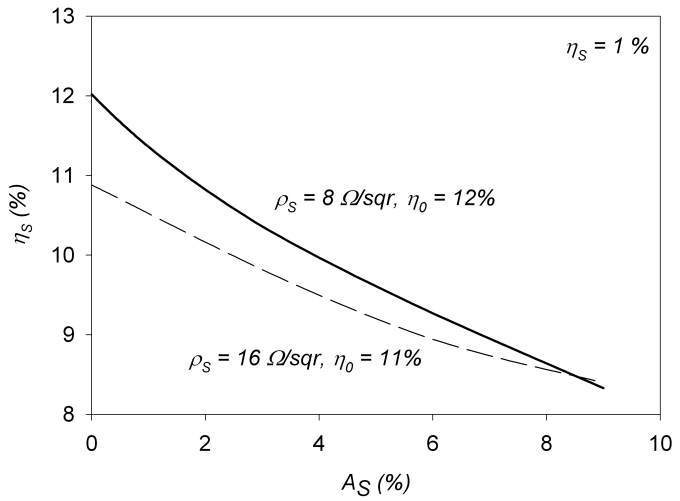

Fig.4.8. Module-efficiency η_S in the worst-case scenario for two sheet resistances.

Because of the power dissipation from lateral currents in the TCO layer, however, higher TCO sheet resistance also yields smaller η_0. Eventually though the two curves intersect, and for sufficiently large area shunting, higher sheet resistance could be advantageous.

4.4. Effect of multiple weak-diodes on thin-film modules

The number of weak-subcells over the module area is parameterized by the relative weak area A_W (%), and the weakness level of a subcell is parameterized by its open-circuit voltage $V_{OC\text{-}W}$.

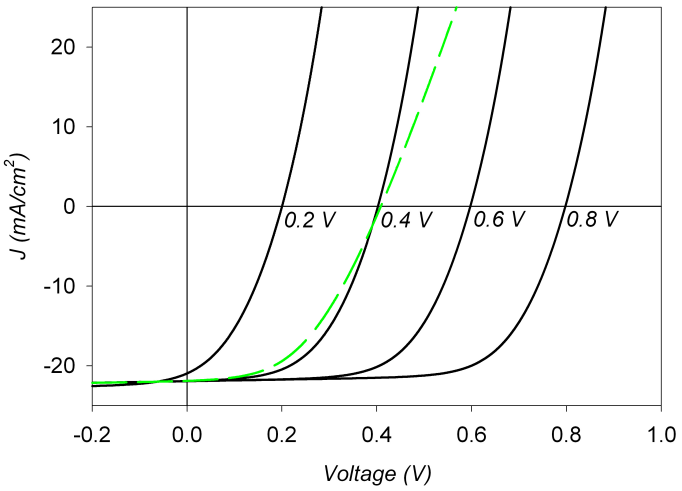

Fig.4.9. Subcell *J-V* curves with different values of V_{OC}.

Figure 4.9 shows subcell *J-V* curves with different values of the open-circuit voltage V_{OC} = 0.2, 0.4, 0.6 and 0.8 V. The *J-V* curve with V_{OC} = 0.8 V represents the baseline subcell *J-V* with 12% efficiency. The solid curves represent uniform subcells with all microcells being identical and having specified open-circuit voltages (0.2, 0.4, 0.6 and 0.8 V). The

dashed curve, however, corresponds to a non-uniform subcell that has a small very weak area in the center of the subcell and the rest of the subcell area with V_{OC} = 0.8 V. The motivation to use uniform-weak subcells is that their *J-V* curves differ from each other in a systematic fashion, which makes comparison of their impact on the module performance easier. However, analysis of the impact of non-uniform subcell on the module performance allows one to see the effect of the TCO sheet resistance.

Figure 4.10 shows that the absolute module-efficiency loss $\Delta\eta$ is a strong function of distribution pattern of weak-subcells over the module (*P*).

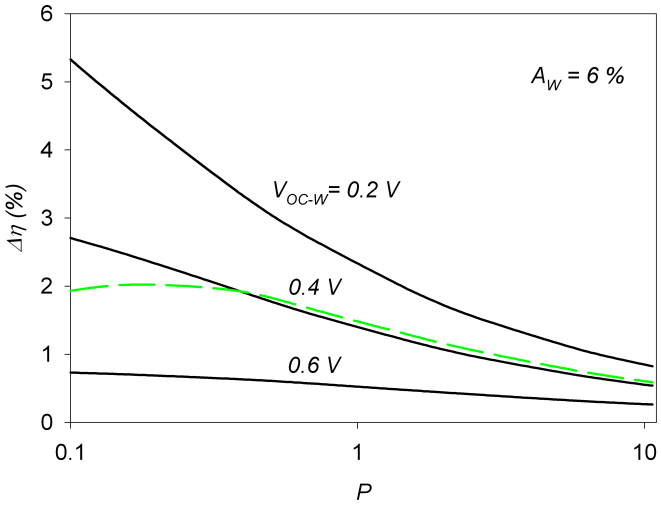

Fig.4.10. $\Delta\eta$ vs. weak-diode-distribution parameter *P*.

Black solid curves in the **figure 4.10** correspond to the module with *6%* of its area covered by uniform weak-subcells with values of $V_{OC\text{-}W}$ = 0.2, 0.4 and 0.6 V. The dashed curve corresponds to $V_{OC\text{-}W}$ = 0.4 V, but with non-uniform weak subcells.

Figure 4.10 suggests that if uniform subcells are assumed, $\Delta\eta$ decreases monotonically as *P* gets larger. Thus the largest decrease in performance occurs when *P*

is small, and the smallest when P is large. **Figure 4.10** also shows that the dashed curve differs only slightly from the corresponding black curve over a wide range of P.

Figure 4.11 illustrates the contributions of V_{OC} and FF to the total module-efficiency loss $\Delta\eta$ *(total)* when uniform weak-subcells are used. The variables shown in the figure are defined as follows:

$$\Delta\eta(V_{OC}) = \eta_0 \frac{\Delta V_{OC}}{V_{OC}} k,\ \Delta\eta(FF) = \eta_0 \frac{\Delta FF}{FF} k, \tag{4.2}$$

where k is a correction factor that accounts for non-negligible second order terms due to both V_{OC} and FF defined as follows:

$$k = \left(1 - \frac{\Delta V_{OC}\Delta FF}{FF\Delta V_{OC} + V_{OC}\Delta FF}\right). \tag{4.3}$$

Figure 4.11 suggests that both $\Delta\eta(V_{OC})$ and $\Delta\eta(FF)$ are comparable over the whole range of P. Contributions from J_{SC} and other second and third order terms are negligible.

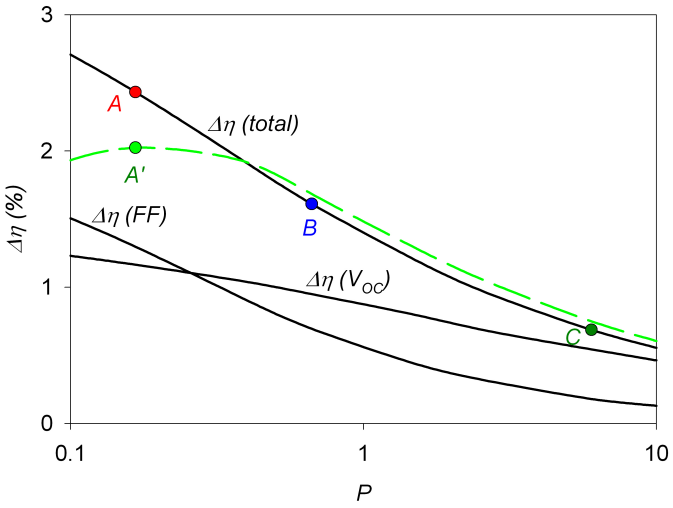

Fig.4.11 Contributions to $\Delta\eta$ caused by different J-V parameters.

Figure 4.12 shows module *J-V* curves corresponding to points *A*, *B*, *C* and *A'* from **figure 4.11**. The black line in **figure 4.12** is the baseline *J-V* curve. Solid circles highlight the maximum power points. Current voltage curves *A*, *B* and *C* progress in a systematic fashion, and both *FF* and V_{OC} decrease similarly as is expected from **figure 4.11**. The dashed "*A*" curve in **figure 4.12**, however, does not follow the systematic progression due to the non-uniform nature of weak-subcells used. **Figure 4.12** also shows that there is essentially no loss in J_{SC}.

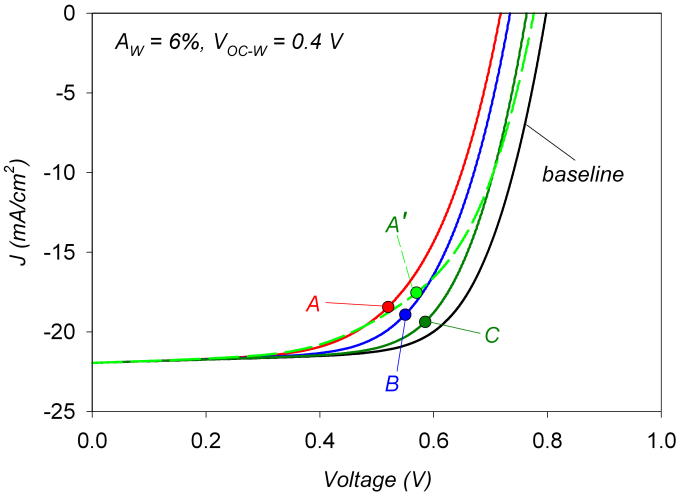

Fig.4.12. Module *J-V* curves for three values of weak-diode distribution parameter *P*.

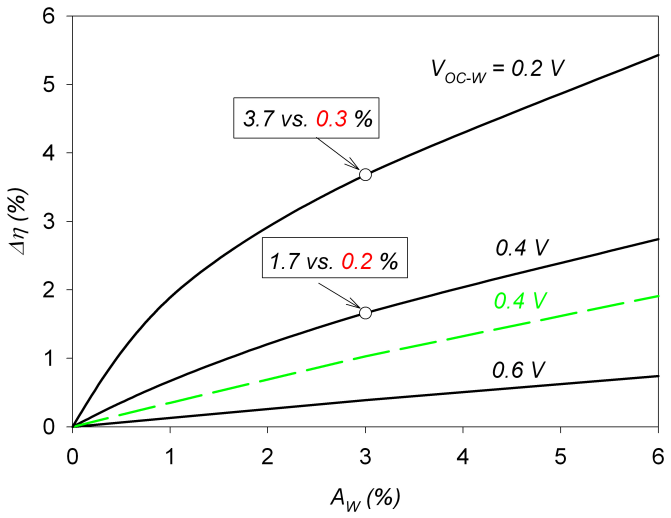

Fig.4.13. $\Delta\eta$ in the worst-case scenario vs. A_S for different $V_{OC\text{-}W}$.

Figure 4.13 shows the absolute module-efficiency loss $\Delta\eta$ in the worst-case scenario (point A) as a function of relative weak area A_W for different values of $V_{OC\text{-}W}$. Estimates of $\Delta\eta$ based on simple area-weighted efficiencies yield an even greater error than for shunts. For example, for A_W = 3% and $V_{OC\text{-}W}$ = 0.4 V, the area-weighted efficiency loss is $\Delta\eta$ = 0.2% compared to the actual 1.7% impact of uniform weak-subcells. Similarly, when $V_{OC\text{-}W}$ = 0.2 V, the area-weighted efficiency loss is 0.3% compared to 3.7%, again for uniform weak-subcells.

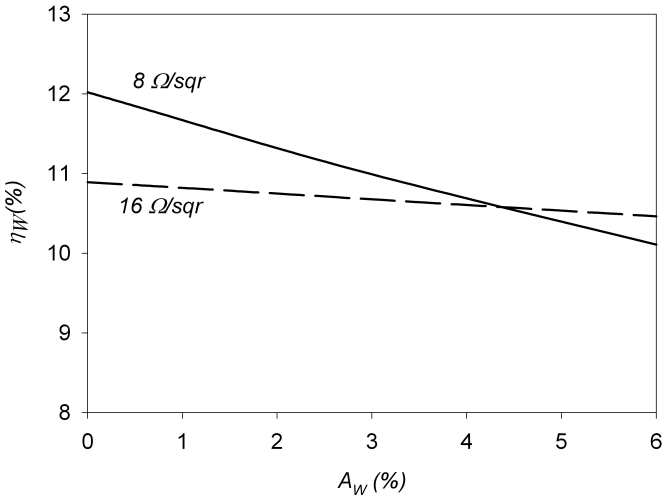

Fig.4.14. Module-efficiency η_W in the worst-case scenario for two sheet resistances.

Figure 4.14 shows module-efficiency η_W at point A as a function of relative weak area A_W with $V_{OC\text{-}W}$ = 0.4 V for two different TCO sheet resistances: 8 and 16 Ω/sqr. Non-uniform subcells are used as weak ones here. Baseline module-efficiencies are η_0 = 12% for the smaller resistance TCO and 11% for the larger sheet resistance. The dashed line has a smaller slope, because a higher sheet resistance diminishes the impact of weak-diodes on module-efficiency. Here also, higher TCO sheet resistance yields smaller η_0, and the two curves shown intersect.

Thus, the effect of multiple identical shunts and weak-diodes on the module performance was analyzed with the help of three step (subcell-cell-module) simulation framework. Introduced here parameters such as absolute module efficiency $\Delta\eta$, non-uniformity distribution parameter P, non-uniformity fractional area $A_{S,W}$, and non-

uniformity severity measure η_S or $V_{OC\text{-}W}$ proved to be helpful to analyze the losses in a systematic way. The summary of obtained results is given in the last chapter.

Chapter 5
Electroluminescence and 2-D simulations

Standard characterization techniques such as current-voltage, quantum efficiency and capacitance measurements provide information about solar cells that is spatially averaged over the cell area. However, most polycrystalline thin-film solar cells are inherently non-uniform and spatially resolved characterization techniques are required to unravel the effect of different microscopic non-uniformities in different layers on the overall performance of solar cells. There are currently several spatially resolved techniques that are being used in PV research laboratories: Light Beam Induced Current (LBIC), Electron Beam Induced Current (EBIC), Photoluminescence (PL) and Electroluminescence (EL) etc. Electroluminescence is one of the spatially resolved characterization techniques, which in recent years has gained increasing popularity in the thin-film PV community. In the current chapter, we will consider how 2-D numerical simulations and analytical calculations can be helpful to understand experimental EL data and what helpful recommendations can be provided. The focus will be on thin-film modules with multiple shunts and/or weak-diodes. The primary goals are to understand how the EL image of a uniform module depends on different controlling parameters, deduce how that image would change due to non-uniformities, develop recommendations

on how to experimentally detect and quantify these non-uniformities and give other qualitative experimental guidelines.

5.1. The general experimental setup

Performing an electroluminescence measurement is essentially operating a solar cell in reverse as a light emitting diode. The solar cell is held under forward bias and some of the injected minority carriers go through radiative recombination and emit photons, which are then collected with a sensitive CCD camera to obtain a spatially resolved image of the distribution of radiative recombination in the cell.

The experimental setup of the EL measurement is relatively simple and requires three primary pieces of equipment – CCD camera, power supply for the cell or module and some sort of temperature controller. The CCD camera is placed on a vertical translation stage right above the sample solar cell. The translation stage allows for different display windows, which makes measurements of different size cells possible. The objective of the CCD camera can also be equipped with additional optics to allow detailed close-up images (higher resolution). The CCD camera is also cooled to diminish thermal noise. The cell or module may also be placed on translation stages to allow movement in X and Y directions and is forward biased by the power supply. The whole system should be covered by a dark box to prevent penetration of ambient light.

Figure 5.1 illustrates a schematic of the experimental setup at the Nara Institute of Science and Technology (NAIST) in Japan.

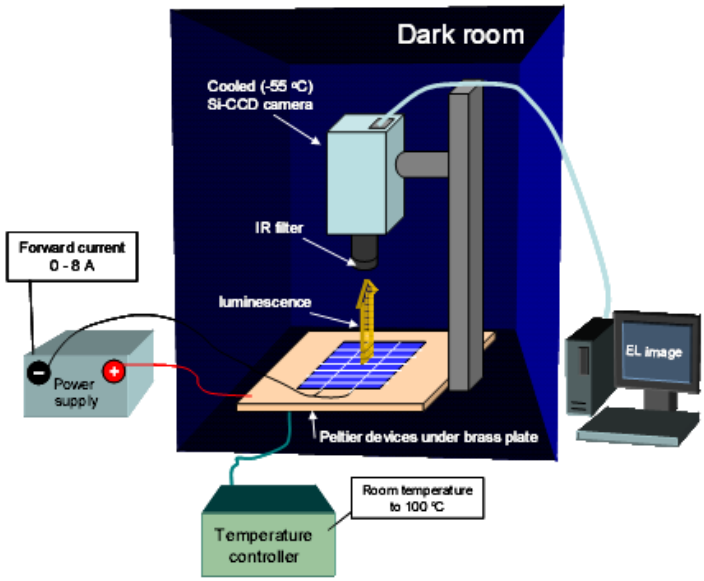

Fig.5.1. Schematic of the experimental setup at the Nara Institute of Science and Technology (NAIST), Japan.

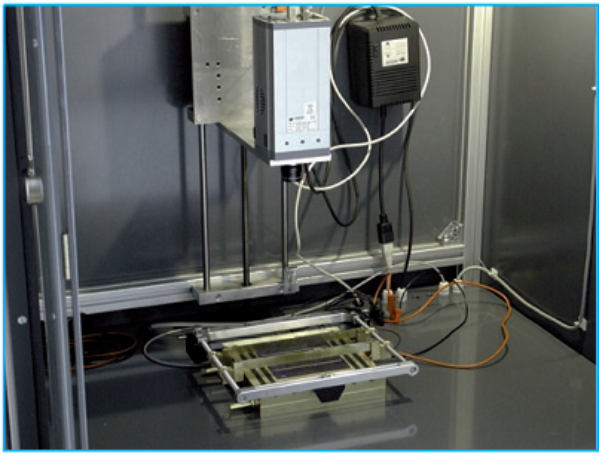

Fig.5.2. Electroluminescence measurement system at the University of Konstanz, Germany (photo by David Kiliani).

Figure 5.2 is a photograph of EL system at the University of Konstanz in Germany. The light emitted by the solar cell generally has very low intensity and that fact sets certain limits on the CCD camera. The camera must have a good sensitivity in the operating

wavelength and a small thermal noise. **Figure 5.3** illustrates typical commercially available CCD cameras.

Fig.5.3. Examples of typical CCD cameras.

Another important part of the EL setup is the cooling system for the solar cell, which allows temperature dependent EL measurements. Even though basic EL measurements can be performed under room temperature, some measurements, for example those to recognize the transition from domination of acceptor-donor recombination to that of band-to-band recombination, very low temperatures are required[12,13]. To identify that transition in Ref. [12] and [13], temperatures as low as 90K for Si and 120K for CIGS were required. The necessity of a high cooling system, of course, depends on the goal of the experiment; for-example in Ref. [12], temperature of only 243K was sufficient for the temperature dependent-measurements. However, in the current work we will not consider any temperature-dependent effects.

5.2. 2-D simulations

2-D simulations can be very helpful in the analysis of EL images and for providing useful recommendations for further experiments. In Chapter 3 it was shown that with 2-D simulations one can calculate the microdiode voltage distribution in the subcell. The voltage map can then be used to reconstruct a spatially resolved EL image, because the EL signal is related to the diode voltage through the so called reciprocity relation, which says that the intensity of the EL signal ϕ depends exponentially on the voltage V across the diode[14]:

$$\phi \propto e^{\frac{qV}{kT}}. \tag{5.1}$$

Figure 5.4 shows the calculated 3-D map of microdiode voltages over the shunted subcell in the dark under forward bias. The shunt is located at the center of the subcell.

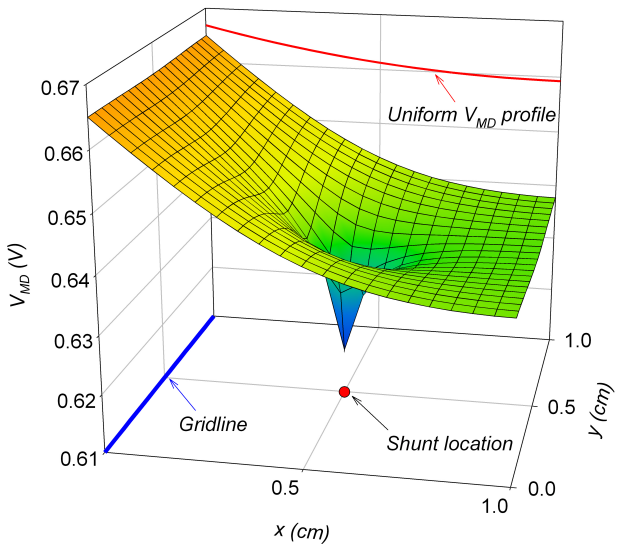

Fig.5.4. 3-D graph of microdiode voltages.

The applied voltage for **figure 5.4** is $V_{app.}$ = 0.69 V, which yields dark current J = 2.2 mA/cm^2. The position of the gridline is shown by blue solid line. The red solid curve illustrates the microdiode voltage profile for the uniform case at the same applied bias. The 3-D map of microdiode voltages with a weak-microdiode in the center instead of a shunt would look similar depending on the weak-microdiode severity, but as discussed later in this chapter, there are differences when the EL current is varied.

Figure 5.5 illustrates electroluminescence image of the shunted subcell that follows from the voltage map in **figure 5.4**, using the reciprocity relation (5.1).

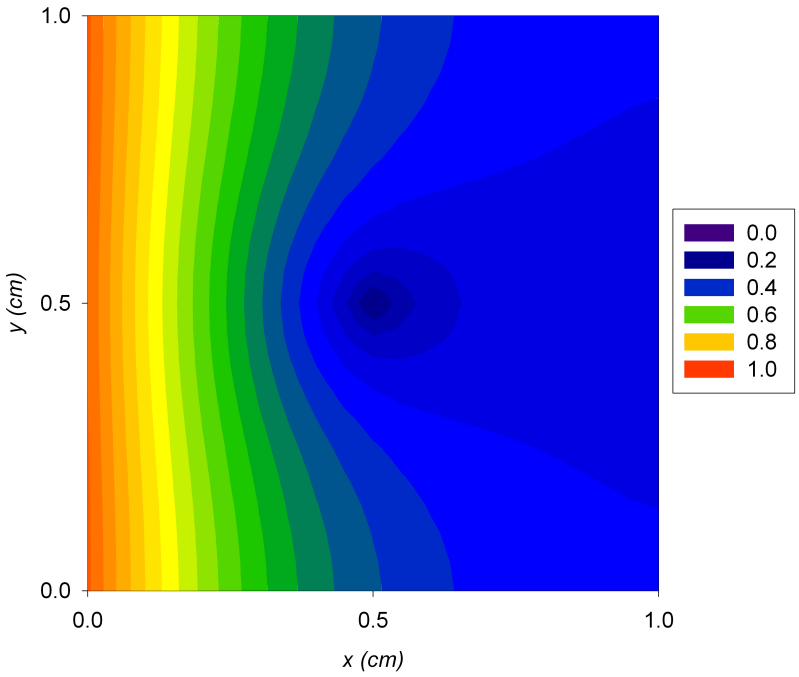

Fig.5.5. Simulated electroluminescence image of the shunted subcell.

The color bars represent the ratio - $\phi(x,y)/\phi_0(0,y)$, where $\phi(x,y)$ is the intensity of the EL signal and the subscript 0 represents the uniform EL signal. The normalization here is relative to x = 0 (at the gridline), where the EL signal intensity is the largest. This

ratio is one of the parameters that is introduced to analyze EL images and is called *cell-contrast (C-contrast).* C-contrast allows one to compare different parts of the same cell (shunted or not). It allows one to reconstruct the actual physical picture of the EL signal from the cell or module in arbitrary units (a.u.).

In addition to the C-contrast, another parameter referred to as *cell-to-cell-contrast* (*CC-contrast*) is introduced here to analyze EL data. The CC-contrast is defined as: $\phi(x,y)/\phi_0(x,y)$, rather than the C-contrast normalized to $x = 0$. CC-contrast allows one to compare EL signals at same coordinates between uniform and non-uniform cells. Obviously, for a uniform cell CC-contrast is unity everywhere.

5.3. Dependence of electroluminescence intensity on current

The current is the primary parameter that drives the EL measurement. Therefore, it is important to know how the EL intensity depends on the current.

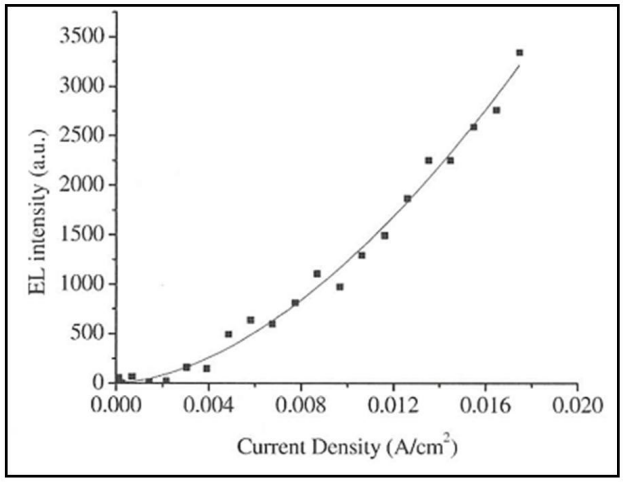

Fig.5.6. ϕ vs. J data for a typical CdTe/CdS device at room temperature (from Ref. [15])

Price et al[15] made EL measurements on a CdTe/CdS solar cell and showed that the EL intensity varies as a power-law function of current, $\phi \sim J^b$. An example from Ref. [15] is shown in **figure 5.6**. The solid line is a fit to $\phi = a \cdot J^b$, where $b \approx 1.7$. It was found that values of parameters a and b vary from sample to sample and that $1 \leq b \leq 2.5$.

Thus we know that[14] $\phi \sim \exp(qV/kT)$ and that[15] $\phi \sim J^b$, but we also know that the dark current $J \sim exp(qV/AkT)$, which suggests that the empirical exponent b should be the diode quality factor A. This is consistent with $1 \leq b \leq 2.5$, which is the typical range for diode quality factors of thin-film solar cells. Thus, we further assume that $\phi \sim J^A$. However, even if this assumption is not completely valid, it will have minimal impact on the results.

5.4. Analytic approach of EL image for the uniform subcell

It is helpful to have approximate analytic results for the simple uniform subcell.

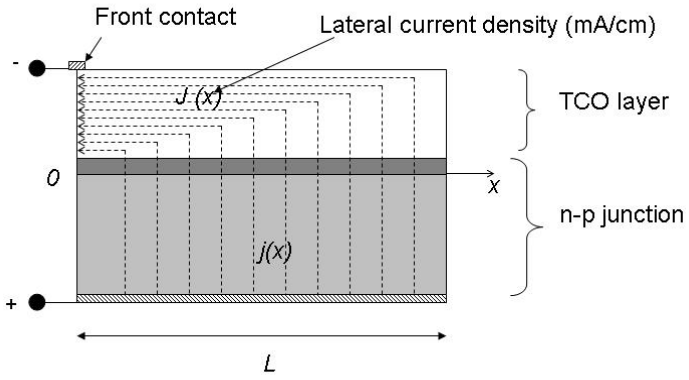

Fig.5.7. Schematic picture of lateral currents in TCO layer.

It turns out that with certain approximations one can derive functional dependence of the C-contrast on position *x*, current *I*, sheet resistance ρ_S and cell geometry (*L* and *W*). **Figure 5.7** shows schematic picture of lateral currents in TCO layer, where *J(x)* represents the lateral dark current density per unit of width (mA/cm), and *j(x)* is the longitudinal dark current density in (mA/cm^2).

If diode shunting is negligible, then the *j(x)* is given by simple diode equation:

$$j(x) = j_0 e^{\frac{qV(x)}{AkT}} = j_0 e^{\beta V(x)}, \tag{5.2}$$

where $\beta = q/AkT$. In the linear approximation the lateral current density (per unit width) is given as:

$$J(x) = j(x)(L - x) = j_0 e^{\beta V(x)}(L - x). \tag{5.3}$$

The total current per unit width in the circuit is $J(0) \equiv J_0$. The differential form of the Ohm's law is given by:

$$J(x) = -\frac{1}{\rho_S}\frac{dV(x)}{dx}. \tag{5.4}$$

From equations (5.3) and (5.4):

$$-\frac{1}{\rho_S}\frac{dV(x)}{dx} = j_0 e^{\beta V(x)}(L - x). \tag{5.5}$$

Rearranging the terms in (5.5):

$$e^{-\beta V(x)} dV(x) = -\rho_S j_0 (L - x) dx. \tag{5.6}$$

Integrating (5.6):

$$-\frac{1}{\beta} e^{-\beta V(x)} = \frac{\rho_S (L - x)^2}{2} j_0 + C, \tag{5.7}$$

where C is the integration constant. From (5.7) at $x = 0$:

$$C = -\frac{1}{\beta} e^{-\beta V(0)} - j_0 \frac{\rho_S L^2}{2}. \tag{5.8}$$

On the other hand, from (5.3) at $x = 0$:

$$J_0 = j_0 L e^{\beta V(0)}. \tag{5.9}$$

From (5.9):

$$-\frac{1}{\beta} e^{-\beta V(0)} = -\frac{1}{\beta} \frac{j_0 L}{J_0}. \tag{5.10}$$

Further substituting the first term in equation (5.8) by equation (5.10):

$$C = -\frac{1}{\beta} \frac{j_0 L}{J_0} - j_0 \frac{\rho_S L^2}{2}. \tag{5.11}$$

Substituting (5.11) into (5.7) and solving for the exponent:

$$e^{\beta V(x)} = \left[\frac{j_0 L}{J_0} + \beta j_0 \frac{\rho_S L^2}{2} - \beta j_0 \frac{\rho_S (L-x)^2}{2} \right]^{-1} =$$

$$= j_0{}^{-1} \left[\frac{L}{J_0} + \beta \frac{\rho_S L^2}{2} \left(1 - \left(1 - \frac{x}{L} \right)^2 \right) \right]^{-1}. \qquad (5.12)$$

From (5.12) at $x = 0$:

$$e^{\beta V(0)} = j_0{}^{-1} \left[\frac{L}{J_0} \right]^{-1}. \qquad (5.13)$$

The uniform EL signal is:

$$\phi_0(x) \propto e^{\frac{qV(x)}{kT}} = e^{\beta V(x) A}. \qquad (5.14)$$

From (5.14):

$$\frac{\phi_0(x)}{\phi_0(0)} = \left[\frac{e^{\beta V(x)}}{e^{\beta V(0)}} \right]^A. \qquad (5.15)$$

Substituting (5.12) and (5.13) into (5.15):

$$\frac{\phi_0(x)}{\phi_0(0)} = \left\{ 1 + \frac{J_0 \beta \rho_S L}{2} \left[1 - \left(1 - \frac{x}{L} \right)^2 \right] \right\}^{-A}. \qquad (5.16)$$

Since the total lateral current density per unit length is $J_0 = I/W$, the C-contrast of the EL signal will be:

$$\frac{\phi_0(x)}{\phi_0(0)} = \left\{1 + \frac{I\beta\rho_S}{2}\left(\frac{L}{W}\right)\left[1 - \left(1 - \frac{x}{L}\right)^2\right]\right\}^{-A} . \qquad (5.17)$$

Figure 5.8 shows the C-contrast given by equation (5.16) as a function of position. Solid lines and open circles in **figure 5.8** represent analytic results given by equation (5.16) and simulation results obtained by PSpice respectively.

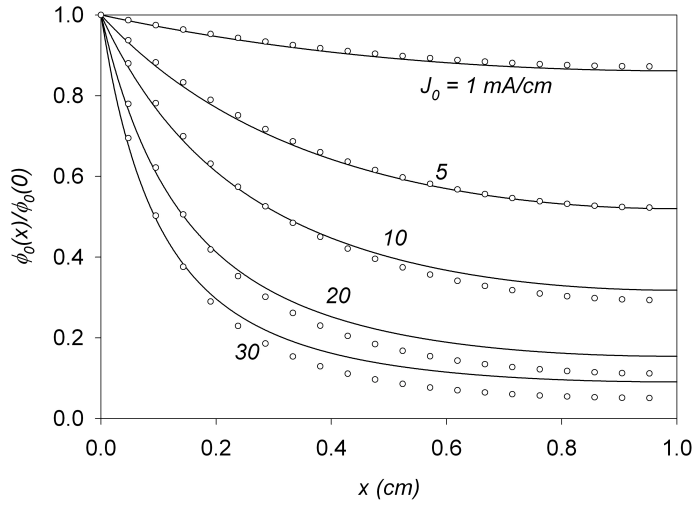

Fig.5.8. The C-contrast as a function of position (analytic vs. simulation results)

Equation (5.16) was obtained with two primary simplifying assumptions in mind: 1.) the lateral current density per unit length given by equation (5.3) assumes a linear approximation and 2.) the longitudinal current density given by equation (5.2) has no conductance term. These approximations lead to small discrepancies between analytic and simulation results, especially for large values of J_0.

Equation (5.17) is a helpful tool in the analysis of EL images of uniform cells. It can be used to estimate the sheet resistance from the EL image. It can predict how the C-contrast, or equivalently the EL image, would change with current.

5.5. Simulation example

Figure 5.9 shows an example of simulated EL image of three cells in a module, one of which is shunted. The color bar on the right represents the scale of the C-contrast.

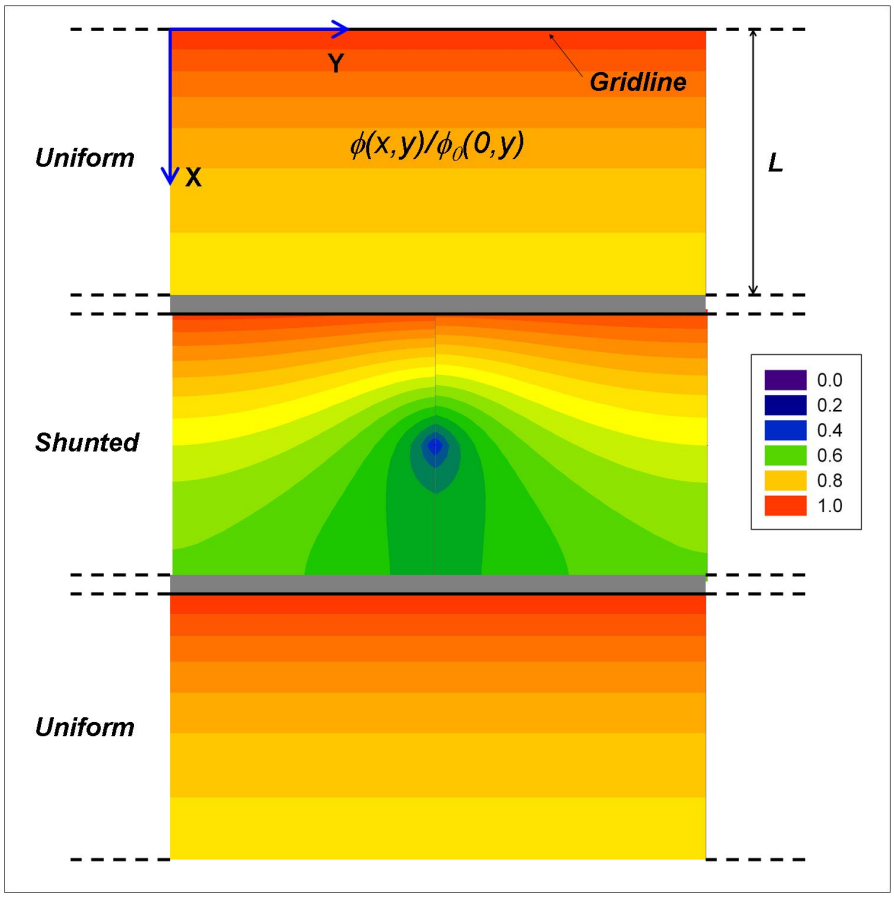

Fig.5.9. EL image of three cells in a module.

Both uniform and shunted cells have a gradient of C-contrast from the gridline to the edge of the cell, though the gradient in the shunted cell is distorted. The C-contrast is unity at the gridline of the uniform cell in accordance with the definition of that parameter. **Figure 5.9** shows how the actual normalized EL image of the module would look if one of the cells had a mild shunt (G_{SH} ~ 5 mScm^{-2}) and the current is ~ 2.2 mA/cm^2. If instead of a shunt we had a weak-microdiode the picture would be similar depending on the weak-microdiode severity. It is difficult to distinguish a shunt from a weak-microdiode using only C-contrast and a single EL current density.

Figure 5.10 shows comparison of C-contrast and CC-contrast. One cell in each case is shunted (bottom) and the other is uniform (top).

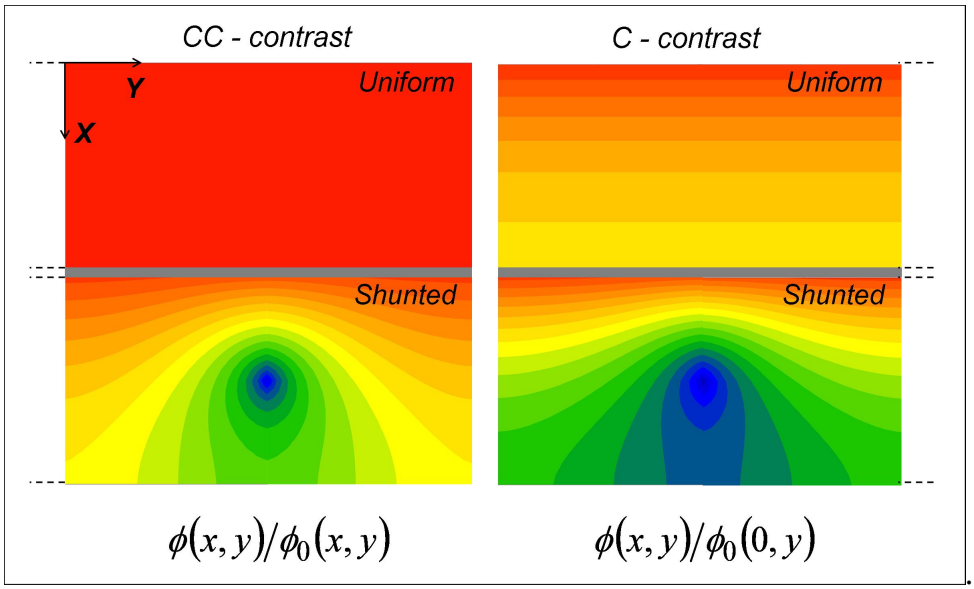

Fig.5.10. Calculated CC-contrast vs. C-contrast.

Obviously, for the uniform CC-contrast we have unity everywhere.

5.6. Range of interest for shunts

For the simplicity of further analysis, it is helpful to narrow the range of potential modules in terms of their absolute module efficiency loss due to multiple shunts. **Figure 5.11** is the same as **figure 4.7** in chapter 4. It shows absolute module efficiency loss as a function of relative shunted area A_S for different values of shunted subcell efficiencies.

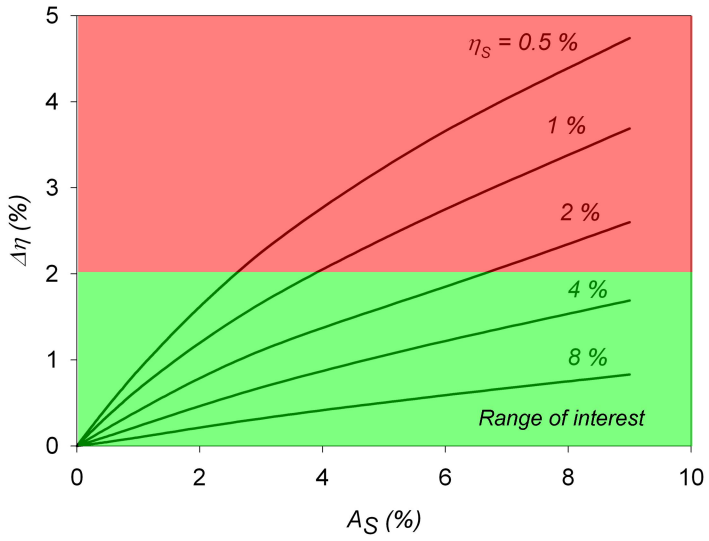

Fig.5.11. Absolute module efficiency loss. Green area with $\Delta\eta \leq 2\%$ is the region of practical interest.

This figure is presented here again to show the range of interest for the EL analysis conducted here. In the current work we will focus on the range colored in green for two reasons:

1. When the absolute module efficiency $\Delta\eta$ is small, the voltage across shunted and uniform cells is approximately equal. This significantly simplifies the analysis because it makes possible determination of single value for the current at which one can extract most information out of the EL data.

2. If the absolute module efficiency $\Delta\eta$ is too large, then the module is essentially unusable. Probably, in such situations the entire manufacturing process needs to be checked and fine-tuning based on EL analysis would not be helpful. Such modules will probably be discarded after basic module parameters are measured.

To get maximum information from the EL image of the module, we need to satisfy two primary conditions:

1. One would like to have highest possible C-contrast of the shunted area. This allows detecting the shunt.
2. One would also like to have highest possible overall intensity of the EL signal that is as large current as possible (best noise/signal ratio). The maximum current that one can practically drive through a module is limited to ~ (3-4)·J_{SC}.

5.7. Optimal current for shunt detection

In the previous section, it was stated that to get maximum information out of the EL data, one must use current that maximizes the C-contrast. The C-contrast depends on the difference in current between shunted and uniform subcells at the same voltage. This difference is given by:

$$\Delta J = J_{SHUNTED} - J_{UNIFORM} \tag{5.18}$$

, where $J_{SHUNTED}$ and $J_{UNIFORM}$ are dark current densities of shunted and uniform subcells respectively.

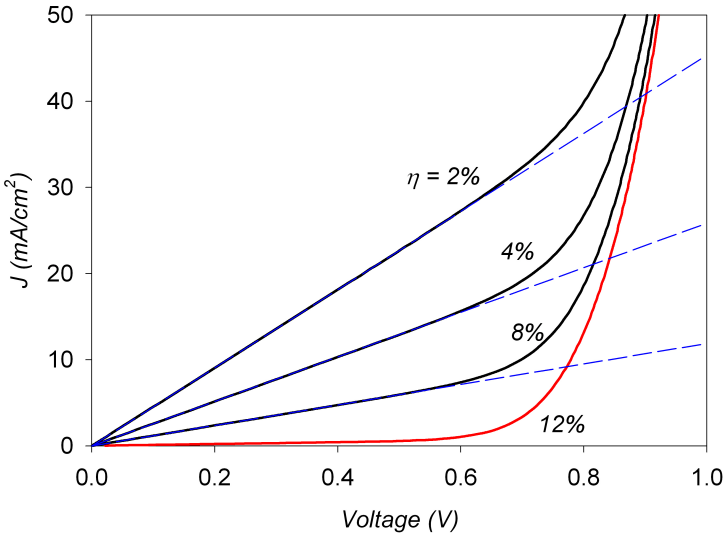

Fig.5.12. Shunted subcell *J-V* curves.

Figure 5.12 illustrates dark *J-V* curves of shunted subcells with different shunted-subcell efficiencies – 2, 4 and 8%. The red solid line is the baseline *J-V* curve from the uniform cell (η = 12%). Dashed straight lines represent linear approximations.

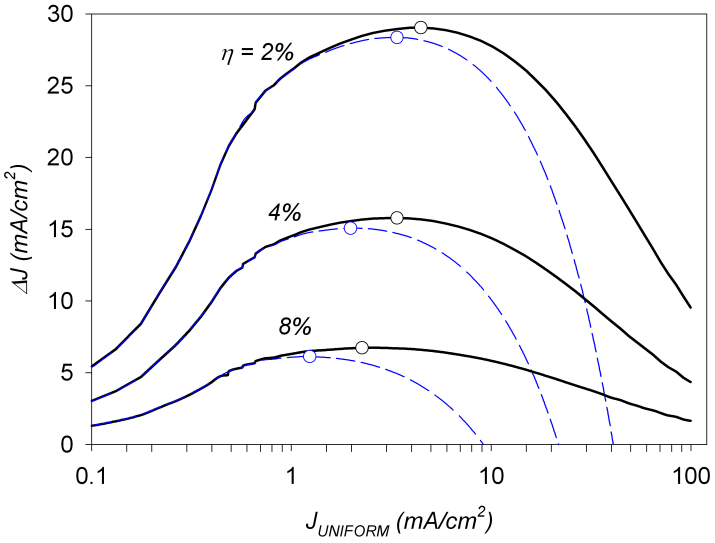

Fig.5.13. ΔJ vs. $J_{UNIFORM}$ for different η.

Figure 5.13 shows ΔJ as a function of $J_{UNIFORM}$ for different values of η. The dashed lines have similar meaning, but when $J_{SHUNTED}$ is approximated by a straight line as is shown on **figure 5.12**. Thus the maximum of ΔJ (that is the maximum of C-contrast) is at 2-3 mA/cm^2. The current at which the C-contrast is maximized can to a reasonable approximation be found analytically. Neglecting the parasitic resistances the dark current of the uniform microcell is given by:

$$j_U = j_0 e^{\beta V} \tag{5.19}$$

, where $\beta = q/AkT$. From (5.19):

$$V = \frac{1}{\beta} \ln\left(\frac{j_U}{j_0}\right). \tag{5.20}$$

Using a linear approximation for the shunted microcell $j_S = GV$, and with definition of Δj:

$$\Delta j = j_S - j_U = GV - j_U. \tag{5.21}$$

Substituting (5.20) into (5.21):

$$\Delta j = \frac{G}{\beta} \ln\left(\frac{j_U}{j_0}\right) - j_U. \tag{5.22}$$

Taking the derivative of (5.22) with respect to j_U and setting it to 0 we find the $j_{U\text{-}MAX}$ at which Δj is maximized:

$$j_{U-MAX} = \frac{G}{\beta}. \tag{5.23}$$

For example, $G \approx 30$ mScm^{-2} ($\eta = 4\%$) and $\beta = 20$ V^{-1} ($T = 300$K) yield $j_{U\text{-}MAX} = 1.6$ mA/cm^2 for the maximum EL C-contrast.

Thus the current at which the C-contrast is maximized is independent of most properties and basic parameters of solar cells and module geometry. It only depends on the conductance of the shunt that is the shunt severity.

5.8. The CC-contrast

So far, the focus has been on C-contrast. However, CC-contrast can also help to extract useful information from the EL-data.

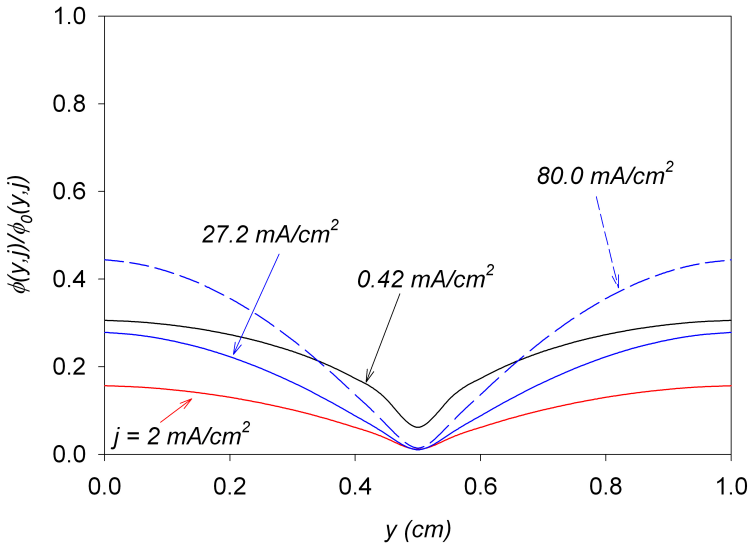

Fig.5.14. Calculated EL CC-contrast at $x = 0.5$, for different current densities.

For simplicity here shunt is used as test non-uniformity. Application of CC-contrast in case of weak-microdiodes is considered in section 5.10. **Figure 5.14** shows CC-contrast at $x = 0.5$ for different values of current. The shunt ($\eta = 4\%$) is located in the center of the subcell. **Figure 5.14** implies that higher current tends to localize the shunt. The CC-contrast grows very slowly as you move away from the shunt location ($y = 0.5$) and for low currents it might never reach unity because the cell width is limited. This means that at low currents, the EL signal from the entire width of the cell can be significantly affected by a single shunt. There are two competing aspects to this effect. On one hand, at low current it is easier to identify the shunted cell because the entire cell will have a lower EL signal compared to the uniform cell. Furthermore, the lower the EL signal from the shunted cell, the more severe the shunt is. This allows quantification of the shunt severity. On the other hand, at low current, it is harder and sometimes impossible to localize the shunt within the shunted cell. These conclusions are supported experimentally.

5.9. Experimental evidence

Experimental evidence presented here is based on the paper by Uwe Rau et al[2]. The paper presents experimental electroluminescence images of a CIGS mini-module at two different currents 1.25 and 50 mA/cm^2. The mini-module has typical thin-film geometry with 42 cells each 20 by 0.4 cm in size. The mini-module has 10-20 localized shunts of different severity. The fact that it is a CIGS rather than a CdTe baseline is not a problem because the qualitative conclusions are the same. There are, of course, other

experimental papers on electroluminescence, but they deal with lab-scale solar cells rather than modules, have different geometries or simply do not have color images with decent resolution. The paper by Rau et al provides a unique opportunity to verify some of the analytical and simulation conclusions.

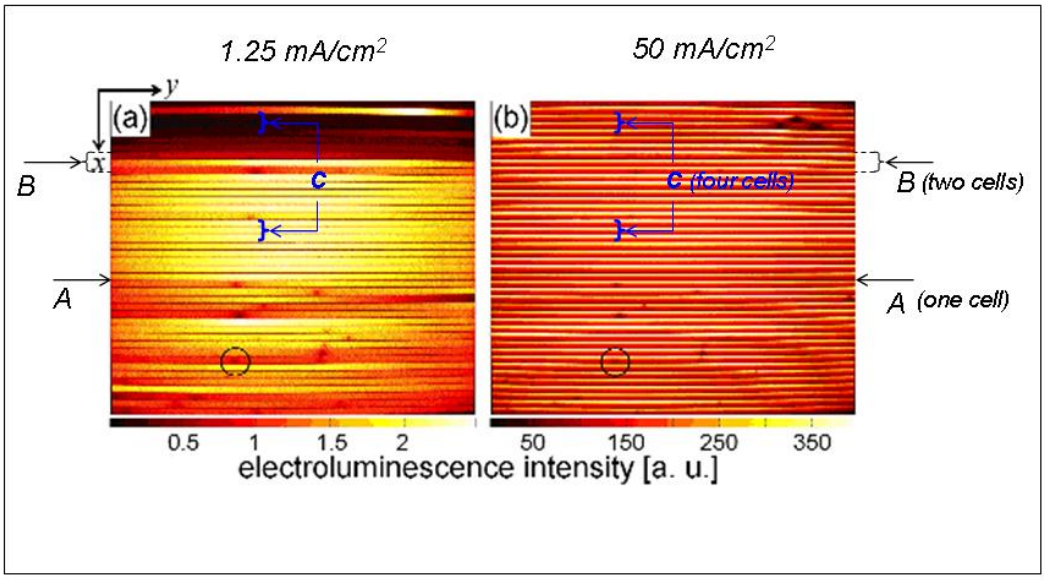

Fig.5.15. Experimental EL image of the CIGS mini-module (Ref. [2]).

Figure 5.15 shows experimental EL images of the CIGS mini-module at two different currents 1.25 and 50 mA/cm^2. The color bar below each image is the relative intensity (or the C-contrast) in arbitrary units (a.u.). The dark spots on both images indicate the presence of a shunt. To verify several of the conclusions we made earlier, we will focus on three sets of cells shown in **figure 5.15** at both currents: A (one cell), B (two cells) and C (four cells). Both B and C include shunted and uniform cells (CC-contrast), while A has shunted cell only (C-contrast).

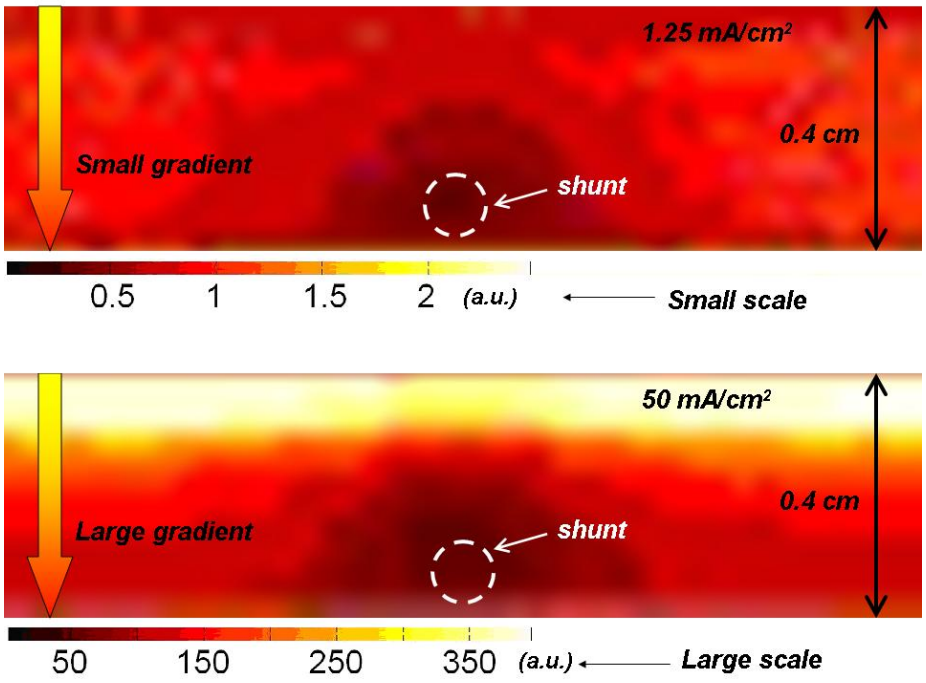

Fig.5.16. Close up EL image of cell A with small (top) and large (bottom) currents. (Ref. [2])

Figure 5.16 shows a close up EL image of a cell A at two different currents: 1.25 and 50 mA/cm^2. The shunt is located close to the edge of the cell (probably because of the scribe delineating the cell). The color scales are different, because the intensity of the EL signal depends on the current. This allows testing the assumption that $\phi \sim J^A$, which implies the following:

$$A = \frac{\ln\left(\phi_1 / \phi_2\right)}{\ln\left(J_1 / J_2\right)}. \tag{5.24}$$

Thus, ϕ_1 = 2 a.u., J_1 = 1.25 mA/cm^2, ϕ_2 = 350 a.u., J_2 = 50 mA/cm^2 yield a diode quality factor A = 1.4 (or the exponent b if earlier analysis is not valid), which is a reasonable

value for a thin-film solar cell (and falls within the range found by Price $1 \leq b \leq 2.5$). This observation implies that the assumption $\phi \sim J^A$ is at least plausible.

Figure 5.16 also shows that for small current, the intensity of the EL signal changes very little from the gridline to the other edge of the cell, while for the high current it changes significantly and rapidly in accordance with the analytical prediction (equation (5.17) and **figure 5.8**).

In principle, this experimental data allows one to calculate the sheet resistance using equation (5.17).

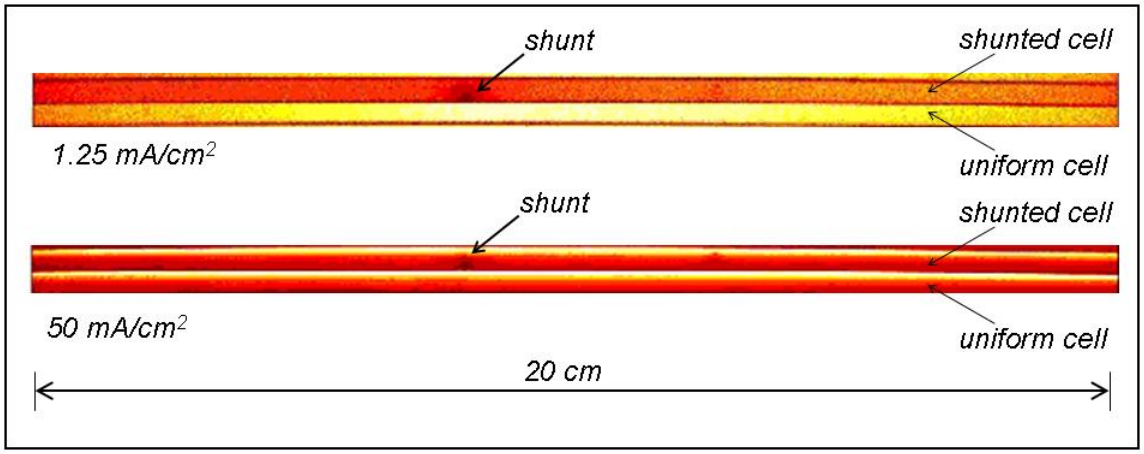

Fig.5.17. Close up EL images of cells B at two different currents (Ref. [2]).

Figure 5.17 shows a close up EL image of two cells shunted and uniform (set B) at two different currents. The fact that we are comparing shunted and uniform cells means that we are actually dealing with the CC-contrast. **Figure 5.17** implies that at small current the EL signals from shunted and uniform cells away from the shunt are significantly different. In other words, at small current the shunt affects the EL signal of the entire cell. At high current there is no difference in EL signal between shunted and uniform cell away from the shunt and the shunted area itself is very well localized.

Both **figures 5.15** and **5.17** show that at small current "uniform" cells have a few slightly dark regions at the edges (left and right). This is probably because there are weak shunts along the edges (left and right), probably also because of the scribing. At small currents one can detect both very weak and very strong shunts. This allows quantifying shunts by their severity with an appropriate calibration. All of these observations are in accordance with the conclusions obtained from simulations (**figure 5.14**).

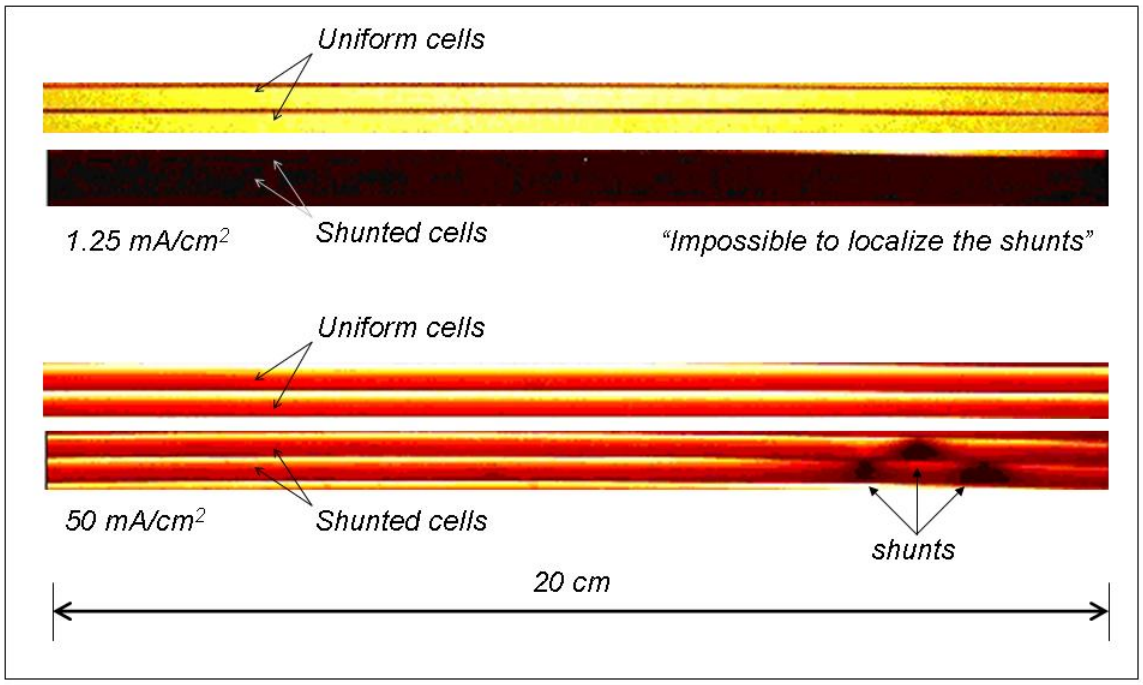

Fig.5.18. Close up EL images of cells C at two different currents (Ref. [2]).

Figure 5.18 shows a close up EL image of four cells (set C) at two different currents. As already mentioned, at small currents the shunt affects the EL signal of the entire cell. However, if the shunt is too severe then it becomes impossible to localize the shunt. In the example presented in the **figure 5.18** at small current one can tell that two cells are badly shunted, while at high current one can tell where the shunts within the shunted cells

actually are (shunt localization effect at high current). These observations are again consistent with conclusions obtained above from calculations (**figure 5.14**).

5.10. Weak – microdiodes vs. shunts

So far, only uniform and shunted cases have been considered. However, electroluminescence measurements can just as well be used to detect and quantify local weak microdiodes. In this section it will be shown how EL data can be used to not only detect non-uniformities but also to distinguish a shunt from a weak-diode.

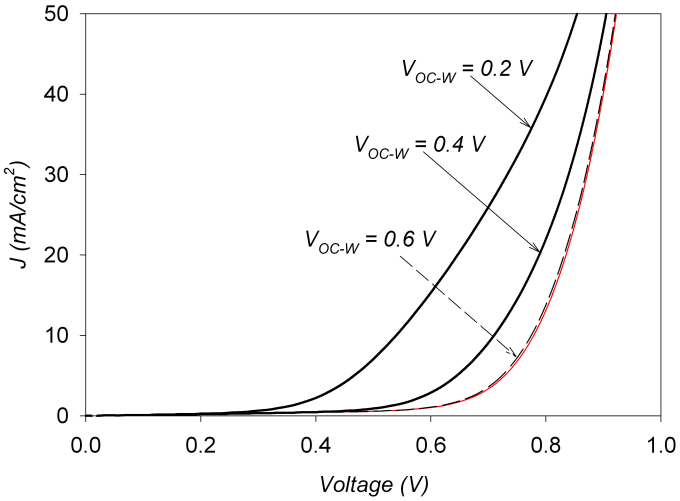

Fig.5.19. Subcell *J-Vs* with weak microdiodes in the center.

It is worthwhile to illustrate how dark subcell *J-V* curve is affected due to a weak microdiode in the subcell. **Figure 5.19** illustrates dark *J-V* curves of subcells for weak microdiodes with different values of $V_{OC\text{-}W}$ in the center of a subcell: 0.2, 0.4 and 0.6 V, while the baseline V_{OC} = 0.8 V. The red solid line is the baseline *J-V* curve from the uniform subcell.

It was found numerically that in the weak-microdiode case the optimal current for maximizing the C-contrast is slightly larger (~ 4-5 mA/cm^2) than it was for shunts. However, a closed-form analytic approach is much more difficult than it was for shunts.

Just as it was for shunts here the range of practical weak-diode interest is also limited. **Figure 5.20** is the same as **figure 4.13** in chapter 4. It shows absolute module efficiency loss as a function of relative weak area A_W for different values of weak-subcell open-circuit voltages.

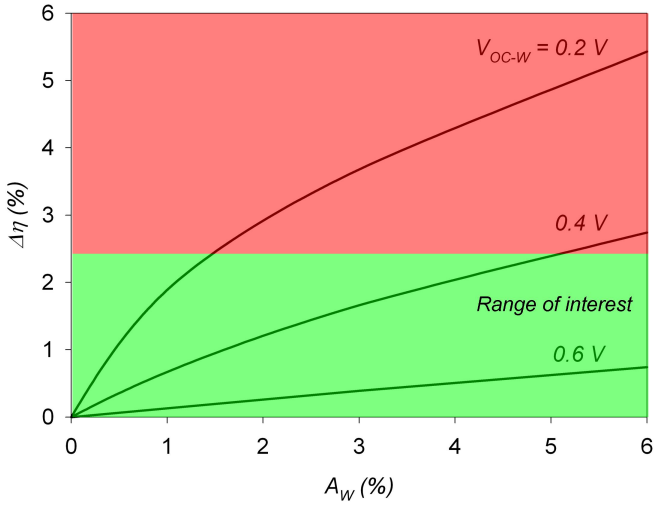

Fig.5.20. Absolute module efficiency loss. Green area with $\Delta\eta \leq 2\%$ is the region of practical interest.

The green area is the area of practical interest for the reasons similar to those mentioned in section 5.6.

It is very difficult to distinguish a shunt from a weak-diode using the C-contrast. However, analysis of the CC-contrast allows developing a strategy to distinguish a shunt from a weak-diode.

Figure 5.21 shows the calculated CC-contrast (at x = 0.5) of a subcell with a mild (A: $V_{OC\text{-}W}$ = 0.6 V) and a severe (B: $V_{OC\text{-}W}$ = 0.2 V) weak microdiode in the center of the

subcell for different values of current j = 1, 4, 10, 40 and 100 mA/cm^2. **Figure 5.21** implies that the minimum of the CC-contrast and the curve itself shift down with increasing current independent of the weak-microdiode severity (though in the severe cases curves may intersect). Furthermore, comparison of **figures 5.21-a** and **-b** implies that in the mild weak-microdiode case the minima are spread, while as the weak-microdiode becomes more severe, the minima tend to both bunch and shift down. This allows a quantification of weak microdiodes in increasing order of their impact.

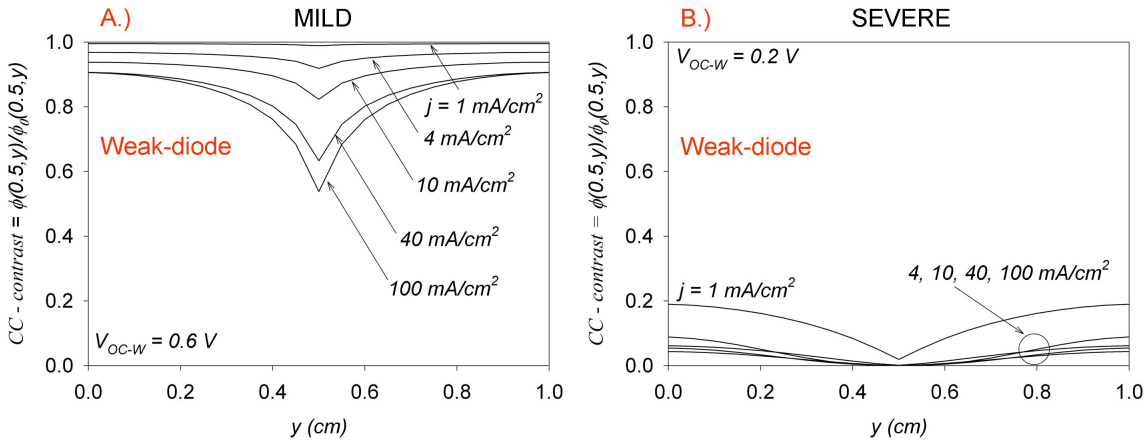

Fig.5.21. Calculated CC-contrast of a subcell with a mild (A) and severe (B) weak microdiode.

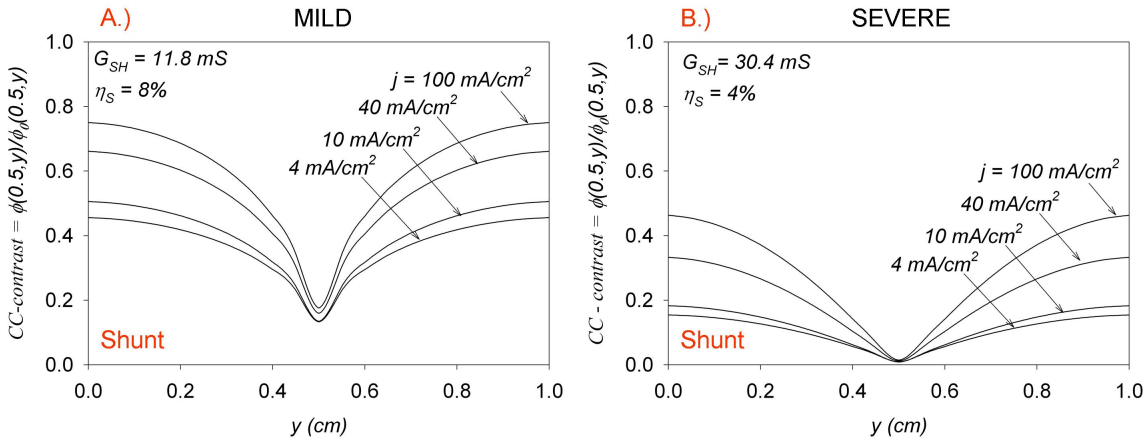

Fig.5.22. Calculated CC-contrast of a subcell with a mild (A) and severe (B) shunt.

Figure 5.22 shows the CC-contrast (at x = 0.5) of a subcell with a mild (A: G_{SH} = 11.8 mS, η_S = 8%) and severe (B: G_{SH} = 30.4 mS, η_S = 4%) shunt in the center for different values of current j = 1, 4, 10, 40 and 100 mA/cm^2. **Figure 5.22** implies that CC-curves shift upward as current increases, independent of the shunt severity. Thus, in the case of shunt the progression of curves with increasing current is opposite to what is seen for weak-microdiodes. This is the primary criterion that helps one distinguish a shunt from a weak-microdiode. **Figures 5.22 -a** and **-b** also imply that minima at different currents are bunched together independent of the shunt severity. However, all minima shift down as shunt gets more and more severe. This is another criterion that can be used to distinguish a shunt from a weak-microdiode and to quantify the shunt severity.

There is another subtle difference between the patterns of CC-contrast in the shunt and weak-microdiode cases. In section 5.8 it was mentioned that for shunts the curve representing the CC-contrast tends to localize the shunt with increasing current. In other words, the minimum of the CC-contrast curve for a shunt "narrows down" and becomes "sharper". However, this is less true in the weak-microdiode case, where there is "parallel shift" of curves and hence, a secondary criterion for distinguishing shunts from weak microdiodes.

Figure 5.23 presents a chart that highlights the differences between the CC-contrast of the shunt and weak-microdiode in a systematic fashion. It is recommended to do EL measurement at three different currents: ~ 1-4 mA/cm^2, ~ J_{SC} and ~ (2-3)·J_{SC} (red). This is consistent with Ref. [2], which used 1.25 and 50 (about 1.5·J_{SC}) mA/cm^2.

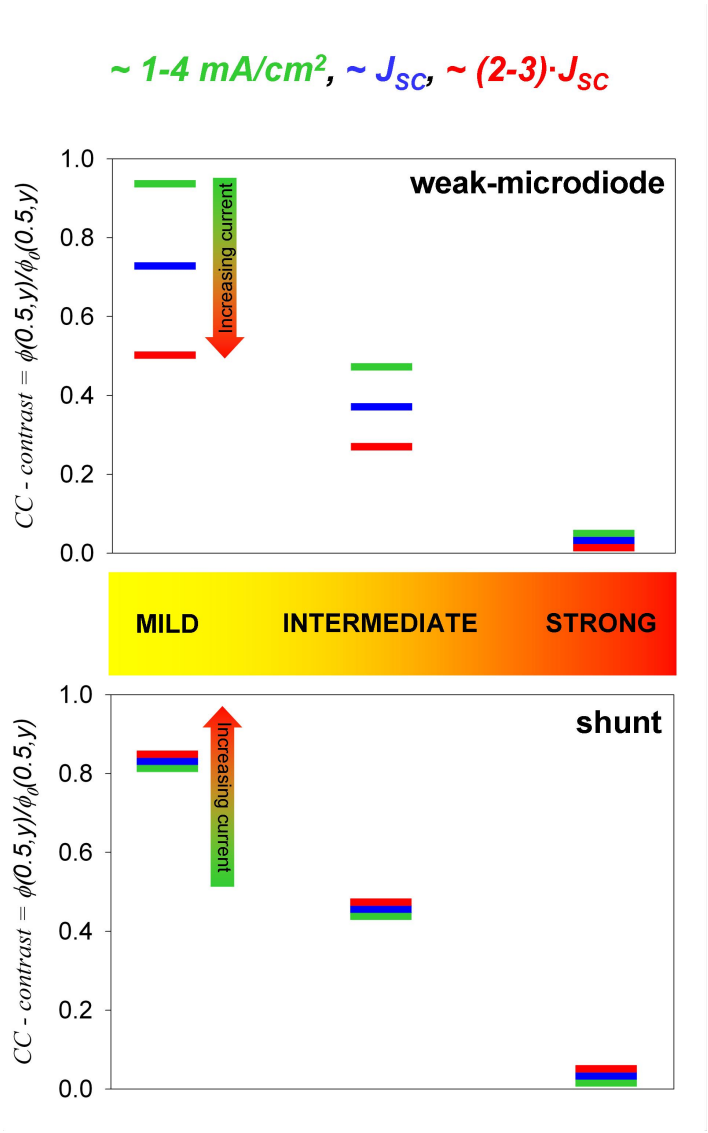

Fig.5.23. Chart summarizing: weak-microdiodes vs. shunts.

The summary chart in the **figure 5.23** highlights the general trends of CC-contrast curves and their minima. For example, the progressions of color bars in the two cases are opposite. For the weak-microdiode, minima at different currents not only decrease, but also change from being spread to being bunched as the microdiode increases in severity. For the shunt, minima are bunched independent of the shunt severity and decrease with it.

5.11. General recommendations

Electroluminescence measurements coupled with 2-D numerical and analytic calculations can indeed be a powerful tool in the analysis of thin-film modules both in research labs and as an in-situ measurement in the manufacturing process. The functional form of the C-contrast (equation 5.17) can be used to predict the EL image of the uniform cell depending on the current, sheet resistance and module geometry. High resolution EL data of uniform cells in a module can be used to determine the sheet resistance.

The general strategy of experimental module analysis using EL measurement should consist of five basic steps:

1. EL measurements should be at three different currents: ~ 1-4 mA/cm^2, ~ J_{SC}, ~ (2-3)·J_{SC}.
2. A 2-D C-contrast image of the module should be produced for the smallest current (~ 1-4 mA/cm^2) to note which cells in the module have non-uniformities: dark spots somewhere in the cell (low EL signal), the whole cell is darker, etc.
3. 1-D CC-contrast plots should be made at all three currents of non-uniform cells. (The *Y*-coordinate is the variable and *X* is fixed at the location of the non-uniformity.) If it is not possible to accurately determine the *X*-coordinate of the non-uniformity from the C-contrast at small current, then identify it from the C-contrast at the highest current ~ (2-3)·J_{SC}.
4. Based on the 1-D CC-contrast plots at all three currents and using criteria mentioned in section 5.10, distinguish shunts from weak-diodes.

5. Based on 1-D CC-contrast plots at all three currents and using criteria described in section 5.10 put non-uniformities in increasing order of severity. For example, assign labels such as mild, intermediate, severe, and extremely severe, keyed to impact module performance.

Additionally, for a manufacturer to implement an EL measurement system for uniformity screening, it is highly recommended to do a systematic calibration of stand-alone cells (that have same geometry, as cells in a module) that have an externally induced shunt or a weak-diode of varying severity. Such calibration at different currents should allow one to quantify non-uniformities in terms of the absolute power loss, rather than assign them labels (mild, intermediate, severe, etc) as recommended in step 5. The final product of such systematic calibration would be a chart that would establish a one-to-one correspondence of CC-contrast minima at a given current and the absolute power loss of the stand-alone cell at MPP. Such systematic calibration can be done initially and then the patterns (graphs or charts) used for the in-situ analysis.

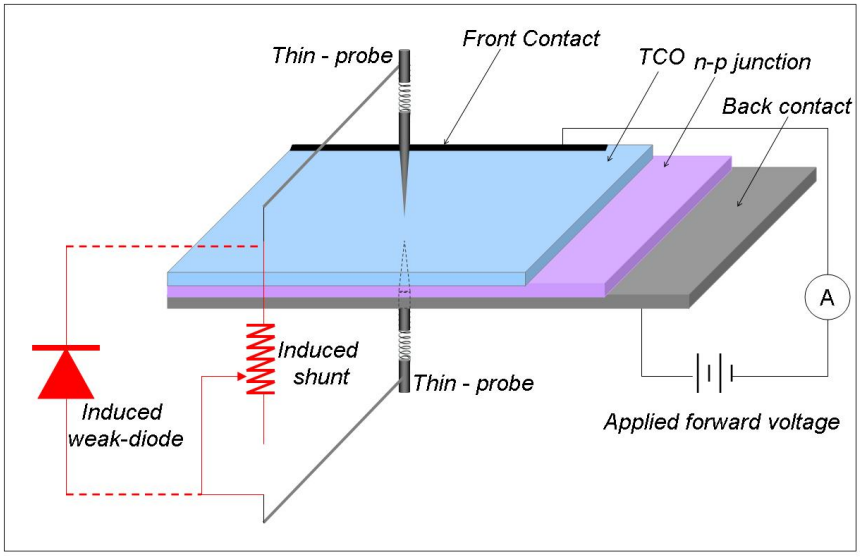

Fig.5.24. EL measurement of the stand-alone cell with the externally induced non-uniformity.

Figure 5.24 shows a schematic of the EL measurement of the stand-alone cell with an external circuit element to simulate non-uniformity (shunt or a weak-diode) of known and variable severity. The top-probe should be very thin to not obstruct the emitted EL radiation. Ideally one would like to have two probes at the same location opposite to each other in contact with TCO and back-contact-metal respectively. However, in the substrate configuration the back-contact-metal is covered with glass, and the back-contact bottom probe can only be connected at the edge of the cell where current is collected. This is not a serious problem because back-contact-metal is very conductive. In the superstrate configuration, however, the situation is opposite: the TCO layer is covered with glass while the back-contact-metal is accessible everywhere, but the TCO is very resistive and same approach will not work. This means that in the superstarte configuration the external circuit element to simulate non-uniformity can only be placed at the very edge of the cell.

Thus, we have seen that electroluminescence from photovoltaic devices, which continues to gain popularity, is indeed a very promising spatially resolved characterization technique when coupled with 2-D modeling. Electroluminescence measurements can be very valuable when integrated as screening and analysis tool in the manufacturing process. The simplicity of the measurement setup, its analysis capabilities and relatively small cost (the CCD camera, which is the primary piece of the whole setup costs about $18,000.00-$25,000.00) make electroluminescence measuring system a good investment for a PV company. The benefit is particularly true for thin-film PV companies

because thin-film solar cells are inherently non-uniform and non-uniformities are the primary source of power loss.

Chapter 6
Effect of shading on thin-film modules

The chapter discusses the effect of partial shading on operation of thin-film modules. A mathematical formalism of current-voltage characteristics of thin-film solar cells in reverse bias is developed on the basis of theoretical and empirical findings for crystalline cells. The formalism is then used to analyze power conditioning of a partially shaded module. In particular, power dissipation in shaded cells and their temperature increase is investigated.

6.1. Shading as a type of non-uniformity

As opposed to shunts, weak-diodes or any other microscopic types of non-uniformities, which can be analyzed and studied on the lab-scale solar cells, partial shading is a macroscopic type of non-uniformity that takes place at the PV module level when it operates out in the field. In fact partial shading is a non-uniformity in the level of illumination.

Figure 6.1 illustrates different obstructions that can cause partial shading of PV modules out in the field. Adjacent solar panels can potentially cause shade on each other

if the available space is limited. Non-uniformity in illumination over a string of cells connected in series is a particular case of mismatch in a module.

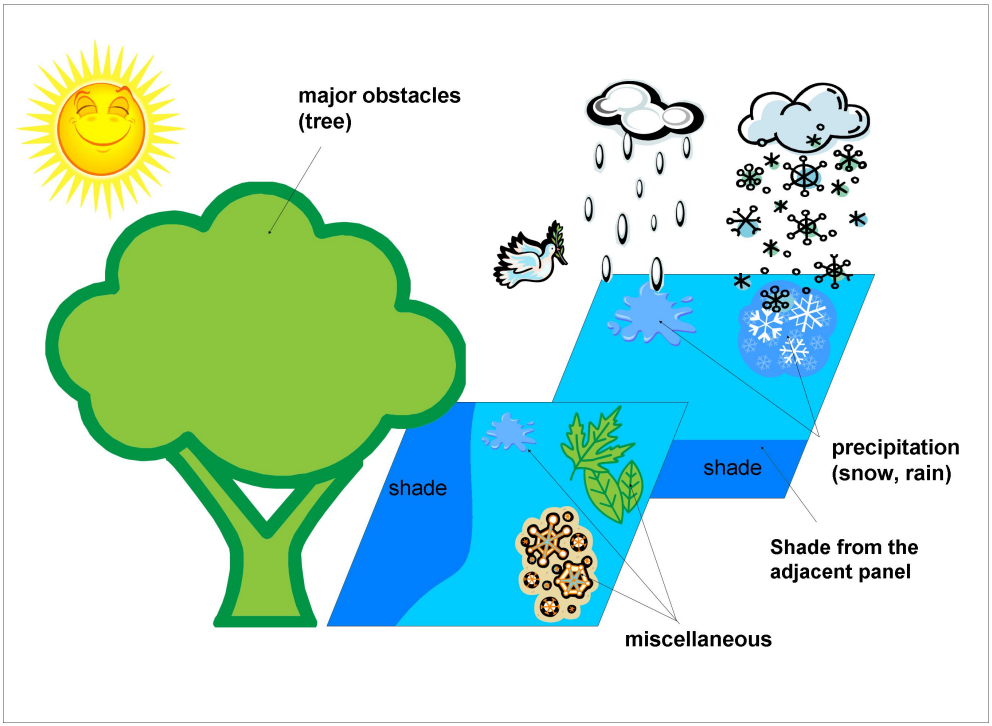

Fig.6.1. Different causes of partial shading.

Besides differences in illumination over a single module, there can also be partial shading of large PV arrays. Also PV modules in a string are never exactly identical, even without partial array shading. The overall efficiency of the array is reduced to near the efficiency of the worst performing module in the array if there are no active electronics to compensate. One way to avoid the mismatch is to use DC-AC inverters which connect every module or a sub-string of several modules separately to the AC grid. Another way to avoid mismatch problems is to place a DC-DC converter on each sub-string of modules and connect these sub-strings in series[16,17]. The work here,

however, will focus on the mismatch between individual cells within a module due to partial shading.

In the crystalline PV industry solar cells in the module are categorized into different performance bins[18,19], different interconnection patterns (bridge-linked, series-parallel, etc.) are used, and bypass diodes or other types of fault tolerant circuitry[20,21,22] are integrated. However, binning methods are only applicable when solar cells are manufactured individually and are then connected into a module. This is generally not the case for thin-film PV modules. A thin-film module is most often produced as a single monolithic piece, and if one of the cells has a fault or otherwise causes a mismatch, one cannot simply remove the undesired cell and replace it with another one. Individual cells in thin-film modules are connected in series, and application of intricate interconnection patterns is not common, since this would complicate the production line and add additional expense. Bypass diodes and other fault-tolerant circuitry are not usually integrated into individual cells in a thin-film module for the same reason. Therefore, mismatch problems are more critical for thin-film panels, and partial shading of thin-film panels and related issues need to be studied in a systematic fashion.

Partial shading of a PV module may cause several problems related to module deterioration and its safety. In a typical thin-film module cells are connected in series. When some cells in the module are shaded, they are forced by other illuminated cells into the reverse bias, which, depending on the cell parameters, can become quite large. If cells are not tolerant to large reverse voltages, ones that are shaded can be permanently damaged. Furthermore, because of the high reverse voltage across the shaded cell, a large amount of power may be dissipated in the single cell. In some cases, the high generated

temperature can result in physical deterioration of the module which may cause cracking, delamination of layers, or other serious problems.

The operation of a partially shaded thin-film module is essentially determined by the reverse voltage characteristics of shaded cells. However, little attention has been paid to reverse bias characteristics of *J-V* curves of thin-film solar cells. Therefore, we first discuss the mathematical formalism of the *J-V* curve in the reverse bias.

6.2. Mathematical formalism of the *J-V* characteristics in the reverse bias

In this section we briefly discuss physical principles behind the reverse voltage characteristics of the solar cell, Miller's empirical relation, and the mathematical formalism that can be used to analyze the consequences of partial shading.

6.2.1. Theoretical background of the breakdown mechanisms

At a sufficiently high reverse bias, breakdown of the p-n junction takes place and large current flows through the junction. There are two primary physical models that explain this effect in different circumstances.

In 1934 C. Zener published his paper titled "A Theory of the Electrical Breakdown of Solid Dielectrics"[23]. In that paper he made the first attempt to give a physical explanation of the breakdown mechanism based on internal field emission. It was later found that such physical mechanism takes place only when both sides of the p-n junction are heavily doped and the depletion layer is very thin.

In 1953 K.G. McKay[24] suggested a different explanation of Si and Ge p-n junction breakdown, which in fact was an extension of Townsend's β-avalanche breakdown theory in gases. Since then many researchers in the field verified the validity of McKay's theory of the avalanche breakdown in such p-n junctions.

The model used to analyze the effect of partial shading of the module deals only with numerical *J-V* curves of microcells. These, in principle, can be obtained experimentally without referring to physical origins. Thus, the obtained simulation results do not depend on the actual physical mechanisms that determine the microcell *J-V* curve. However, understanding what physical mechanism is responsible for the breakdown is important because it allows development of a realistic mathematical formalism and parameterization of the *J-V* curve, which makes simulations more universal and practical. Therefore, both Zener and Avalanche breakdown mechanisms are discussed further below.

Most of the research[24,25,26,27] on the diode breakdown effect was done on crystalline Si and Ge p-n junctions, while the behavior of thin-film polycrystalline or amorphous solar cells under reverse bias has generally been overlooked. However, with appropriate assumptions, the theoretical and empirical results obtained for crystalline Si and Ge p-n junctions can be applied to model *J-V* characteristics of thin-film solar cells.

6.2.2. Zener breakdown

The Zener process is the name given to the occurrence of "tunneling" in the reverse biased diode. If the electric field in the depletion region is sufficiently large it will

tend to displace valence electrons with respect to their atomic cores. Thus, the electric field will tend to break the bonds. According to Zener's theory, a spontaneous breaking of the valence bonds occurs before the electric field is large enough to rupture them directly. As a result of this spontaneous breaking which is induced by strong electric fields, generation of hole-electron pairs will occur in the diode's depletion region[23,28]. In other words, valence electrons on p-side of the junction pass through the barrier to empty states at the same energy in the conduction band on the n-side of the junction. The greater the reverse bias, the larger the number of filled valence-electron states on the p-side placed opposite empty conduction-band states on the n-side, and hence the greater the reverse-bias tunneling current. For tunneling to be significant, the barrier thickness, roughly the depletion width, must be $<10^{-6}$ cm (0.01 μm), which is much thinner than the typical thin-film solar cell depletion width (~ 1-10 μm). The Zener process is therefore important only in diodes that are heavily doped on both sides of the junction[29] and have very thin depletion width. Thus, Zener's breakdown mechanism is not likely to take place in thin-film p-n junctions.

6.2.3. Avalanche breakdown

Avalanche breakdown theory for semiconductors is a modified version of the simple gas discharge theory, which states that the breakdown mechanism in p-n junctions is a direct result of multiplication by collision. For the sake of mathematical formalism discussed in the following sections, it is important to understand the physical meaning of the multiplication factor introduced here.

Following the brief description of the theory as suggested by McKay[24] and Miller[26] in the Townsend's β-discharge theory, the rate of ionization $\alpha_i(E)$ is defined as the number of electron-hole pairs produced by an electron per centimeter it travels in the direction opposite to the electric field E. In the same manner we define $\beta_i(E)$ as the number of electron-hole pairs produced by travelling holes.

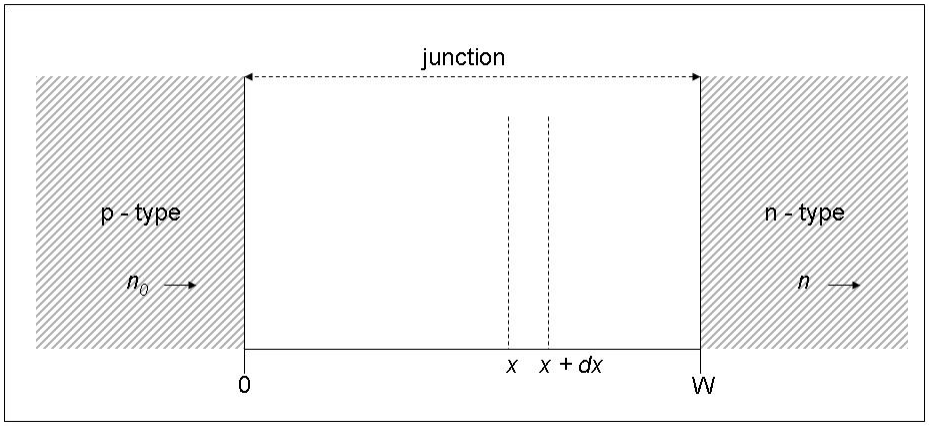

Fig.6.2. The geometry assumed for calculation of avalanche multiplication.

Figure 6.2 illustrates the geometry of the problem; n_0 is the number of electrons entering the junction at $x = 0$, n_1 is the number of electrons produced by electrons or holes between 0 and x, and n_2 is the number of electrons produced between x and W. Then the number of electrons produced between x and $x + dx$ is:

$$dn_1 = (n_0 + n_1)(\alpha_i - \beta_i)dx + (n_0 + n_1 + n_2)\beta_i dx. \tag{6.1}$$

Integrating equation (6.1) with boundary conditions $n_1(0) = 0$ and $n_2(W) = 0$ we get:

$$1 - \frac{1}{M} = \int_0^W \alpha_i \exp\left[-\int_0^x (\alpha_i - \beta_i)dx' \right] dx, \tag{6.2}$$

where $M = (n_0 + n_1 + n_2)/n_0$ is the multiplication factor. The breakdown occurs when $M \rightarrow \infty$, corresponding to the integral reaching unity.

6.2.4. Miller multiplication factor

Miller showed that the multiplication factor in the avalanche breakdown theory for Ge and Si p-n junctions can be expressed by the following empirical relation[26,27]:

$$M(V) = \frac{1}{1 - \left(V / V_B \right)^n}, \tag{6.3}$$

where V_B is the breakdown voltage and parameter n is a number which depends on the resistivity of the low carrier density side of a step-like p-n junction. Miller found that for Si and Ge the values of the exponent n range from 2 to 6. In the empirical expression (6.3) the breakdown voltage is defined as the voltage when the multiplication factor is essentially infinite.

The breakdown voltage depends on temperature. If the temperature is increased the phonon scattering is enhanced and the average distance between two collisions is reduced. This means that a larger electric field is needed to achieve the threshold kinetic energy, and hence the increase in temperature increases the breakdown voltage (positive temperature coefficient). Incorporation of temperature dependence significantly complicates the model. Therefore, since the model developed here is essentially phenomenological rather than fundamental, the breakdown voltage of thin-film solar cells V_B is assumed to be weakly dependent on temperature.

6.3. Reverse bias characteristics of thin-film solar cells

There has been no systematic experimental study of reverse bias characteristics of thin-film solar cells, and no rigorous theory has been developed, because the physical structure of polycrystalline thin-film solar cells is granular and is therefore more complex than the structure of crystalline ones. It has been found, though, that the breakdown in thin-film solar cells occurs at lower voltages and is less abrupt than that of crystalline ones.

A reasonable way to model a thin-film solar-cell behavior in reverse bias is to apply the framework from crystalline solar cells. Thus, **figure 6.3** shows the circuit diagram of a microcell with the voltage-dependent Miller multiplication factor (6.3).

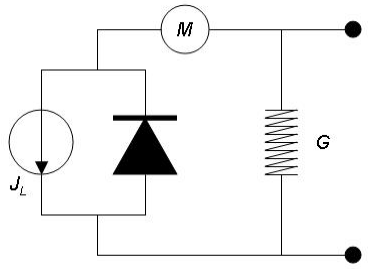

Fig.6.3. Circuit diagram of a microcell with Miller multiplication factor.

Figure 6.3 implies that the microcell *J-V* can be represented as follows:

$$j(V)=\begin{cases} j_0\left(e^{\beta V}-1\right)-j_L+GV, V\geq 0 \\ \left(j_0\left(e^{\beta V}-1\right)-j_L\right)\cdot M(V)+GV, V\leq 0 \end{cases}. \tag{6.4}$$

Using a similar approach Spirito and Albergamo[30] distinguish two types of solar cells depending on their reverse bias *J-V* characteristics: a.) ones dominated by avalanche multiplication; b.) ones dominated by shunt conductance. Such differentiation of solar cells by two types has been adopted[31] by International Standards (IEC 61646).

Miller's multiplication term has been used in different ways to model behavior of the *J-V* curve in the reverse bias by a number of other researchers as well[31,32]. Depending on the dominating factor in the equation (6.4) (*M(V)* or *G*) we can have the two qualitatively different operations of a partially shaded module.

6.3.1. Breakdown vs. shunt

Figure 6.4 illustrates examples of subcell *J-V* curves with different mechanisms that dominate in the reverse bias.

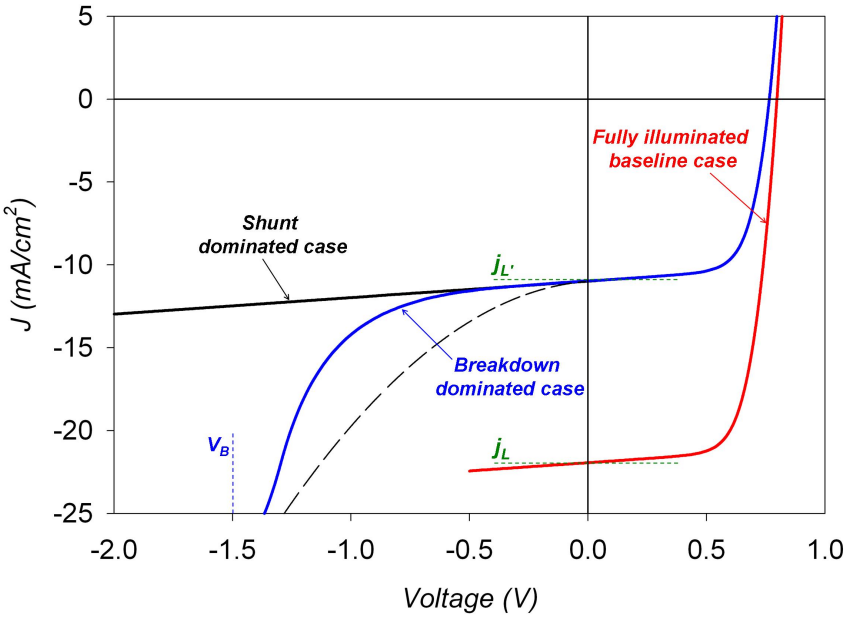

Fig.6.4. Subcell *J-V* curves.

Both breakdown and shunt dominated subcells are 60% shaded. The red curve represents baseline *J-V* of the fully illuminated subcell. The microcell *J-V* curve used to generate the subcell *J-V* curve for the breakdown dominated case is given by equation (6.4), with *n* =

4, V_B = -1.5 V, and G = 1 mScm^{-2}, while for the shunt dominated case V_B = - ∞ and G = 1 mScm^{-2}. In the following sections the partial shading of the module is analyzed for both extremes separately.

There is experimental evidence[31] that sometimes neither regular shunt nor breakdown dominates. For example, such a *J-V* curve is shown in **figure 6.4** by a dashed line. These types of intermediate situations (when neither shunt nor breakdown dominates) will not be considered in the present work. Operation of a partially shaded module in such situations can be deduced from the analysis of two extremes.

6.3.2. Analysis of partial shading of a module at the short-circuit

It is useful to consider a short circuit condition to show why shaded cells (if there are only a few of them) in the partially shaded module are reverse biased.

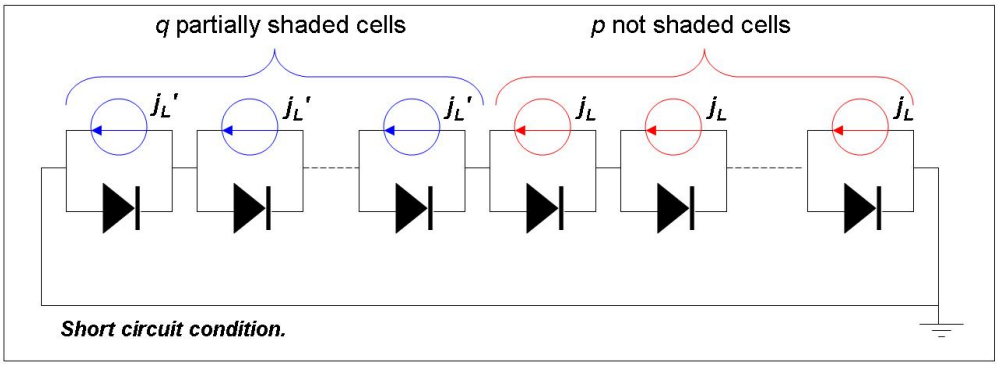

Fig.6.5. Circuit diagram of the partially shaded module with p+q cells.

Figure 6.5 shows the circuit diagram of the short-circuited module with q equally shaded cells and p fully illuminated ones.

Figure 6.6 shows *J-V* curves of fully illuminated cells in red and partially (50%) shaded cells in blue for the breakdown dominated case. **Figure 6.6** illustrates a step by step iterative process of how cell voltages can be found (in the shunt dominated case the logic is the same).

Since all cells are connected in series the current j that flows through each cell must be the same. In the first iteration we assume that the maximum current j_1 that passes through the fully illuminated cell is equal to the short circuit current of the stand alone shaded cell.

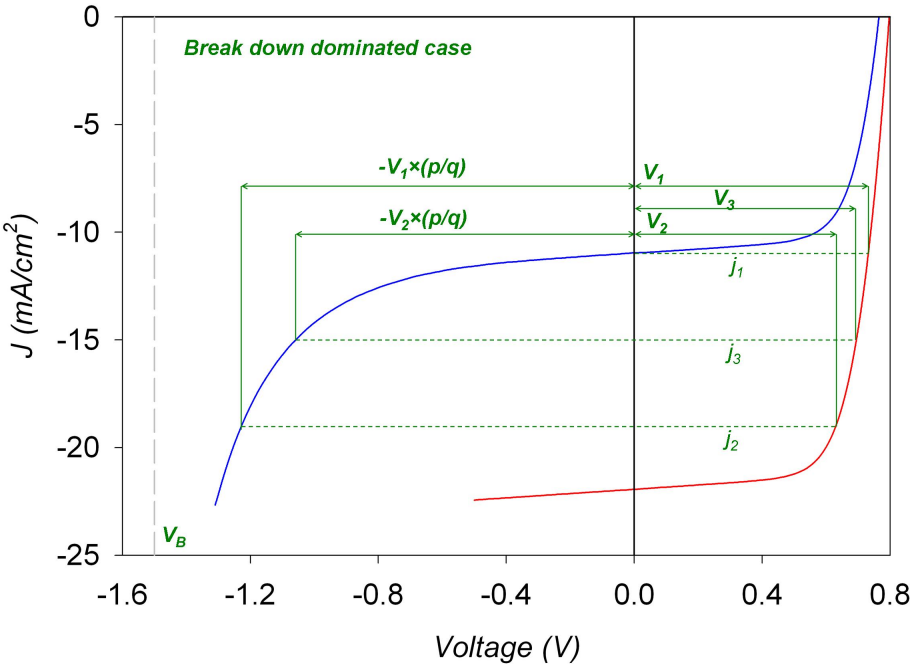

Fig.6.6. Calculated current-voltage of shaded and non-shaded cells in a module for the breakdown dominated case.

At j_1 the fully illuminated cell has voltage V_1. Since cells are connected in series and the module is short-circuited all voltages across cells have to add up to zero, which implies that the voltage across the shaded cell has to be $-V_1 \times (p/q)$. However, at that voltage the shaded cell has current j_2, which is different from j_1, while the fully illuminated cell at

that current has voltage V_2. This in turn implies that voltage across the shaded cell has to be $-V_2 \times (p/q)$. This is now the second iteration. **Figure 6.6** shows that the current of the third iteration j_3 is in-between j_1 and j_2, which means that the iteration process is converging. This iterative process illustrates why shaded cells are in reverse voltage. The exact value of the voltage V_S across the shaded cell in both breakdown and shunt dominated cases is derived in the following section.

6.3.3. Voltage across the shaded cell in a module at the short-circuit

Depending on the ratio (p/q) the current that passes through each cell may be less than the short-circuit current of the fully illuminated cell. However, in the present work we consider the more dramatic situation when most of the cells are fully illuminated and only few are partially shaded ($q \ll p$). This implies that in the short-circuited, partially shaded module, the current that passes through each cell is the short circuit-current (or equivalently light generated current) j_L of the fully illuminated cell.

To find the voltage across the shaded cell, let's first consider the breakdown dominated case. Using a lumped-series-resistance approximation the *J-V* curve of the shaded cell in the breakdown dominated case can be described as:

$$j' = \left(j_0 \left(e^{\beta (V - R_S j)} - 1 \right) - j_L{}' \right) \cdot M(V) + GV, \tag{6.5}$$

where $M(V)$ is the Miller's multiplication factor given by equation (6.3) and the prime superscript (') refers to the shaded cell. In reverse bias ($V<0$) and when the shunt is insignificant, equation (6.5) can be simplified as follows:

$$j'(V) \cong -j_L{}' M(V) = \frac{-j_L{}'}{1-(V/V_B)^n}. \tag{6.6}$$

The voltage V_S across the shaded cell can be found from $j'(V_S) = -j_L$. Thus, from equation (6.6):

$$-j_L = \frac{-j_L{}'}{1-(V_S/V_B)^n}. \tag{6.7}$$

After mathematical simplifications from (6.7):

$$V_S = V_B(1-\gamma)^{1/n}, \tag{6.8}$$

where $\gamma = j_L'/j_L$ is the illumination coefficient (wavelength independent). The illumination coefficient is $0 < \gamma < 1$, where 0 corresponds to no illumination (complete shading) and 1 to full illumination (no shade).

In the shunt dominated case (large V_B) at $V < 0$ from (6.5):

$$j' \cong -j_L{}' + GV. \tag{6.9}$$

Setting $j'(V_S) = -j_L$ from (6.9):

$$V_S = -\frac{j_L}{G}(1-\gamma). \tag{6.10}$$

Both equations (6.8) and (6.10) are true only when:

$$|V_S| < V\left(j_L{}'\right) \times \frac{p}{q}. \tag{6.11}$$

However, since $V(j_L')$ < V_{OC}, one can also set stronger and more practical conditions separately for (6.8) and (6.10):

$$\begin{aligned} &\text{For the breakdown dominated case: } V_S = V_B(1-\gamma)^{1/n}, \text{ when } |V_B| < V_{OC} \times \frac{p}{q}; \\ &\text{For the shunt dominated case: } \quad V_S = -\frac{jL}{G}(1-\gamma), \text{ when } \left|\frac{j_L}{G}\right| < V_{OC} \times \frac{p}{q}. \end{aligned} \tag{6.12}$$

Even though equations and inequalities (6.12) are derived when the module is at short-circuit, they can be applied when the module is connected to a load and operates at maximum power point. This is because $j_{MP} \approx j_L$ and V_S is a weak function of j_L' in both breakdown and shunt-dominated cases.

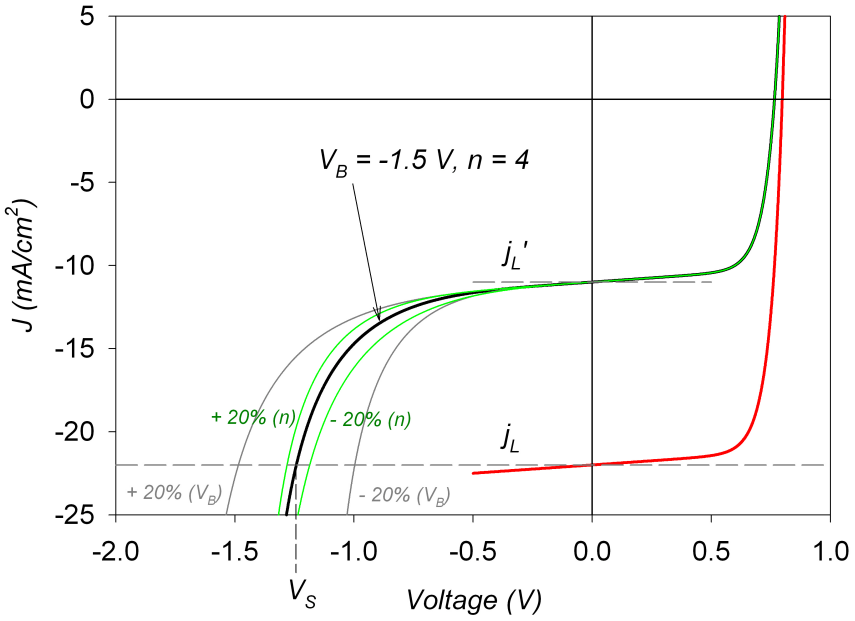

Fig.6.7. Variation of a cell's *J-V* curve in the breakdown-dominant case with V_B and n.

In the shunt-dominated case, V_S can be very large. For example, baseline values j_L = 22 mA/cm^2 and G = 1 mS/cm^2 yield V_S = - 22.0 V at γ = 0. In the breakdown dominated case, V_S values are generally much lower. Typical values V_B = - 1.5 V and n = 4 yield V_S = -1.5 V at γ = 0.

Experimental data for Miller's exponent n, as opposed to V_B, is only available for crystalline solar cells. Numerical values of n used in the simulations here are purely speculative. It is, therefore, important to know how sensitive equation (6.8) is to variation in n. **Figure 6.7** illustrates a set of cell J-V curves at γ = 0.5 with varying parameters V_B and n. The black line represents a J-V curve when V_B = -1.5 V and n = 4, green when V_B = -1.5 V but n = 4 ± 20% and grey when V_B = -1.5 V ± 20% and n = 4. Both equation (6.8) and **figure 6.7** imply that V_S is much more sensitive to variation in V_B than n. **Figure 6.8** illustrates how sensitive V_S is to V_B and n as a function of the illumination coefficient γ.

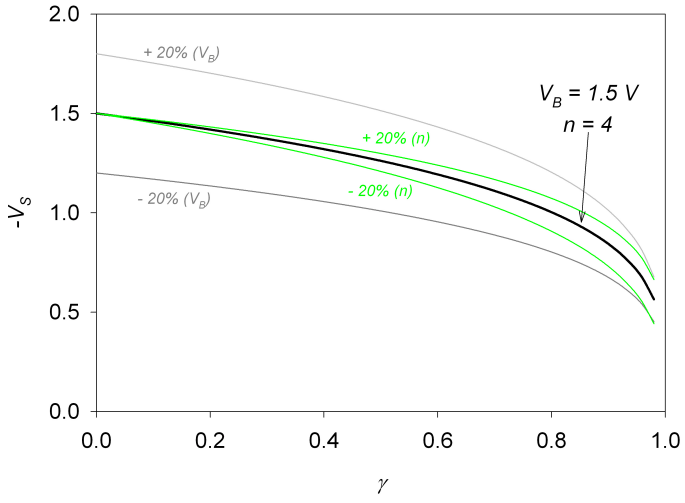

Fig.6.8. Voltage across the shaded cell as a function of illumination coefficient.

Figure 6.8 shows that for the region of most interest (values of γ less than 0.6), variation in n has only a very small effect on V_S, which partially justifies application of experimental values of n obtained for crystalline (Si and Ge) solar cells to thin-film solar cells. In the simulations to follow $n = 4$ is chosen as the baseline.

6.4. Partially shaded module

In most of the sections to follow the same issues are addressed for both breakdown and shunt dominated cases.

6.4.1. Examples of module *I-V*s

In the following examples of *I-V* curves of partially shaded modules, all shaded cells in each particular example are assumed to be equally shaded. Furthermore, if the cell is said to be shaded it means that the whole area of the cell is shaded. Other shading configurations are addressed in the last section.

Figure 6.9 illustrates *J-V* curves of cells in the breakdown dominated case with different values of $\gamma = 0.0, 0.2, .., 1.0$, $V_B = -1.5$ V and $n = 4$.

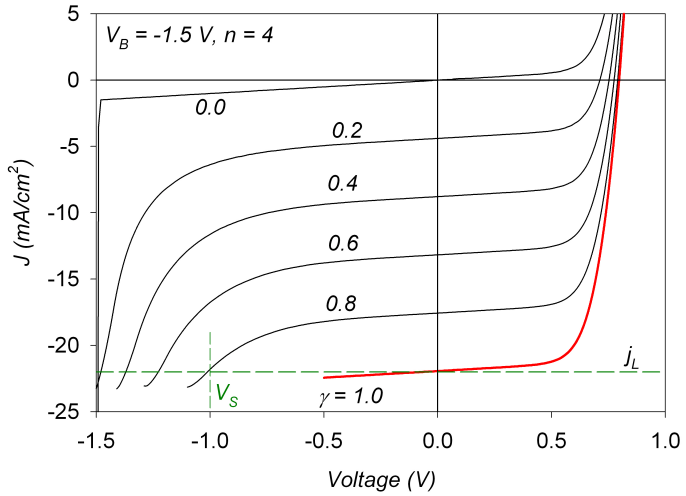

Fig.6.9. Cell *J-V* curves for the breakdown dominated case.

The dashed line in **figure 6.9** represents light generated current level j_L. In accordance with equation (6.8), the dashed line intersects the curves at different values of V_S depending on the illumination coefficient γ.

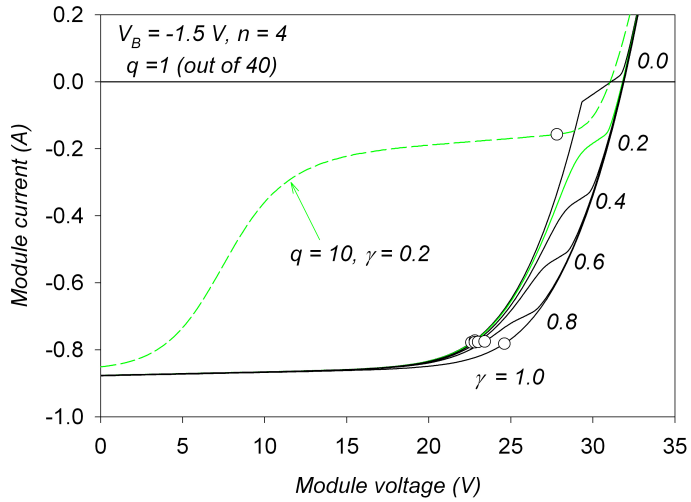

Fig.6.10. Module *I-V* curves for the breakdown dominated case.

Cell *J-V* curves shown in **figure 6.9** are used to calculate module *I-V* curves. **Figure 6.10** shows module *I-V* curves in the breakdown dominated case when one cell out of 40 is

shaded with different values of γ. For comparison, the dashed line in **figure 6.10** represents module *I-V* curve when 10 cells out of 40 are shaded with $\gamma = 0.2$.

Since cells in the module are connected in series the unusual bending of the module *I-V* curve takes place approximately at the current level determined by the illumination coefficient γ. For instance, **figure 6.9** implies that for $\gamma = 0.2$ the light generated current of the shaded cell is $j_L' = j_L \cdot \gamma = -22 \cdot 0.2 = -4.4$ mA/cm^2. Since the area A of the cell used in simulations is 40 cm^2, it follows that $I_{Bending} = j_L' A \approx -0.2$ A.

Figure 6.11 is similar to **figure 6.9** but in the shunt dominated case with $G = 1$ mScm^{-2}. **Figure 6.11** shows that V_S values in the shunt dominated case are much larger than in the breakdown dominated case. These *J-V* curves are used to simulate partially shaded module *I-V* curves shown in **figure 6.12.**

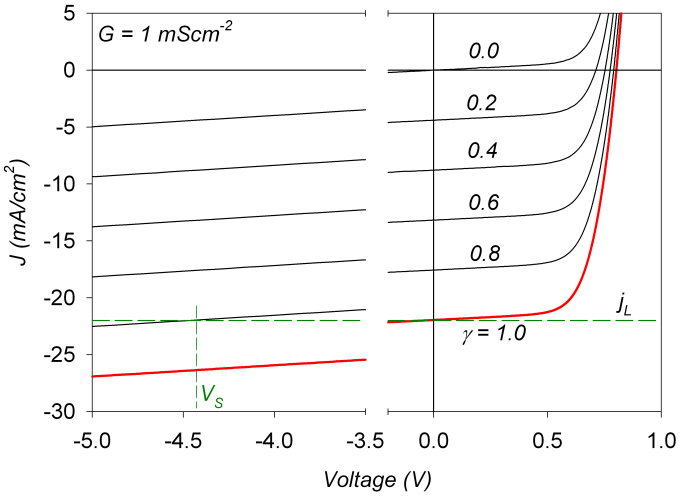

Fig.6.11. Cell *J-V* curves for the shunt dominated case.

Figure 6.12 shows module *I-V* curves in the shunt dominated case when one cell out of 40 is shaded. Again, for comparison, the dashed line in **figure 6.10** represents module *I-V* curve when 10 cells out of 40 are shaded with $\gamma = 0.2$.

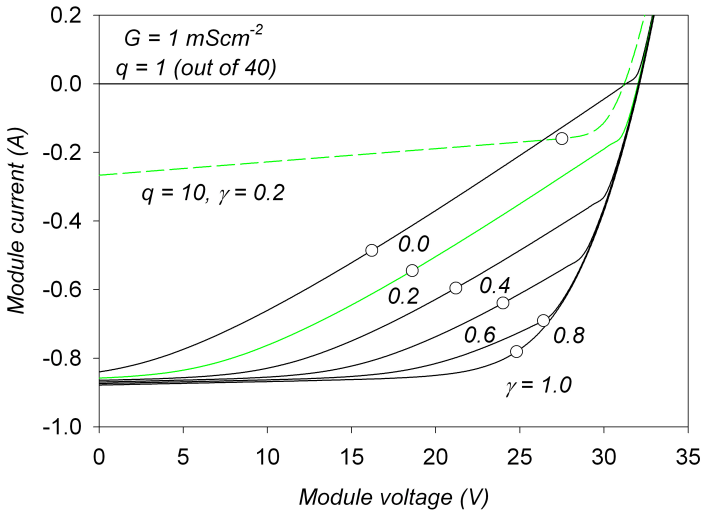

Fig.6.12. Module *I-V* curves for the shunt dominated case.

Module *I-V* curves shown in **figure 6.12** in the vicinity of maximum power points have a quasi-linear behavior. The slope in that region can in principle be calculated analytically. The current level at which module *I-V* curve bends, $I_{Bending}$, is again determined by γ, just as for the breakdown case; the same calculations as given above can be applied here. The dashed line in **figure 6.12** has a much lower I_{SC}. This is because the inequality (6.12) for shunt-dominated case is not satisfied and full I_L cannot pass through the shaded cell; j_L = 22 mA/cm^2 and G = 1 mScm^{-2} yield $j_L/G = 22$ *V*, while V_{OC} = 0.8 V, p = 30 and q = 10 yield $V_{OC}\cdot(p/q)$ = 2.4 V < 22 V.

6.4.2. Shaded-cell voltage

Module safety, lifetime and stability depend on the operating voltage of the shaded cell in the partially shaded module.

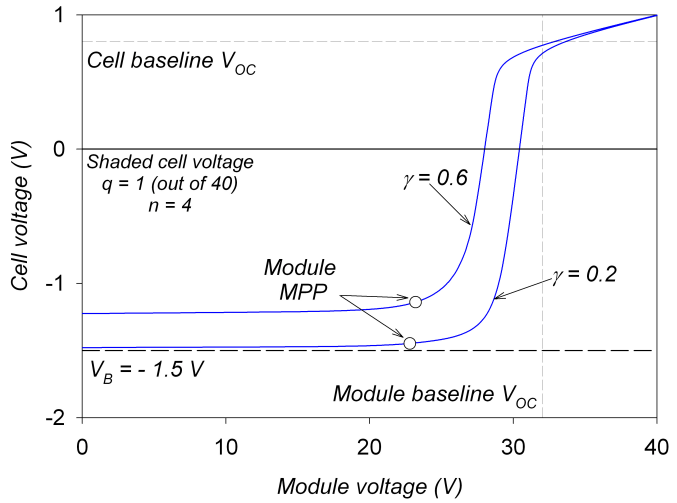

Fig.6.13. Shaded-cell voltage vs. module voltage in the breakdown dominated case.

Figure 6.13 shows shaded cell voltage as a function of module voltage in the breakdown dominated case (V_B = - 1.5 V and n = 4) for two values of γ, 0.2 and 0.6. Only one cell out of 40 is shaded. The baseline module and cell V_{OC} values are shown by dashed lines for reference purposes.

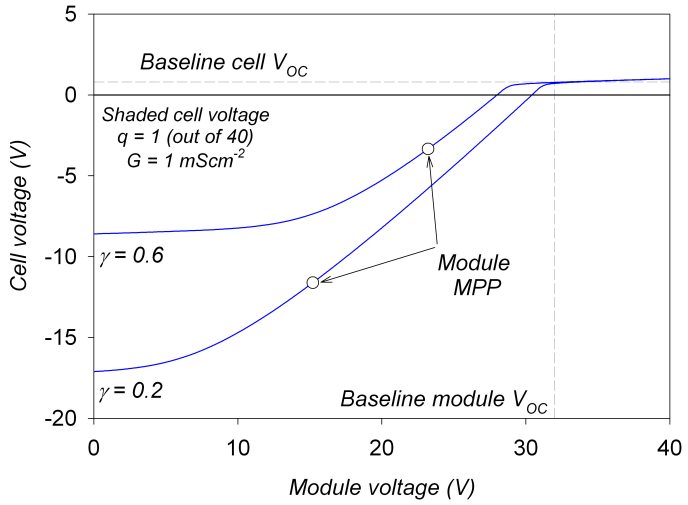

Fig.6.14. Shaded cell voltage vs. module voltage in the breakdown dominated case.

The voltage of the shaded cell at V_{MP} of the module is limited by V_B. Unless V_B is very large, voltage across the shaded cell cannot cause potential problems to the module.

Figure 6.14 is similar to **figure 6.13** but for the shunt dominated case (G = 1mScm^{-2}). In the shunt-dominated case the voltage across the shaded cell can get very high depending on γ. Large reverse voltage across the shaded cell implies that the power dissipated in that cell may be very high. High power dissipation in turn causes increase in the temperature of the cell. The temperature, in principle, can exceed the upper limit of the safe range for the module. Furthermore, if the cell is frequently shaded for a long period of time (thus being frequently exposed to high temperatures and large reverse voltages) it will degrade faster than the rest of the module. Power and temperature aspects are considered in more depth in the following sections.

6.4.3. Power of partially-shaded module in the breakdown dominated case

Figure 6.15 shows module *I-V* curves with different percentage of shaded cells 0, 5,..,25% with γ = 0.2 in the breakdown case (V_B = -1.5 V, n = 4).

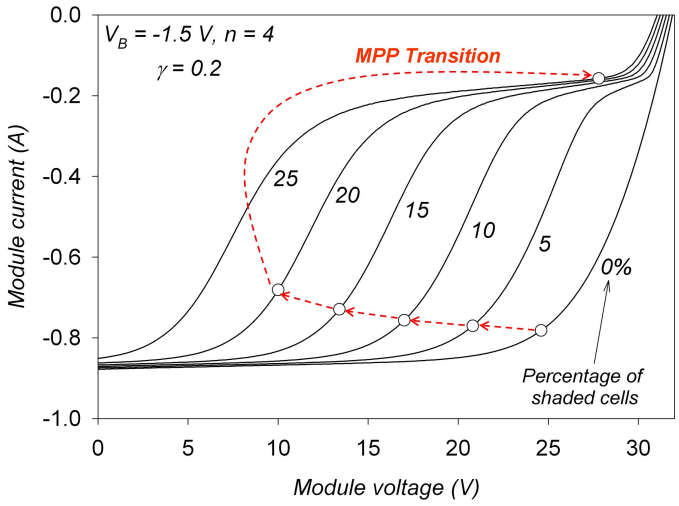

Fig.6.15. Module *I-V* curves with different percentage of shaded cells in the breakdown dominated case.

The dashed arrows show propagation of the maximum power point (MPP). There is an abrupt transition in voltage of the MPP when the percentage of shaded cells shifts from 20 to 25%. If the module is equipped with the MPP tracking electronics the operating voltage of the module will follow dashed arrows depending on the percentage of shaded cells. **Figure 6.16** shows the module power curves corresponding to the *I-V* curves shown in **figure 6.15**. The dashed arrows in **figure 6.16** have the same meaning as in **figure 6.15**. When the percentage of shaded cells in the module is non-zero, the power curve has two maxima. The transition in MPP takes place when the local maximum at higher voltages becomes the global maximum.

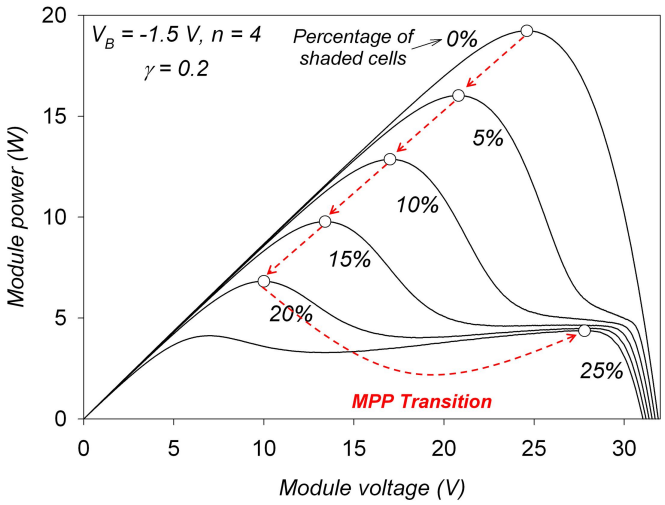

Fig.6.16. Module power curves with different percentage of shaded cells in the breakdown dominated case.

The transition in MPP is basically the onset of a different regime of the partially shaded module operation. This is more clearly illustrated in **figure 6.17**, which shows cell power as a function of percentage of shaded cells in the module.

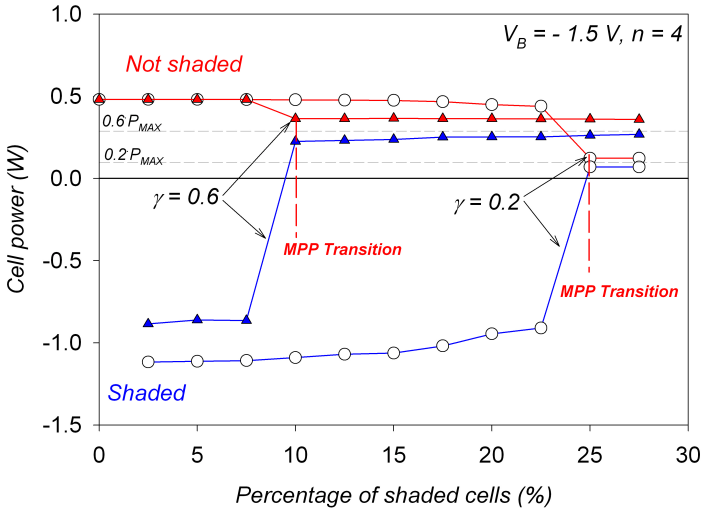

Fig.6.17. Cell power vs. percentage of shaded cells in the breakdown dominated case.

In **figure 6.17** open circles and filled triangles correspond to $\gamma = 0.2$ and 0.6 respectively. The red lines with corresponding symbols show the power generated by fully illuminated cells in the module. The blue lines and their symbols correspond to power consumed or generated by shaded cells. **Figure 6.17** shows that the MPP transition takes place when the shaded cells shift from being consumers to generators and the shaded cells start to dominate the module operation. MPP transition takes place sooner for higher values of γ. Once the MPP transition takes place with an increasing percentage of shaded cells, both the shaded and fully illuminated cells tend to generate $P_{MAX} \cdot \gamma$, where P_{MAX} is the baseline generated cell power at MPP. Dashed lines in **figure 6.17** show $P_{MAX} \cdot \gamma$ levels for $\gamma = 0.2$ and 0.6. In each case, the limit with all cells shaded is γ times the fully illuminated power. **Figure 6.18** shows the total power of the partially shaded module as a function of percentage of shaded cells.

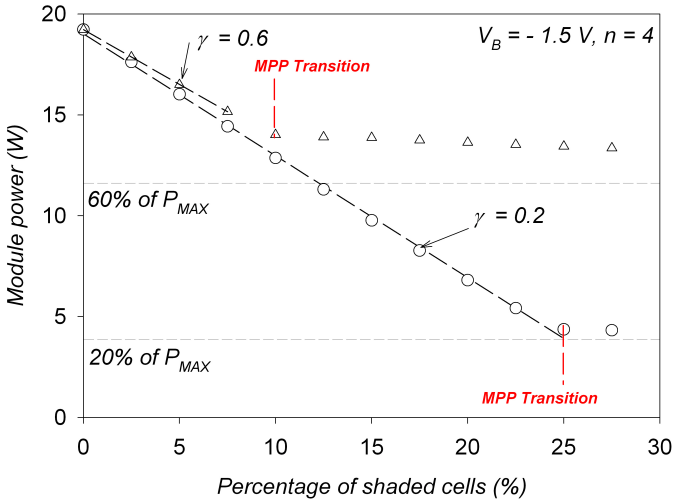

Fig.6.18. Module power vs. percentage of shaded cells in the breakdown dominated case. The symbols in **figure 6.18** have the same meaning as in **figure 6.17**. The total module power decreases quasi-linearly with increasing percentage of shaded cells until the MPP transition. After that it saturates at $P_{MAX} \cdot \gamma$.

6.4.4. Power of partially-shaded module in the shunt-dominated case

This section is similar to the previous one but it describes the shunt dominated case. Therefore, all the symbols and curves in any of the figures shown in this section have the same meaning as the corresponding figures in the previous section.

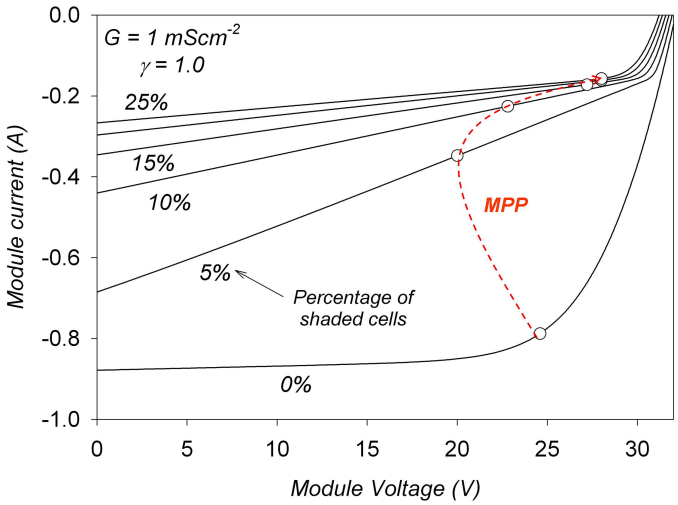

Fig.6.19. Module *I-V* curves with different percentage of shaded cells for the shunt dominated case.

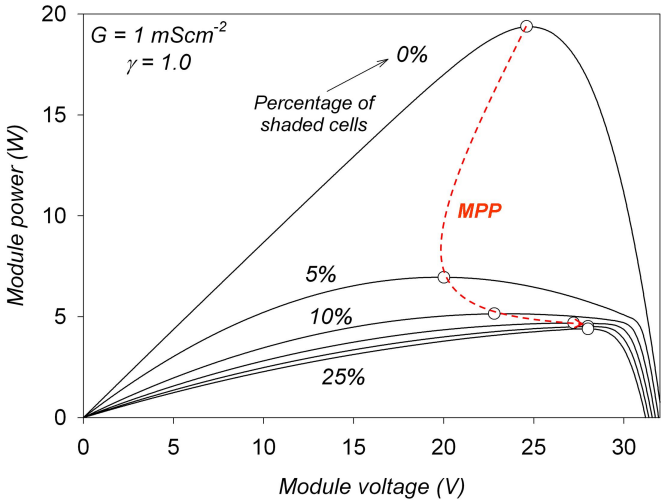

Fig.6.20. Module power curves with different percentage of shaded cells for the shunt dominated case.

Both **figures 6.19** and **6.20** show that there is no abrupt change in module operation; the MPP changes gradually as the percentage of shaded cells increases. Another important difference is that power consumed by shaded cells in the shunt-dominated case is much larger compared to breakdown-dominated case as is shown in **figure 6.21**.

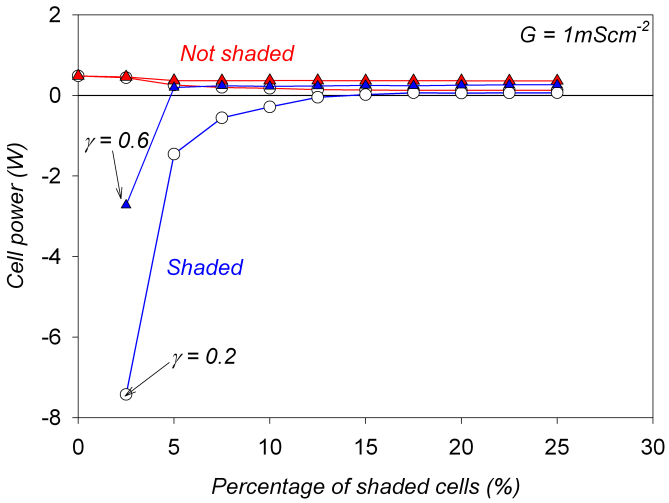

Fig.6.21. Cell power vs. percentage of shaded cells for the breakdown dominated case.

Even though shaded cells do not abruptly shift from being consumers to being generators, they do gradually become generators as the percentage of shaded cells increases. Furthermore, in the shunt dominated case shaded cells become generators sooner than they do in the breakdown case. The last statement, of course, depends on actual values of V_B, n and G, but it holds for reasonable values of these parameters.

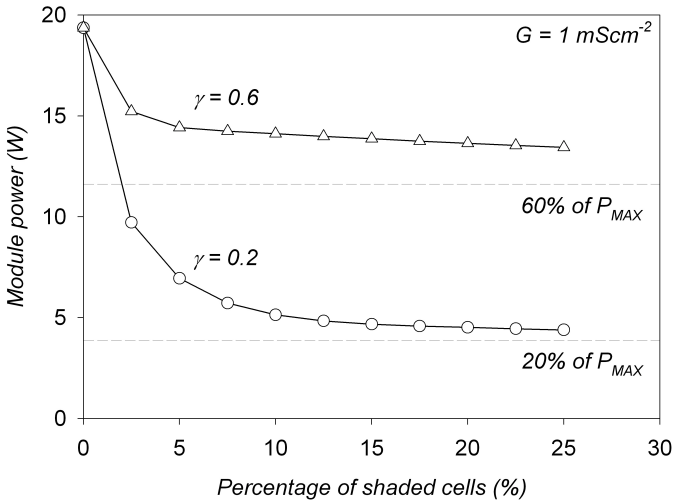

Fig.6.22. Module power vs. percentage of shaded cells for the shunt dominated case.

Figure 6.22 shows that in the shunt dominated case the total power saturates at P_{MAX}·γ, though there is no quasi-linear behavior and abrupt leveling off as is in the breakdown case.

6.4.5. Temperature differential

In the previous section in **figure 6.21** it was shown that in the shunt dominated case the power dissipation in the shaded cell can be very high depending on γ and the number of shaded cells. This implies that the temperature of the shaded cell increases substantially. The temperature of the shaded cell T_{SC} is determined by the power density dissipated in the cell P_D and the coefficient of thermal conductivity κ as follows:

$$\kappa = \frac{P_D\left[W \cdot m^{-2}\right] + 1000\left[W \cdot m^{-2}\right] \cdot \left(1 - \varepsilon_R\right) \cdot \gamma}{T_{SC} - T_A} \left[\frac{W}{m^2\ {}^{o}C}\right], \tag{6.13}$$

where T_A is the ambient temperature and ε_R is the reflection coefficient of the module. The second term in the numerator of equation (6.13) accounts for partial solar illumination of the shaded cell, which can be significant if γ is large enough. In principle, equation (6.13) allows one to calculate the temperature of the shaded cell, T_{SC}, but thermal conductivity κ is generally not a known parameter of the module and is rarely provided by the manufacturer for commercially available PV panels. However, manufacturers of PV modules do provide another parameter, known as NOCT (Nominal Operating Cell Temperature)[33].

NOCT is defined as the equilibrium mean solar cell temperature within an open-rack mounted module in the following standard reference environment (SRE):

- tilt angle: at 45º tilt from the horizontal

- total irradiance: 800 $W \cdot m^{-2}$

- ambient temperature T_A: 20ºC

- wind speed: 1 m/s

- electrical load: nil (open-circuit)

NOCT can be used by the system designer as a guide to the temperature at which a module will operate in the field. It is therefore a useful parameter when comparing the performance of different module designs. For most commercially available modules NOCT is 45 ± 5ºC. Given the definition of NOCT, one can express thermal conductivity of a module as follows:

$$\kappa = \frac{800\left[W \cdot m^{-2}\right]\left(1-\varepsilon_R\right)}{NOCT - 20^{o}C}\left[\frac{\mathrm{W}}{\mathrm{m}^2\ {}^{o}\mathrm{C}}\right]. \tag{6.14}$$

Typical values of $NOCT$ = 45 ºC and ε_R = 0.1 yield $k \approx 30$ W/m^{2}ºC. Thus, with the known value of thermal conductivity of the module, the temperature differential of the shaded cell $\Delta T_{SC} = T_{SC} - T_A$ as a function of P_D from equation (6.13) is:

$$\Delta T_{SC} \approx \frac{1}{30\left[W/m^2\ {}^{o}C\right]}\left(P_D\left[W/m^2\right] + 900\left[W/m^2\right]\cdot\gamma\right) \tag{6.15}$$

Figure 6.23 shows the calculated temperature differential of the shaded cell ΔT_{SC} as a function of module voltage in the shunt dominated case.

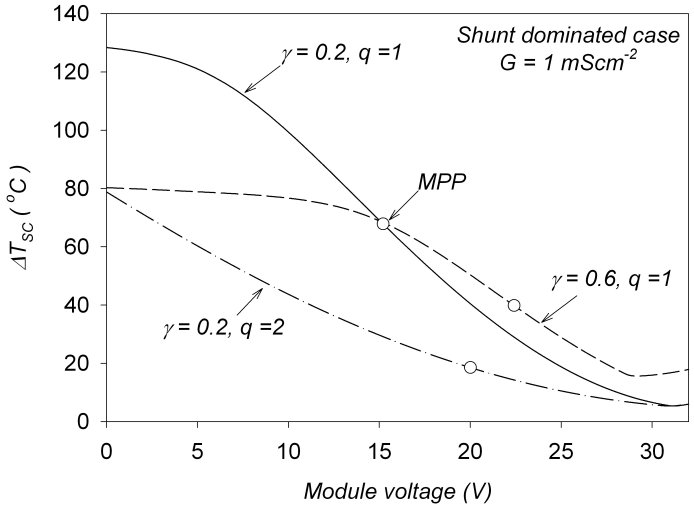

Fig.6.23.Temperature differential of the shaded cell.

Solid, dashed and dash-dot lines correspond to $\gamma = 0.2$ and $\gamma = 0.6$ with one cell shaded and $\gamma = 0.2$ with two cells shaded respectively. Open circles correspond to MPP. The temperature of the shaded cell can increase above the ambient temperature by 20 - 80ºC if the module is equipped with MPP-tracking electronics. The shaded-cell temperature depends on γ and the number of shaded cells, but in many cases can be greater than the temperature of the fully illuminated cells. If there is no MPP-tracking electronics then the increase can be even higher. Furthermore, if the ambient temperature in the summer on a very hot day is ~ +35ºC then the absolute temperature of the shaded cell can be in the range of 100 - 120 ºC, which may cause diffusion of layers, cell cracking, and other serious problems.

The temperature problem becomes more dramatic for solar panels that have larger values of light generated current. As an example, let's compare a CIGS module (j_L ~ 35 mA/cm^2) with CdTe one (22mA/cm^2). Even though the V_{OC} of the CIGS (~ 0.64 V) is lower than that of CdTe (~ 0.8 V) if the number of cells in a CIGS module is large

enough (> 60) inequality (6.12) will be satisfied. This means that equation (6.10) can be applied and V_S(CIGS)/V_S(CdTe) ~ j_L(CIGS)/j_L(CdTe) ~ 35/22 ≈ 1.6, which in turn implies that P_D(CIGS)/P_D(CdTe) ~ 1.6^2 ≈ 2.6 since P_D ~$V_S \cdot j_L$~ j_L^2. Thus, while for a CdTe module in the shunt dominated case, the temperature differential ΔT_{SC} of the shaded cell can reach 100ºC for CIGS it can be as high as 260ºC. On a hot summer day (+35 ºC) the actual temperature of the shaded CIGS cell can be over 300ºC.

6.4.6. Other shading configurations

Figure 6.24 shows different shading configurations with simple geometry. In the discussions above only configuration A was considered, but it is straightforward to deduce configurations B and C from A.

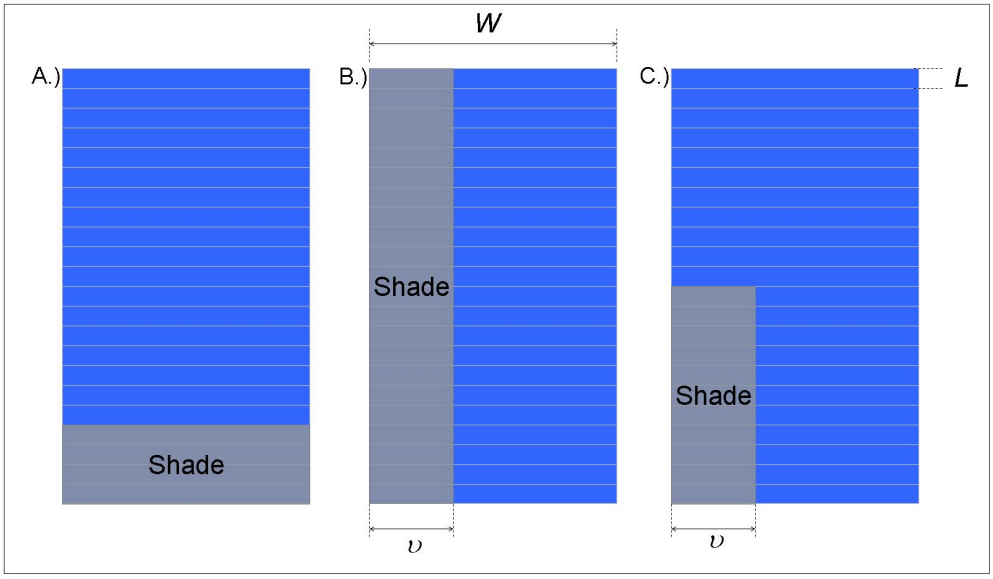

Fig.6.24. Different shading configurations.

Given the same shaded area, configuration B is clearly preferable to configuration A, because in B there is no mismatch between cells even though the module is partially

shaded. The module *I-V* curve in B will be the same as in the baseline case except for a shift in the current. The light generated current $I_L^{(B)}$ in the shaded configuration B is given by:

$$I_L^{(B)} = j_L(W-\upsilon)L + j_L\gamma\upsilon L = I_L\left[1+(\gamma-1)\frac{\upsilon}{W}\right] = I_L\gamma_{eff}, \qquad (6.16)$$

where υ, L and W are shown in **figure 6.24**, I_L and j_L are baseline light generated current and current density respectively.

Configuration C is a particular case of B, however, where there is a mismatch between cells. All results presented above for configuration A are applicable to C, where an effective γ is:

$$\gamma_{eff} = 1+(\gamma-1)\frac{\upsilon}{W}. \qquad (6.17)$$

Usage of γ_{eff} is valid because within the frames of the model adjacent subcells in a cell are independent.

Thus, using developed in this chapter mathematical formalism and the simulation model it has been shown that shading can cause serious problems to module operation and even its safety. It has also been shown here that numerical simulations and analytic calculations can be helpful in the analysis of effects caused by shading. It was found that reverse voltage characteristics of thin-film solar cell determine the operation of the module under partial shading conditions. Shaded cells can be either generators or

consumers of power, depending on different circumstances. Two distinct shaded module operation regimes were outlined. It was also calculated that in some extreme cases temperature of shaded cells can be dangerously high. Shades of different configurations can be treated by introducing an effective shading coefficient.

Chapter 7
Summary and conclusions

A 2-D circuit model was used to estimate losses associated with distributed nature of sheet resistance in the uniform cell. The primary goal of the 2-D circuit model was to analyze the effect of different types of spatial non-uniformities. The three step design of the model (subcell-cell-module) allows one to analyze the impact of non-uniformity with varying parameters (severity, area, distribution, etc.) on a lab-size cell, module-size cell, and the whole module.

Besides the fundamental advantages of 2-D models over 1-D models there are practical and technical advantages. Even though in the present work only three types of non-uniformities were addressed (shunts, weak-diodes and shading) the model has the capability of addressing any spatial non-uniformity without changing the framework of the model and without introducing additional circuit elements. This is possible because instead of using circuit elements, such as diodes and current sources, numerical *J-V* tables of microcells called GTABLEs were used here. For example, a standard 2-D circuit model that implies a network of diodes, current sources and resistors to simulate a back-contact barrier spatial non-uniformity, one would need additional diodes opposite to main ones at spatial locations of non-uniformities. However, in the approach presented here, one would only have to change the numerical table of the non-uniform microcell and

keep the structure of the model unchanged. This may seem to be a purely technical advantage, but it adds universality to the analysis and allows a researcher using the 2-D model much more efficiently.

The TCO sheet resistance is a primary numerical parameter of any 2-D circuit model of a solar cell. It is important to have an analytic relation between the sheet resistance, which is a physical parameter, and model TCO resistance R. Such an analytic relation between ρ_S, R and discretization level N has been derived in the present work based on calculation of power dissipation in the TCO layer. Having such analytic relation allows comparison of results from different researchers who use relations between ρ_S and R based on other principles.

Even though a single-parameter series resistance R_S is applicable only to non-distributed TCO sheet resistance models, it is important to have a relation between an effective R_S and ρ_S for practical purposes. Such an analytic relation has been derived in the present work. For a given typical thin-film geometry series resistance R_S can be expressed in terms of sheet resistance ρ_S, length of the cell L, absorber layer resistivity ρ and its thickness b. It was also shown that for typical thin-film parameters the absorber layer resistivity has negligible effect on R_S. Such a relation can be used by manufacturer to estimate the sheet resistance of the TCO from the J-V curve of the uniform cell or module.

Based on the analysis of the uniform subcell it has been empirically shown that there is a global parameter δ that can be used to estimate the FF loss of a subcell or cell due to sheet resistance. It was shown that δ depends on four parameters ρ_S, V_{OC}, J_{SC}, and

L. Such a global parameter can be used by a manufacturer to predict how FF will change with these four parameters.

It was shown that in the uniform case there are two power losses associated with distributed TCO sheet resistance: dissipation in the TCO layer due to lateral currents P_{TCO} and power loss due to variation in microdiode operating voltage P_{MD}, which is generally less than P_{TCO}. It was also shown that at MPP to a good approximation $P_{TCO} \sim \rho_S \cdot J_{SC}^2$. In the uniform case the P_{MD} increases with ρ_S and at sufficiently large values of ρ_S becomes comparable with P_{TCO}. Typical thin-film solar cell parameters (ρ_S, J_{SC}, L etc.) in the uniform case yield total power loss associated with distributed TCO sheet resistance ($P_{TCO} + P_{MD}$) around 10-20%. Just as in the uniform case power loss was used to evaluate the impact of micro-shunts and weak microdiodes on a subcell.

It was found that the location of the shunt in the subcell makes a relatively minor difference. The further away the shunt is from the gridline the better. In the shunted subcell case the dominant power loss is the power dissipated in the shunt itself P_{SH}. Even though P_{SH} was found to be in the range of ~ 1-10 mW the dissipated power density can be on the order of ~ 1 W/cm^2 depending on the physical shunt area. Such high power density may cause elevated temperature (hot-spot) and in turn can significantly alter material properties in the vicinity of the shunt. In the shunted subcell case P_{TCO} increases with ρ_S just as in the uniform case, but P_{MD} stays relatively constant. It was also found that P_{SH} decreases semi-linearly with ρ_S (TCO sheet resistance screening effect), but at a relatively modest rate. The overall loss and P_{SH} in particular are smaller for larger J_{SC}. This was found to be qualitatively consistent with analytic relation between shunt screening length L_{SC} and J_{SC}: $L_{SC} \sim J_{SC}^{-1/2}$. Therefore, CIGS cells are more tolerant to

shunts than CdTe cells because the L_{SC} of CdTe is larger than that of CIGS. For a manufacturer this implies that shunts are more of an issue to CdTe solar cells than to CIGS.

It was shown that the subcell is more sensitive to the location of the weak-microdiode then it is for shunts and the trend is opposite and more complex. If the weak-microdiode is very weak it serves as a power consumer rather than power generator. The primary difference of weak-microdiode from micro-shunt is that for weak-microdiode P_{MD} is the dominant power loss. Power lost in the weak-microdiode itself P_{WD} is comparable to P_{TCO}. Also it was shown that P_{WD} exponentially depends on the weak-microdiode severity. The major loss P_{MD} decreases with increasing sheet resistance ρ_S.

Thus, a single micro-shunt or weak-microdiode can have a severe destructive effect on a small size cell (subcell). However, even a single extremely severe shunt or weak-diode cannot have a serious effect on the whole module. Therefore, a collective impact of multiple non-uniformities on a module, which is typical for thin-film modules, was studied. For simplicity of analysis, the effect of multiple but identical non-uniformities was studied. To address that issue in a more systematic fashion an easy-to-work practical numerical parameter P was introduced to characterize non-uniformity distribution pattern of identical non-uniformities over the module. It was found that absolute module efficiency loss $\Delta\eta$ (%) is a strong function of not only the fractional shunted area A_S and shunted area efficiency η_S but also of the shunt distribution pattern. The same was found to be true for weak-diodes.

It was found that for given values of A_S and η_S independent of the module size the $\Delta\eta$ has a maximum (the worst case scenario) when shunts are distributed uniformly over

the module area. In the worst case scenario and in the intermediate case scenario, when shunts are evenly distributed over all cells in the module, the $\Delta\eta$ is mostly due to *FF* reduction while decrease in V_{OC} is insignificant. It was also shown that concentration of shunts in a few cells is the most preferable scenario, and in that case reduction in both *FF* and V_{OC} is comparable. Thus, in some cases comparing *FF* and V_{OC} reductions from the module *J-V* curve one can identify which shunt distribution pattern is taking place. The decrease in J_{SC} and second order terms in all scenarios is insignificant. It was found that $\Delta\eta$ depends more strongly on η_S compared to A_S, which generally means that one would rather have many mild shunts than a few strong ones. Depending on A_S and η_S absolute module efficiency $\Delta\eta$ (%) varies around ~ 1-4%. Simple area-weighted efficiency calculations underestimate $\Delta\eta$ by 3-5 times.

Same distribution patterns of weak-diodes affect the module performance in a different way compared to shunts. For the given fractional weak area A_W and weak area open-circuit voltage $V_{OC\text{-}W}$ the worst case is when weak diodes are evenly distributed over all cells in the module and the most preferable case is when they are clustered in just a few cells. Situation when weak-diodes are uniformly spread over the whole module area happens to be intermediate. In the worst case scenario reduction in $\Delta\eta$ is due to decrease in *FF* and V_{OC} to comparable extents, while in the best case scenario mostly due to decrease in V_{OC}. Decrease in J_{SC} and second order terms have little effect on $\Delta\eta$ reduction just as it is for shunts. An important practical observation is that for all situations, decrease in V_{OC} is generally larger for weak diodes compared to shunts. This to some extent may be used to identify the nature of non-uniformities from the module *J-V* curve.

Just as for shunts simple area-weighted efficiency estimates yield a significant error in $\Delta\eta$ and the range of $\Delta\eta$ is essentially the same as for shunts.

There are several spatially resolved experimental techniques such as LBIC, thermograph, photoluminescence, electroluminescence (EL) etc. that can screen for non-uniformities like shunts and weak-diodes in modules. However, experimental data obtained from these techniques is of little value unless there is a model based on which one can extract useful information from the gathered data. In the current work it was shown that the developed 2-D circuit model can be successfully used to analyze data obtained from EL measurements, which are gaining popularity in PV as a promising screening tool.

It was shown how the microdiode voltage distribution map in a cell can be translated into EL intensity $\phi(x,y)$ map through the reciprocity relation. Two different parameters were introduced to extract useful information from EL data. Both parameters reflect same EL intensity but normalized in two different ways: 1.) $\phi(x,y)/\phi_0(0,y)$ called C-contrast, and 2.) $\phi(x,y)/\phi_0(x,y)$ called CC-contrast, where subscript 0 refers to the uniform cell. The dependence of the EL intensity on current was analyzed. It was found that the following dependence may be valid: $\phi \sim J^A$, where A is the diode quality factor.

For the uniform cell an analytic dependence of the C-contrast on position x, sheet resistance ρ_S, current J, and cell length L was derived. That analytic expression can be used to predict how EL image (C-contrast) would change with current and estimate ρ_S from EL data of the uniform cell. Results obtained from simulations were consistent with experimental findings in Uwe Rau's paper.

A general set of recommendations based on the analysis of the EL data (C- and CC-contrast) that can help distinguish a shunt from a weak-diode and put non-uniformities in the module in order of their severity was proposed. Some recommendations related to experimental calibration that can enhance the proposed analysis were developed. The benefits of integrating an in-situ EL measuring system into thin-film module production line were outlined.

Shunts and weak-diodes are microscopic defects, but there can also be macroscopic non-uniformities, the most common of which, is the non-uniformity in illumination level caused by temporal or permanent shades when the module operates out in the field. To address the issue of partial shading of thin-film modules theoretical and empirical results obtained for crystalline solar cells were adopted to develop a mathematical formalism of reverse voltage characteristics of thin-film solar cells. The core of the formalism is the analytic expression of the microcell *J*-*V* curve in the reverse bias. In the developed mathematical formalism two distinct extremes were identified: shunt- and breakdown-dominated cases. A real thin-film module would fall somewhere in-between these two extremes.

A graphic explanation of why under certain circumstances shaded cells in the partially shaded module are reverse-biased was presented. Approximate analytic expressions of the voltage across the shaded cell V_S in the partially shaded module and their range of validity were derived for both shunt- and breakdown-dominated cases. These simple expressions allow a manufacturer to a priori estimate what reverse voltage across shaded cells would be under common shading conditions. For the baseline it was estimated that for shunt-dominated case the V_S can be quite high (~ 20 V), while in the

breakdown-dominated case V_S is essentially limited by V_B, which for thin-film solar cells happens to be rather small: ~ 1-5 V. For better understanding of module operation under partial shading conditions examples of calculated *I-V* curves of partially shaded modules for both shunt- and breakdown-dominated cases were presented and their primary features were addressed in a systematic quantitative fashion.

A detailed analysis of power conditioning of shaded cells in the partially shaded module was performed. It was found that in both shunt- and breakdown-dominated cases, depending on the percentage of shaded cells and illumination coefficient γ, a partially shaded module operates in one of two different regimes. For a given γ, the first regime takes place when percentage of shaded cells is small and the operation of the whole module is dominated by fully illuminated cells. In the first regime shaded cells serve as power consumers. When the percentage of shaded cells increases a transition of the module operation to the second regime takes place. In the second regime the module operation is dominated by shaded cells and they shift from being power consumers to power generators. In the second regime with increase in percentage of shaded cells both shaded and illuminated cells tend to generate $P_{MAX} \cdot \gamma$, where P_{MAX} is the baseline generated cell power at MPP. When all cells are shaded they all generate exactly $P_{MAX} \cdot \gamma$. For larger values of γ the transition happens at smaller percentage of shaded cells. The only qualitative difference between shunt- and breakdown dominated cases is that in latter the transition is abrupt and in the former it is gradual. Because of typically larger values of V_S in the shunt dominated case in some extreme situations (only 1-2 cells extremely shaded) the power dissipated in the shaded cell can be quite high (up to ~ 40%

of the baseline generated module power). This implies that the temperature of shaded cells T_{SC} can increase substantially causing some serious problems.

The issue of T_{SC} was addressed in a systematic fashion with the help of internationally adopted solar panel parameter: NOCT (Nominal Operating Cell Temperature). It was shown that for a typical CdTe module ΔT_{SC} (above ambient) under some extreme shading conditions can be as high as 100ºC. It was also shown that $\Delta T_{SC} \sim J_L^2$ and, for example, for CIGS the temperature differential $\Delta T_{SC} \sim 260$ºC. Such an analysis that allows one to estimate the upper temperature limit is helpful both for consumers and manufacturers for module and general safety issues.

An effective illumination coefficient γ_{eff} was introduced to address other shading configurations. All results obtained for standard shading configuration (when shade covers the entire area of the shaded cell) can be extended to other shading configurations if γ_{eff} is properly used.

Thus, current work discusses the issue of non-uniformities (shunts, weak-diodes and shading) in a systematic fashion. A set of useful recommendations and results related to these non-uniformities were extracted from 2-D numerical simulations based on the developed here circuit model. General strategies of addressing the impact of non-uniformities on both small size solar cells and large area modules were outlined.

REFERENCES

[1] AVS Rocky Mountain Chapter, Short Course: “Introduction to PV Technology” by J.Alleman and S.Robbins (NREL).

[2] U.Rau, T.Kirchartz, A. Helbig and B.E. Pieters, “Electroluminescence imaging of CIGS thin film solar modules,” MRS symposium proceedings, V.1165 (2009), pp. 87-92.

[3] Steven S. Hegedus and William N. Shafarman, “Thin-Film Solar Cells: Device Measurements and Analysis,” Prog. Photovolt: Res. Appl. 2004; **12**: 155-176.

[4] OrCAD PSpice®, Electronic Design Software, EMA Design Automation, 225 Tech Park Drive, Rochester, NY 14623.

[5] M.A. Green, Solar Cells: Operating Principles, Technology, and System Applications, Prentice Hall, Englewood Cliffs, NJ, 1982, p.145.

[6] AFORS-HET (Automat FOR Simulation of HETerostructures) is a numerical simulation tool, which allows one to model/simulate heterojunction semiconductor devices. Developed at Hahn-Meitner Institute (HMI), Berlin.

[7] M. Gloeckler, A.L. Fahrenbruch, and J.R. Sites, “Numerical modeling of CIGS and CdTe solar cells: setting the baseline,” Proc. 3rd World Conference on Photovoltaic Energy Conversion, 2003, pp.491-494.

[8] T.J. McMahon, T.J. Berniard, and D.S. Albin, “Nonlinear shunt paths in thin-film CdTe solar cells,” Journal of Applied Physics **97**, 054503 (2005).

[9] A.L. Fahrenbruch, R.H. Bube, Fundamentals of Solar Cells, Photovoltaic Solar Energy Conversion, Academic Press, New York, 1983, p. 362-364.

[10] Lars Drud Nielsen, “Distributed series resistance effects in solar cells,” IEEE Transactions on electron devices, VOL. ED-29, NO. 5, May 1982.[11] V.G. Karpov, G.Rich, A.V. Subashiev, and G. Dorer, “Shunt screening, size effects and I/V analysis in thin-film photovoltaics,” Journal of Applied Physics, VOL. 89, NO. 9, May 2001.

[12] T. Kirchartz, J. Mattheis, and U. Rau, “Electroluminescence from CIGS Thin-Film Solar Cells,” MRS symposium proceedings, V.1012 (2007), pp. 115-120.

[13] T. Kirchartz, U.Rau, M.Kurth, J.Mattheis, J.H. Werner, "Comparative study of electroluminescence from CIGS and Si solar cells," Thin Solid Films **515** (2007), 6238-6242.

[14] U. Rau, "Reciprocity relation between photovoltaic quantum efficiency and electroluminescent emission of solar cells," Phys. Rev. B **76**, 085303 (2007).

[15] K.J. Price, A.Vasko, L.Gorrell and A.D.Compaan, "Temperature-Dependent Electroluminescence," MRS symposium proceedings, V.763 (2003), pp. 195-200.

[16] G.R. Walker, P.C. Serina, "Cascade DC-DC converter connection of photovoltaic module," Power Electronics Specialists Conference, 2002. psec 02.2002 IEEE 33rd Annual, Vol. 1 p.24-29.

[17] Antonio Luque, Steven Hegedus, "Handbook of Photovoltaic Science and Engineering," Wiley pp. 863-902.

[18] H. Field, A. M. Gabor, "Cell binning method analysis to minimize mismatch losses and performance variation in Si-based modules," PVSC 29th IEEE.

[19] K. Wilson, D. Ceuster, R. Sinton, "Measuring the effect of cell mismatch on module output", World Conference on Photovoltaic Energy Conversion, Hawaii

[20] R. Gonzales, R. Weaver, "Circuit design considerations for photovoltaic modules and systems," Proc. Of the 14th IEEE PVSC, San-Diego, 1980, p 528-535

[21] A. Brandstetter, A. Hinds, E.K. Inall, "Eighteenth IEEE Photovoltaic Specialists Conference - 1985," 21-25 Oct. 1985, Las Vegas, NV, USA; p.1025-30

[22] E. S. Hasyim, S.R. Wenham, M.A. Green, "Shadow tolerance of modules incorporating integral bypass diode solar cells," Solar cells, Vol. 19, 1986, pp. 109-122

[23] C. Zener, "A Theory of the Electrical Breakdown of Solid Dielectrics," Proceedings of the Royal Society of London, Series A , 1934, Vol. 145, pp. 523-529.

[24] K.G. McKay "Avalanche Breakdown in Silicon," Phys. Rev. **94**, 877 (1954).

[25] K.G. McKay, K.B. McAfee, "Electron multiplication in Silicon and Germanium," Phys. Rev. **91**, 1079 (1953).

[26] S.L. Miller, "Avalanche breakdown in Germanium," Phys. Rev. **99**, 1234 (1955).

[27] S.L. Miller, "Ionization rates for holes and electrons is Silicon," Phys. Rev. **105**, 1246 (1957).

[28] W.Shockley, "Transistor Electronics: Imperfections, unipolar and analog transistors," Proceedings of the I.R.E., 1952, pp. 1289-1313.

[29] R.F. Pierret, Semiconductor Device Fundamentals, 1996, pp. 268-270.

[30] P. Spirito and V. Albergamo, “Reverse bias power dissipation of shadowed or faulty cells in different array configurations,” in Proceedings of the 4th European Photovoltaic Solar Energy Conference, 1982, pp. 296-300.

[31] M.C. Alonso-Garcia, J.M. Ruiz, “Analysis and modeling the reverse characteristic of photovoltaic cells,” Solar Energy Materials & Solar Cells 90 (2006) 1105-1120.

[32] S. Silvestre, A Chouder, “Effects of shadowing on photovoltaic module performance,” Prog. Photovolt: Res. Appl. 2008; **16**:141-149.

[33] IEC 61646 INTERNATIONAL STANDRD, Thin-film terrestrial photovoltaic (PV) modules – Design qualification and type approval.